RECONSTRUCTION IN TOMOGRAPHY WITH DIFFRACTING SOURCES

A Dissertation

by

YUAN XU

Submitted to the Office of Graduate Studies of
Texas A&M University
in partial fulfillment of the requirements for the degree of

DOCTOR OF PHILOSOPHY

December 2003

Major Subject: Biomedical Engineering

RECONSTRUCTION IN TOMOGRAPHY WITH DIFFRACTING SOURCES

A Dissertation

by

YUAN XU

Submitted to Texas A&M University
in partial fulfillment of the requirements
for the degree of

DOCTOR OF PHILOSOPHY

Approved as to style and content by:

Lihong V. Wang
(Chair of Committee)

Edward S. Fry
(Member)

Hsin-i Wu
(Member)

Jay D. Humphrey
(Member)

William A. Hyman
(Head of Department)

December 2003

Major Subject: Biomedical Engineering

ABSTRACT

Reconstruction in Tomography
with Diffracting Sources. (December 2003)
Yuan Xu, B.S., Wuhan University;
M.S.,Shanghai Institute of Optics and Fine Mechanics;
Ph.D., Institute of Physics, Chinese Academy of Sciences
Chair of Advisory Committee: Dr. Lihong V. Wang

In this dissertation, we first derive exact reconstution algorithms for thermoacoustic tomography (TAT) and broadband diffraction tomography (a linearized inverse scattering problem) using derived time-reversal formulas. Then we focus on some important practical problems of TAT including the limited-view problem, the effects of acoustic heterogeneity, and fast reconstruction algorithms.

In Chapter II, we propose time-reversal methods and apply them to tomography with diffrating sources. We first develop time-domain methods to time-reverse a transient scalar wave using only the field measured on an arbitrary closed surface enclosing the initial sources. Under certain conditions, a time-reversed field can be obtained with the delay-and-sum algorithm (backprojection to spheres) used in synthetic aperture imaging. Consequently, the physical meaning and the valid conditions of this widely used algorithm are revealed quantitatively for the first time from basic physics. Then exact reconstruction for TAT and broadband diffraction tomography is proposed by time-reversing the measured field back to the time when each source or secondary source is excited. The theoretical conclusions are supported by a numerical simulation of three-dimensional diffraction tomography. The extension of our time-reversal methods to the case using Green function in a heterogeneous medium is also discussed.

In Chapter III, the limited-view problem is studied for TAT. We define a "detection region," within which all points have sufficient detection views. It is explained analytically and shown numerically that the boundaries of any object inside this region can be recovered stably. Otherwise some sharp details become blurred. One can identify in advance the parts of the boundaries that will be affected if the detection view is insufficient. Computations are conducted for both numerically simulated and experimental data. The reconstructions confirm our theoretical predictions.

In Chapter IV, the effects of wavefront distortions induced by acoustic heterogeneities in breast TAT are studied. Amplitude distortions are shown to be insignificant for different scales of acoustic heterogeneities. After that we consider the effects of phase distortions (errors in time-of-flight) in our numerical studies. The numerical results on the spreads of point sources and boundaries caused by the phase distortions are in good agreement with the proposed formula. We also demonstrate that the blurring of images can be compensated for by using the distribution of acoustic velocity in the tissues in the reconstructions.

In Chapter V, we discuss exact and fast Fourier-domain reconstruction algorithms for TAT in planar and circular configurations.

To my wife Xiaotong and my daughter Grace

ACKNOWLEDGMENTS

I would like to thank Dr. Lihong Wang, my supervisor, for his guidance and constant support during this research. I would also thank the current and some former members of optical imaging lab. The creative and supportive research environment in the lab made my research possible.

I would like to thank Dr. Peter Kuchment and Dr. Qin Zhu for many useful discussions, and Dr. Hsin-i Wu and Dr. Jay Humphrey for their advice on my research. I am also indebted to the anonymous reviewers of my journal papers, whose constructive comments led to a more comprehensive investigation in my research.

Finally, I wish to thank my parents for their patience and love, and the following: Kim Jung, Xiaofan Zhang, Kaibin Fu, and many others for all the good times we had together.

TABLE OF CONTENTS

LIST OF FIGURES

CHAPTER I

INTRODUCTION

A. TOMOGRAPHY WITH DIFFRACTING SOURCES

Traditional X-ray and emission tomographies have been successful, but they are either ionizing or radiative. Interest in tomography with diffracting sources has been increasing due to the need for developing novel noninvasive non-ionizing medical imaging modality. In X-ray and emission tomographies, a ray travels from the source to the detector along a straight line, because the diffraction effect is ignorable due to the much smaller wavelength than the resolution of the imaging system. In this case, the signal at one detection position is just the integration of the object value along a straight line. On the other hand, in the tomography with diffracting sources, the diffraction effect can not be ignored because the wavelength of the field is on the same scale of the resolution of the system. Consequently, the signal at one detection position is related with the object value throughout the object space. This makes the tomography with diffracting sources (TWDS) more challenging. Diffraction-based tomographies have wide applications in industry field and medical imaging. Some examples are diffraction tomography (DT) and thermoacoustic tomography (TAT), which may also be referred to as photoacoustic or optoacoustic tomography depending on the source of irradiation. In DT, objects are irradiated by an illuminating (acoustic or electromagnetic) source and the scattered field is measured to map the heterogeneity of objects. In TAT, objects are irradiated by electromagnetic pulse, and the thermoacoustic signal, which is induced by the electromagnetic absorption and the subsequent thermoelastic expansion, is measured to map the electromagnetic

---

The journal model is *IEEE Transactions on Automatic Control.*

absorption of objects.

B. THERMOACOUSTIC TOMOGRAPHY

When electromagnetic radiation is absorbed in biological tissues, the heating and the subsequent expansion will cause emission of acoustic signals, which is called the thermoacoustic effect. In thermoacoustic tomography, the thermoacoustic signals from a tissue sample are collected to map the distribution of the radiative absorption within the sample. The radiative absorption is closely related to the physiological and pathological status of the tissue: for example, cancerous breast tissues are 2-5 times more strongly absorbing to microwaves than surrounding normal breast tissues [1, 2, 3], which has been attributed to an increase in bound water and sodium within malignant cells. While the optical absorption is related to the oxy- and deoxyhemoglobin [4].

Thermoacoustic tomography combines good imaging resolution with good imaging contrast. Purely microwave or optical imaging has the advantage of good imaging contrast but suffers from poor spatial resolution [5, 6, 7, 8]. On the other hand, purely ultrasonic imaging has good spatial resolution but poor contrast. Thermoacoustic tomography can bridge the gap between them. Therefore, in this thesis, TAT will be studied in more details.

There are various types of thermoacoustic tomography, such as photoacoustic tomography [9, 10, 11] and microwave-induced thermoacoustic tomography (MITT) [12, 13, 14, 15, 16, 17, 18, 19]. In photoacoustic tomography, due to the use of short laser pulses (several nanoseconds in pulse width) and the strong attenuation of the laser light by tissues, the frequency spectrum of the acoustic signal from the buried object of several micrometers in size is estimated to have significant components up to

75 MHz, which makes its axial resolution as good as 10 μm. However, the maximum imaging depth in photoacoustic tomography is limited by the strong attenuation of the laser light and of the high-frequency acoustic waves. On the other hand, MITT can be used to image much deeper tissues due to the relatively low absorption of microwaves. The spectra of the acoustic signals in MITT are usually below 2 MHz, and the axial resolution is not better than 1 mm. Several investigators employed microwave-induced thermoacoustic waves in the 1980s for imaging of biological tissues; these early works however did not produce any tomographic or depth-resolved images. Recent progress realized tomographic imaging of biological tissues based on microwave-induced thermoacoustic waves [16].

C. FORWARD FORMULAS OF TAT IN A HOMOGENEOUS MODEL

We will be deriving a formula for the forward problem in an acoustically homogeneous model, which will be used in the following chapters on TAT. In the case of thermal confinement, the acoustic wave at point $\mathbf{r}$ and time t, $p(\mathbf{r}, t)$, is related to the microwave absorption $H(\mathbf{r}, t)$ by the following wave equation [20]:

$$\frac{\partial^2 p(\mathbf{r}, t)}{\partial t^2} - \nu_{s0}^2 \nabla^2 p(\mathbf{r}, t) = \frac{\beta}{C} \frac{\partial H(\mathbf{r}, t)}{\partial t}, \tag{1.1}$$

where v_{s0} is the acoustic speed; C is the specific heat; and β is the coefficient of the volume thermal expansion. (1.1) can be rewritten in terms of $H(\mathbf{r}, t)$:

$$p(\mathbf{r}, t) = \frac{\beta}{4\pi C} \iiint \frac{\partial H(\mathbf{r}', t')}{\partial t'} \frac{d\mathbf{r}'}{|\mathbf{r} - \mathbf{r}'|}, \tag{1.2}$$

where $t' = t - |\mathbf{r} - \mathbf{r}'| / \nu_{s0}$. The source term $H(\mathbf{r}, t)$ can further be written as the product of a spatial component and a temporal component,

$$H(\mathbf{r}, t) = I_0 \varphi(\mathbf{r}) \eta(t), \tag{1.3}$$

where I_0 is a scaling factor proportional to the incident radiation intensity; $\varphi(\mathbf{r}')$ describes the to-be-reconstructed microwave absorption properties of the medium at $\mathbf{r}'$; and $\eta(t)$ describes the shape of the irradiating pulse. Substituting (1.3) into (1.2) results in

$$p(\mathbf{r}, t) = \frac{\beta I_0}{4\pi C} \iiint \varphi(\mathbf{r}') \frac{d\eta(t')}{dt'} \frac{d\mathbf{r}'}{|\mathbf{r} - \mathbf{r}'|}. \tag{1.4}$$

We proceed by transforming the time-dependent wave equation into the temporal-frequency domain. Denoting the Fourier transforms of p and η by $\bar{p}$ and $\bar{\eta}$, respectively, we have

$$\begin{aligned} p(\mathbf{r}, t) &= \int_{-\infty}^{\infty} \bar{p}(\mathbf{r}, \omega) \exp(i\omega t) d\omega, \\ \eta(t) &= \int_{-\infty}^{\infty} \bar{\eta}(\omega) \exp(i\omega t) d\omega. \end{aligned} \tag{1.5}$$

Substituting (1.5) into (1.4) results in

$$\bar{p}(\mathbf{r}, \omega) = \frac{i\beta I_0 \omega \bar{\eta}(\omega)}{4\pi C} \iiint \varphi(\mathbf{r}') \frac{\exp(-i\omega \left|\mathbf{r} - \mathbf{r}'\right| / \nu_{s0})}{|\mathbf{r} - \mathbf{r}'|} d\mathbf{r}'. \tag{1.6}$$

Define $\bar{p}_1(\mathbf{r}, \omega) = \bar{p}(\mathbf{r}, \omega)/(2\pi\bar{\eta}(\omega))$; substitute it into (1.6); apply an inverse Fourier transform to both sides of the equation, and obtain the following equation:

$$p_1(\mathbf{r}, t) = \frac{\beta I_0 v_{s0}}{4\pi C} \frac{\partial}{\partial t} \iint\limits_{t = t_f(\mathbf{r}', \mathbf{r})} \frac{\varphi(\mathbf{r}')}{|\mathbf{r} - \mathbf{r}'|} d\mathbf{r}', \tag{1.7}$$

where

$$t_f(\mathbf{r}', \mathbf{r}) = \left|\mathbf{r} - \mathbf{r}'\right| / \nu_{s0} \tag{1.8}$$

is the time-of-flight (TOF) from $\mathbf{r}'$ to $\mathbf{r}$; $p_1(\mathbf{r}, t)$ is the deconvolution of $p(\mathbf{r}, t)$ with respect to the profile of the microwave pulse and can be interpreted as the detected pressure signal when the microwave pulse is infinitely narrow. The physical meaning of this equation is that, in an acoustically homogenous medium, the pressure p_1, at a spatial point $\mathbf{r}$ and time t, is proportional to the first-order temporal derivative of the integration of the absorbed microwave energy over a spherical surface [a circle in the two-dimensional (2-D) case]. The spherical surface is centered at $\mathbf{r}$ and has a radius of tv_{s0}.

D. OUTLINE

In this thesis, I first derive exact reconstuction algorithms for TAT and broadband diffraction tomography using developed time-reversal techniques [21]. Then I will focus on some important practical problems of TAT including limited-view problem [22], effects of acoustic heterogeneity [23], and fast reconstruction algorithms [24, 25].

In Chapter II, we develop time-reversal methods and apply them to deriving exact reconstruction algorithms for broadband UT and TAT in an arbitrary configuration for the first time [21]. Before our work, developing reconstruction methods in TWDS has been a craft work. The derivation of an algorithm depends strongly on the specific illumination and detection geometry and exact reconstruction algorithms are only available in a few special geometries. Although the concept of time reversal (more generally known as backpropagation) has been used in developing reconstruction algorithm, no exact reconstruction algorithm is available using only the measured field on a closed surface. This is because the available time-reversal formulas [26, 27] requires both the field and its normal gradient on a closed surface enclosing the initial sources. However, it is not practical to measure both the field and its normal gradient simultaneously. In Chapter II, we find that when time reversal is considered in the time domain, exact time-reversal methods that use only the field on an arbitrary closed surface can be derived for a wide variety of applications such as tomography with diffracting sources, inverse diffraction, and ultrasound therapy. Then the reconstruction in UT and TAT can be developed by time-reversing the acoustic field to the time when the to-be-reconstructed point is excited. By using time-reversal concept, the reconstruction in different branches of TWDS can be derived in a uniform framework. Furthermore, the proposed time-reversal methods can be applied in other studies such as inverse diffraction, ultrasound therapy, and other time-reversal applications.

The TAT reconstruction algorithms developed in Chapter II are based on two assumptions. The first one is that the thermoacoustic signals are detected in a full (panoramic) view. In other words, the detector moves along a whole circle in the 2-D case or sphere in the three-dimensional (3-D) case. This means in particular that each point of the scanned object is visible from the detector's trajectory for 2π radians in the 2-D case or 4π steradians in the 3-D case. However, in many applications of TAT, the signals cannot be collected from all directions. For example, the solid angle of detection is at most 2π steradians for a breast. So, one faces here an incomplete data problem. In Chapter III, we define a "detection region," within which all points have sufficient detection views. It is explained analytically and shown numerically that the boundaries of any objects inside this region can be recovered stably. Otherwise some sharp details become blurred. One can identify in advance the parts of the boundaries that will be affected if the detection view is insufficient. If the detector scans along a circle in a two-dimensional case, acquiring a sufficient view might require covering more than a π-, or less than a π-arc of the trajectory depending on the position of the object. Similar results hold in a three-dimensional case. In order to support our theoretical conclusions, three types of reconstruction methods are utilized: a filtered backprojection (FBP) approximate inversion, which is shown to work well for limited-view data, a local-tomography-type reconstruction that emphasizes sharp details (e.g., boundaries of inclusions), and an iterative algebraic truncated conjugate gradient algorithm used in conjunction with FBP. Computations are conducted for both numerically simulated and experimental data. The reconstructions confirm our theoretical predictions.

The second assumption is that the tissue is acoustically homogeneous. For many medical imaging applications, including imaging of the female breast, this assumption is an approximation. For example, the speed of sound in the breast can vary from 1400 m/s to 1550 m/s. Errors due to the assumption of a constant acoustic speed, which has never been studied in TAT, can potentially have a pronounced effect on image quality. In Chapter IV, The effects of wavefront distortions induced by acoustic heterogeneities in breast thermoacoustic tomography (TAT) are studied [23]. Firstly, amplitude distortions are shown to be insignificant for different scales of acoustic heterogeneities. For wavelength-scale, or smaller heterogeneities, amplitude distortion of the wavefront is minor as a result of diffraction when the detectors are placed in the far field of the heterogeneities. For larger-scale heterogeneities at the parenchyma wall, by using a ray approach (geometric optics), we show that no refraction-induced multipath interference occurs and, consequently, that no severe amplitude distortion, like is found in ultrasound tomography, exists. Next, we consider the effects of phase distortions (errors in time-of-flight) in our numerical studies. The numerical results on the spreads of point sources and boundaries caused by the phase distortions are in good agreement with the proposed formula. After that, we demonstrate that the blurring of images can be compensated for by using the distribution of acoustic velocity in the tissues in the reconstructions. The effects of the errors in the acoustical velocities on this compensation are also investigated. An approach to implement the compensation using only TAT data is proposed. At last, the differences in the effects of acoustic heterogeneity and the generation of speckles in breast TAT and breast ultrasound imaging are discussed.

The above reconstruction algorithms are implemented in the time domain. The reconstruction of an image by Fourier transform has been used in X-ray CT [28], ultrasonic reflectivity imaging [29] and diffraction tomography [30] successfully. The computation complexity is reduced greatly due to the efficiency of the Fourier transform. Then, in Chapter V, we develop exact and fast Fourier-domain reconstruction algorithms for thermoacoustic tomography in planar and cylindrical configurations. This is important for real-time 3-D imaging.

CHAPTER II

TIME REVERSAL AND ITS APPLICATION TO TOMOGRAPHY WITH DIFFRACTING SOURCES[1]

A. INTRODUCTION

Time reversal of an acoustic or electromagnetic wave is based on the invariance of the wave equation in a lossless medium under the transform $t \rightarrow -t$ (t represents the time). Time reversal of a wave can be understood as generating the back-propagation field from the measured forward-propagation field and/or its normal derivative after removing the initial sources. The concept of time reversal has been implemented experimentally and applied to a wide range of studies such as inverse scattering [31, 32, 33], wavefront distortion correction [27, 34], and multiple scattering phenomena [35].

However, no formula is available for computing the time-reversed field using only the measured field on a closed surface enclosing the initial source. When both the field and its normal gradient on a closed surface are available, there are formulas [26, 27] to derive the time-reversed field. However, it is not practical to measure both the field and its normal gradient simultaneously. There are two challenges in deriving the time-reversed field using only the field. First, it is not obvious that Green function, which is widely used to derive the field in space from the field on a closed surface, can be applied here. This is because the time-reversed field on the closed surface includes both diverging and converging components [26, 27]. While the converging component of the time-reversed wave is just the measured signals in the forward

---

[1] Y. Xu and L.-H. Wang, Phys. Rev. Lett., accepted, 2003. Copyright (2003) by the American Physical Society.

propagation with reverse temporal order, the diverging component has no counterpart in the forward propagation and, consequently, is not available from measurement in general. Secondly, in a free space, retransmission of the measured signals in reversed temporal order from the detection surface will not reproduce the time-reversed field. This is because the waves retransmitted in one position will propagate to the other positions on the surface and change the field there, and consequently the field on the surface will not equal the field in the forward propagation in reversed temporal order.

In this chapter, we find that when time reversal is considered in the time domain, exact time-reversal methods that use only the field on an arbitrary closed surface can be derived for a wide variety of applications such as tomography with diffracting sources, inverse diffraction, and ultrasound therapy. Under certain conditions, a time-reversed field can be approximated by retransmitting the measured signals in reversed temporal order in a free space. Acoustic waves are used as an example to present our results and methods, but their application to other scalar or vector waves is straightforward.

Next, we show that exact reconstruction for broadband diffraction tomography (DT) [36, 37, 38, 39, 40] and TAT can be essentially represented by a time-reversal process. Although exact reconstruction algorithms have been proposed for DT and TAT in some special geometries, no exact algorithm for broadband DT and TAT using only pressure measured on an arbitrary closed surface has been proposed. In the forward problem of our DT model, the objects [shaded in (Fig. 1)] are irradiated by an illuminating source of $\delta(t)\delta(\mathbf{r}-\mathbf{r}_s)$ at $\mathbf{r}_s$, and the scattered field is measured on an arbitrary closed surface Σ enclosing the objects to reconstruct their heterogeneity. This DT model is a single-view one; therefore, it is very efficient for collecting data.

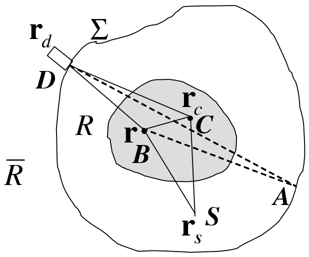

Fig. 1. Illustration of diffraction tomography. S represents the illuminating source, D represents a detector scanning across surface Σ, and the to-be-imaged object is shaded. R and $\bar{R}$ are the space inside and outside Σ, respectively.

The total field in an acoustically heterogeneous medium is [41]:

$$\bar{p}_t(\mathbf{r},\omega) = \bar{p}_{in}(\mathbf{r},\omega) + \oint_R d\mathbf{r}_1 \omega^2 \gamma(\mathbf{r}_1) \bar{p}_t(\mathbf{r}_1,\omega) G_\omega(\mathbf{r}\,|\mathbf{r}_1\,)/v_s^2 \ , \tag{2.1}$$

where $\bar{p}_t(\mathbf{r},\omega)$ and $\bar{p}_{in}(\mathbf{r},\omega)$ are the temporal spectrum of the total pressure field and the incidence field, respectively; $\gamma(\mathbf{r}) = (\kappa - \kappa_0)/\kappa_0$ describes the normalized deviation of compressibility κ from the average κ_0; $G_\omega(\mathbf{r}\,|\mathbf{r}_0\,) = \exp(-i\omega\,|\mathbf{r}-\mathbf{r}_0|\,/v_s)/(4\pi\,|\mathbf{r}-\mathbf{r}_0|)$; $\bar{p}_{in}(\mathbf{r},\omega) = G_\omega(\mathbf{r}\,|\mathbf{r}_s\,)$ is the incident wave. Now we define a normalized scattered field as $\bar{p}_n(\mathbf{r},\omega) = [\bar{p}_t(\mathbf{r},\omega) - \bar{p}_{in}(\mathbf{r},\omega)]v_s^2/\omega^2$ and rewrite (2.1) as

$$\bar{p}_n(\mathbf{r},\omega) = \oint_R d\mathbf{r}_1 \gamma(\mathbf{r}_1) \bar{p}_t(\mathbf{r}_1,\omega) G_\omega(\mathbf{r}\,|\mathbf{r}_1\,) \ . \tag{2.2}$$

It is easy to see that point $\mathbf{r}_1$ of the objects can be considered as a secondary source $\gamma(\mathbf{r}_1)\bar{p}_t(\mathbf{r}_1,\omega)$ for $\bar{p}_n$. In our reconstruction of DT, we first time-reverse $\bar{p}_n$ back to time $t_e(\mathbf{r}) = |\mathbf{r}-\mathbf{r}_s|\,/v_s$ at point $\mathbf{r}$ (v_s is the acoustic speed and $t_e(\mathbf{r})$ is the time the secondary source at $\mathbf{r}$ is excited) and then derive the heterogeneity. Here, we first derive the formulas for time-reversing a wave in a homogeneous medium and treat DT under first Born approximation (FBA), which involves replacing $\bar{p}_t(\mathbf{r}_1,\omega)$ with $\bar{p}_{in}(\mathbf{r}_1,\omega)$ on the right-hand side of (2.2). Then the extensions of the results to the case using Green function in a heterogeneous medium are discussed.

B. TIME REVERSAL OF A WAVE

1. Definition of Time Reversal

We start from the wave equation for pressure $p_0(\mathbf{r}, t)$

$$\nabla^2 p_0(\mathbf{r}, t) - \frac{1}{v_s^2}\frac{\partial^2 p_0(\mathbf{r}, t)}{\partial t^2} = -q(\mathbf{r}, t) \ , \tag{2.3}$$

where $q(\mathbf{r}, t)$ is the source term and is nonzero only in R [the space enclosed by the detection surface Σ (Fig. 1)] and within the time period $[0, T_s]$. The pressure field can be expressed as

$$p_0(\mathbf{r}, t) = \int_0^{T_s} dt_0 \oint_R d\mathbf{r}_0 q(\mathbf{r}_0, t_0) g_+(\mathbf{r}, t \left|\mathbf{r}_0, t_0\right.) \ , \tag{2.4}$$

where $g_\pm(\mathbf{r}, t\left|\mathbf{r}_0, t_0\right.) = \delta(t - t_0 \mp \left|\mathbf{r} - \mathbf{r}_0\right| / v_s) \,/ (4\pi \left|\mathbf{r} - \mathbf{r}_0\right|)$ is a diverging (g_+) or converging (g_-) Green function of the wave equation.

In this chapter, time reversal of $p_0(\mathbf{r}, t)$ at time T_0, is defined as

$$p_r(\mathbf{r}, T_0) = p_0(\mathbf{r}, T_0), p_r'(\mathbf{r}, T_0) = -p_0'(\mathbf{r}, T_0) \ , \tag{2.5}$$

where prime represents the temporal derivative in this chapter; $p_r(\mathbf{r}, t)$ is the time-reversed field of $p_0(\mathbf{r}, t)$; and T_0 is chosen to be large enough so that $p_0(\mathbf{r}, t) = 0$ for $\mathbf{r} \in R, t \geqslant T_0$. Then, $p_r(\mathbf{r}, t)$ can be uniquely determined by the initial conditions at T_0. The above definition of time reversal is analogous to the fact that a particle will move back along its trajectory if its velocity is reversed and position unchanged. According to this definition, we mean $p_r(\mathbf{r}, \hat{t})$ when we say time-reversing a field back to time t, where a hat over a time variable t represents $2T_0 - t$ in this chapter.

2. Time Reversal in the Case of a Point Source

In the case of a point source $\delta(\mathbf{r}-\mathbf{r}_0)\delta(t-t_0)$ in R, (2.5) becomes $g_r(\mathbf{r},T_0) = g_+(\mathbf{r},T_0\left|\mathbf{r}_0,t_0\right.)$, $g_r'(\mathbf{r},T_0) = -g_+'(\mathbf{r},T_0\left|\mathbf{r}_0,t_0\right.)$. It can be easily verified that the time-reversed field

$$\begin{aligned} g_r(\mathbf{r},t\left|\mathbf{r}_0,t_0\right.) &= g_-(\mathbf{r},t\left|\mathbf{r}_0,\hat{t_0}\right.) \\ &\quad -g_+(\mathbf{r},t\left|\mathbf{r}_0,\hat{t_0}\right.), t \geqslant T_0 \ , \end{aligned} \tag{2.6}$$

because it satisfies both the homogeneous wave equation and the initial-value conditions shown above. This result is also obtained by Cassereau [27] and Porter [26] . The physical meaning of (2.6) is that if we time-reverse, at T_0, the field of a point source which is located at $\mathbf{r}_0$ and excited at t_0, the time-reversed field converges to $\mathbf{r}_0$ at time $\hat{t_0}$, and then diverges with an opposite amplitude. The diverging wave $g_+(\mathbf{r},t\left|\mathbf{r}_0,\hat{t_0}\right.)$, however, does not have a counterpart in the forward propagation. It exists because, unlike the forward propagation, there is no source inside Σ for $g_r(\mathbf{r},t)$. The diverging wave with an opposite amplitude exactly cancels the source term related to the converging one.

3. Time Reversal in the Case of an Arbitrary Source

In the case of an arbitrary source, similar results can be obtained after considering the linearity of the wave equation with respect to the source

$$p_r(\mathbf{r},t) = \int_0^{T_s} dt_0 \oint_R d\mathbf{r}_0 q(\mathbf{r}_0,t_0) g_r(\mathbf{r},t\left|\mathbf{r}_0,t_0\right.) \ . \tag{2.7}$$

After substituting (2.6) into (2.7), using $g_-(\mathbf{r}, t\,|\mathbf{r}_0, t_0) = g_+(\mathbf{r}, -t\,|\mathbf{r}_0, -t_0)$, and variable transform, we have for $\mathbf{r}_d \in \Sigma$ (although it is valid for any $\mathbf{r}$)

$$\begin{aligned} p_r(\mathbf{r}_d, t) &= p_0(\mathbf{r}_d, 2T_0 - t) + p_{out}(\mathbf{r}_d, t) \ , \qquad (2.8) \\ p_{out}(\mathbf{r}_d, t) &= -\int_{2T_0 - T_s}^{2T_0} dt_0 \oint_R d\mathbf{r}_0 q(\mathbf{r}_0, \hat{t_0}) g_+(\mathbf{r}_d, t\,|\mathbf{r}_0, t_0) \ . \end{aligned}$$

As in the case of a point source, the diverging component $p_{out}(\mathbf{r}_d, t)$ has no counterpart in the forward propagation and is, in general, not available from the experimental measurements of p_0 except in some special cases. Nevertheless, we will be showing that $p_r(\mathbf{r}, t)$ before a specified time can be derived using only $p_0(\mathbf{r}_d, t)$.

C. TIME-REVERSAL METHODS

Since there is no source for $p_r(\mathbf{r}, t)$ and $p_r(\mathbf{r}, T_0) = 0$ in R, $p_r(\mathbf{r}, t)$ in R can be expressed in terms of the field on Σ [42]:

$$p_r(\mathbf{r}, t) = -\int_{T_0}^{t^+} dt_0 \oint_\Sigma dS_d p_r(\mathbf{r}_d, t_0) \frac{\partial g_1(\mathbf{r}, t\,|\mathbf{r}_d\ , t_0)}{\partial n} \ , \qquad (2.9)$$

where $\mathbf{n}$ is a unity vector along the normal of Σ at $\mathbf{r}_d$ pointing away from the volume R; $g_1(\mathbf{r}, t\,|\mathbf{r}_0, t_0)$ with $\mathbf{r}, \mathbf{r}_0 \in (R \cup \Sigma)$ is Green function subject to the homogeneous Dirichlet boundary condition on Σ and explicit expression of g_1 in the form of series of eigenfunctions can be found for the boundaries that fit with separable coordinates [42]. Here, we will show that $p_{ro}(\mathbf{r}, t)$, the contribution of $p_{out}(\mathbf{r}_d, t_0)$ to the right-hand side of (2.9), is zero before a specified time. After inserting (2.8) into (2.9), we have

$$\begin{aligned} p_{ro}(\mathbf{r}, t) \ &= \ \int_{T_0}^{t^+} dt_0 \oint_\Sigma dS_d \int_{2T_0 - T_s}^{2T_0} dt_c \oint_R d\mathbf{r}_c q(\mathbf{r}_c, \hat{t}_c) \\ &\quad \times g_+(\mathbf{r}_d, t_0\,|\mathbf{r}_c, t_c)\ \frac{\partial g_1(\mathbf{r}, t\,|\mathbf{r}_d\ , t_0)}{\partial n} \ . \qquad (2.10) \end{aligned}$$

Considering $g_+(\mathbf{r}_d, t_0 \left| \mathbf{r}_c, t_c \right.) = 0$ when $t_0 < t_c + \left| \mathbf{r}_c - \mathbf{r}_d \right| / v_s$, and $g_1(\mathbf{r}, t \left| \mathbf{r}_d, t_0 \right.) = 0$ when $t < t_0 + \left| \mathbf{r} - \mathbf{r}_d \right| / v_s$, and assuming that $q(\mathbf{r}_c, t_c)$ is nonzero only within the period $[t_c^1, t_c^2]$, we conclude that $p_{ro}(\mathbf{r}, t) = 0$ if for any $\mathbf{r}_c \in R$ and $\mathbf{r}_d \in \Sigma$

$$t < 2T_0 - t_c^2 + \left| \mathbf{r}_d - \mathbf{r}_c \right| / v_s + \left| \mathbf{r} - \mathbf{r}_d \right| / v_s \ . \tag{2.11}$$

Actually, $p_{ro}(\mathbf{r}, t)$ can be shown to be equivalent to the field induced by the reflection of the diverging field $p_{out}(\mathbf{r}, t)$ by Σ. It contributes only to the late part of $p_r(\mathbf{r}, t)$. In many applications including tomography with diffracting sources and ultrasound therapy, it can be shown that we are only interested in the part of $p_r(\mathbf{r}, t)$ within the range defined by (2.11). For example, let us consider our broadband DT model. As will be shown in (2.20), the heterogeneity at point $\mathbf{r}$ in Fig. 1 can be derived from $p_r(\mathbf{r}, \hat{t}_e(\mathbf{r}))$. After noticing $\left| t_e(\mathbf{r}) - t_e(\mathbf{r}_c) \right| \leqslant \left| \mathbf{r} - \mathbf{r}_c \right| / v_s$ and $t_c^1 = t_c^2 = t_e(\mathbf{r}_c)$, it can be found that (2.11) is minimally observed for any $\mathbf{r}_c \in R$ and $\mathbf{r}_d \in \Sigma$ to compute $p_r(\mathbf{r}, \hat{t}_e(\mathbf{r}))$ in DT. Similarly, it can be found that (2.11) can be easily met for other applications such as thermoacoustic tomography and ultrasound therapy. Therefore, $p_r(\mathbf{r}, t)$, within the range defined by (2.11), can be expressed as

$$p_r(\mathbf{r}, t) = - \int_{T_0}^{t^+} dt_0 \oint_{\Sigma} dS_d p_0(\mathbf{r}_d, \hat{t_0}) \frac{\partial g_1(\mathbf{r}, t \left| \mathbf{r}_d \right., t_0)}{\partial n} \ . \tag{2.12}$$

The physical meaning of (2.12) is that the time-reversed field before a certain time in R is equivalent to the field (caused by the retransmission of $p_0(\mathbf{r}_d, t)$ from Σ in reversed temporal order) in a reflective cavity (formed by Σ) rather than in the free space. Therefore, the reflections from Σ will also contribute to $p_r(\mathbf{r}, t)$. The reason is that the field transmitted in one position on Σ will propagate to the other positions on Σ, and, consequently, the field in these positions will change. The reflections from Σ will cancel the changes in these positions.

Next, we will show that the reflections from Σ can be approximately ignored under certain conditions. The central concept is that $g_1(\mathbf{r}, t\,|\mathbf{r}_d\,, t_0)$ can be obtained in a model where the boundary Σ serves as a perfect mirror (with a phase shift of π after reflection), and a delta pulse source is launched at $\mathbf{r}_d$ and time t_0. Under the ray approach (geometrical optics approximation), $g_1(\mathbf{r}, t\,|\mathbf{r}_d\,, t_0)$ is the summation of the contributions from all the rays that go from $\mathbf{r}_d$ and arrive at $\mathbf{r}$ if the radii of Σ are much larger than the wavelength of the excitation pulse. As shown in Fig. 1, the first ray from $\mathbf{r}_d$ to $\mathbf{r}$ travels along the line connecting $\mathbf{r}_d$ and $\mathbf{r}$. The second ray is first reflected by the boundary at $\mathbf{r}_d$ and then goes to $\mathbf{r}$. Both of them arrive at $\mathbf{r}$ at time $t_0 + |\mathbf{r} - \mathbf{r}_d|/v_s$. The contribution of the first two rays to $\partial g_1/\partial n$ in (2.12) is $2\partial g_+/\partial n$. Then there will be other rays (for example, the dashed line in Fig. 1) that are reflected at other points on the boundary such as A. In DT, it is shown in Appendix A that when the to-be-reconstructed point $\mathbf{r}$ is around the center of Σ, and $l_{\det} > 2l_{obj}$, where $l_{\det}$ is the average linear dimension of Σ and l_{obj} is the maximum linear dimension of the object, $p_r(\mathbf{r}, \hat{t}_e(\mathbf{r}))$ can be approximated well after replacing $\partial g_1/\partial n$ in (2.12) with $2\partial g_+/\partial n$

$$p_r(\mathbf{r}, t) \approx -2\int_{T_0}^{t^+} dt_0 \oint_{\Sigma} dS_d p_0(\mathbf{r}_d, \hat{t_0}) \frac{\partial g_+(\mathbf{r}, t\,|\mathbf{r}_d\,, t_0)}{\partial n}\,. \tag{2.13}$$

The physical meaning of (2.13) is that under certain conditions, time reversal can be approximated well by retransmission of the measured signals in reversed temporal order from the detection surface in a free space. (2.13) also holds for applications other than DT when appropriate $l_{\det}$ is chosen by using the demonstrated method for DT. (2.13) can be transformed into

$$\begin{aligned} p_r(\mathbf{r}, t) \;\; &\approx \;\; \frac{1}{2\pi} \oint_{\Sigma} dS_d \frac{\mathbf{n}\cdot(\mathbf{r}_d - \mathbf{r})}{|\mathbf{r} - \mathbf{r}_d|^2} [\frac{p_0(\mathbf{r}_d, t_{rd})}{|\mathbf{r} - \mathbf{r}_d|} \\ &\quad -p_0'(\mathbf{r}_d, t_{rd})/v_s]\,, \end{aligned} \tag{2.14}$$

where $t_{rd} = 2T_0 - t + |\mathbf{r} - \mathbf{r}_d| / v_s$. (2.14) is in the form of the well-known delay-and-sum algorithm (backprojection to spheres) used in synthetic aperture imaging. Consequently, the physical meaning and the valid conditions of this widely used algorithm are revealed quantitatively for the first time from basic physics.

D. RECONSTRUCTION IN DT

Now we will discuss the reconstruction in DT. In the forward propagation, the secondary sources (the points of the objects) are not excited at the same time, since the incidence wave reaches different points at different times. Therefore, in the time-reversed field, the diverging waves from some secondary sources mingle with the converging waves from other secondary sources according to (2.6). Nevertheless, we will show that there is a strikingly simple relationship between the time-reversed field and the heterogeneity under FBA. After combining (2.2), (2.6), and (2.7) and the application of inverse Fourier transform, the time-reversed field of $\bar{p}_n(\mathbf{r}, \omega)$ at time $\hat{t}_e(\mathbf{r})$ is

$$\begin{aligned} p_{nr}(\mathbf{r}, \hat{t}_e(\mathbf{r})) &= \oint_R d\mathbf{r}_1 \gamma(\mathbf{r}_1) \int_{-\infty}^{\infty} dk \exp(-ik\,|\mathbf{r} - \mathbf{r}_s|) \\ &\quad \times \bar{p}_t(\mathbf{r}_1, -\omega)[G^*_\omega(\mathbf{r}\,|\mathbf{r}_1) - G_\omega(\mathbf{r}\,|\mathbf{r}_1)] , \end{aligned} \tag{2.15}$$

where * represents the complex conjugate and $k = \omega / v_s$. Let's define $\varphi_1(\mathbf{r}) = |\mathbf{r} - \mathbf{r}_s|\, p_{nr}(\mathbf{r}, \hat{t}_e(\mathbf{r}))$. After applying FBA we have

$$\begin{aligned} \varphi_1(\mathbf{r}) &= \frac{1}{4\pi} \oint_R d\mathbf{r}_1 \gamma(\mathbf{r}_1) \int dk \{ \frac{|\mathbf{r} - \mathbf{r}_s| \exp\left[-ik(|\mathbf{r} - \mathbf{r}_s| - |\mathbf{r}_s - \mathbf{r}_1| - |\mathbf{r} - \mathbf{r}_1|)\right]}{4\pi\,|\mathbf{r} - \mathbf{r}_1|\,|\mathbf{r}_s - \mathbf{r}_1|} \\ &\quad - \frac{|\mathbf{r} - \mathbf{r}_s| \exp[-ik(|\mathbf{r} - \mathbf{r}_s| - |\mathbf{r}_s - \mathbf{r}_1| + |\mathbf{r} - \mathbf{r}_1|)]}{4\pi\,|\mathbf{r} - \mathbf{r}_1|\,|\mathbf{r}_s - \mathbf{r}_1|} \} . \end{aligned} \tag{2.16}$$

We denote the contribution of the first term in the integrant on the right-hand side of (2.16) to $\varphi_1(\mathbf{r})$ as $\varphi_1^+(\mathbf{r})$. After the integration over k, we have

$$\varphi_1^+(\mathbf{r}) = \frac{1}{2}\oint_R d\mathbf{r}_1\gamma(\mathbf{r}_1)\frac{|\mathbf{r}-\mathbf{r}_s|\,\delta(|\mathbf{r}-\mathbf{r}_s|-|\mathbf{r}_s-\mathbf{r}_1|-|\mathbf{r}-\mathbf{r}_1|)}{4\pi\,|\mathbf{r}-\mathbf{r}_1|\,|\mathbf{r}_s-\mathbf{r}_1|}\ . \tag{2.17}$$

It can be found that $\mathbf{r}_1$ has to fall in the line between $\mathbf{r}_s$ and $\mathbf{r}$ to make the δ function nonzero. Without losing generality, assume $\mathbf{r}-\mathbf{r}_s$ is in the z direction and $\mathbf{r}_s$ is the original point, and we can compute the above integration in a spherical coordinate system

$$\begin{aligned}
\varphi_1^+(\mathbf{r}) &= \frac{1}{2}\oint_R d\phi d\theta\sin(\theta)dr_1r_1\gamma(\mathbf{r}_1)\frac{r\delta(r-r_1-\sqrt{r^2+r_1^2-2rr_1\cos(\theta)}}{4\pi\sqrt{r^2+r_1^2-2rr_1\cos(\theta)}} \\
&= \frac{1}{2}\int dr_1r_1\int_0^\pi d\theta\sin(\theta)\gamma(\mathbf{r}_1)\frac{r}{2\sqrt{r^2+r_1^2-2rr_1\cos(\theta)}} \\
&\quad\times\delta(\frac{2rr_1(1-\cos(\theta))}{r-r_1+\sqrt{r^2+r_1^2-2rr_1\cos(\theta)}}) \\
&= \frac{1}{8}\int_0^\infty dr_1\gamma(\mathbf{r}_1)\frac{|r-r_1+|r-r_1||}{2\,|r-r_1|} \\
&= \frac{1}{8}\int_0^r dr_1\gamma(\mathbf{r}_1)\ .
\end{aligned} \tag{2.18}$$

Similarly, we can obtain the second part of the integration in (2.16)

$$\varphi_1^-(\mathbf{r}) = -\frac{1}{8}\int_r^\infty dr_1\gamma(\mathbf{r}_1)\ . \tag{2.19}$$

At last, we have

$$\gamma(\mathbf{r}) = 4\frac{\partial[|\mathbf{r}-\mathbf{r}_s|\,p_{nr}(\mathbf{r},\hat{t}_e(\mathbf{r}))]}{\partial\,|\mathbf{r}-\mathbf{r}_s|}\ . \tag{2.20}$$

Therefore, the reconstruction in DT can be implemented by first time-reversing p_n to obtain $p_{nr}(\mathbf{r},\hat{t}_e(\mathbf{r}))$ with (2.12) or (2.13), and then obtaining $\gamma(\mathbf{r})$ with (2.20). A numerical simulation of three-dimensional DT is implemented to support our theoretical conclusions. The object is a sphere with a radius of 8 mm that is located at the origin, and $\gamma(\mathbf{r})$ is set to be unity in the sphere and zero otherwise. The illuminating

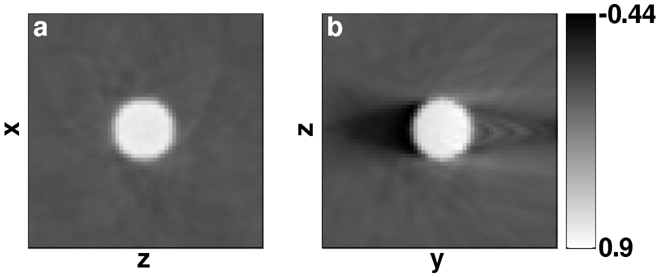

Fig. 2. Reconstructed image sections in DT along the (a) $y = 0$ and (b) $x = 0$ planes, respectively.

point source is at [0, 64, 0] mm. The detection surface is an ellipsoid with three axis lengthes of [80, 64, 80] mm and centered at the origin. 4096 detection positions are randomly distributed over the detection ellipsoid. The imaging space is a cube with a side length of 62 mm, centered at the origin, and mapped with a 62 by 62 by 62 mesh. In the forward problem, $p_n(\mathbf{r}, t)$ is computed by the integration of the object value along a series of ellipsoids. In the inverse problem, we use (2.14) instead of the exact formula (2.12) to time-reverse fields due to the consideration of computation efficiency. Fig. 2(a)-(b) shows the reconstructed image section along the $y = 0$ and $x = 0$ planes, respectively. It can be found that the object value is reconstructed quantitatively. There are some shadows from the object along the y axis in Fig. 2(b). The shadows are probably caused by the limited bandwidth of the simulated signals. They can be eliminated if the illuminating source is placed in several positions and multiple sets of data are collected.

E. TIME REVERSAL AND DT IN A HETEROGENEOUS MEDIUM

1. Time Reversal in a Heterogeneous Medium

Our time-reversal methods are derived for waves in a homogeneous medium. The extension of most of them to a heterogeneous medium is straightforward. (2.4)-(2.9) hold for a heterogeneous medium after Green function is replaced by the corresponding one in a heterogeneous medium. In this case, g_- is defined as

$$g_-(\mathbf{r}, t\,|\mathbf{r}_0, t_0) = g_+(\mathbf{r}, -t\,|\mathbf{r}_0, -t_0) \ . \tag{2.21}$$

In addition to replacing Green function, v_s in (2.11) should be understood as the maximum of the acoustic speed in the medium to extend (2.10)-(2.12). (2.13) can be extended after the minimum requirement for l_{det} is estimated. This estimation is more complex in a heterogeneous medium, since Green function in a heterogeneous medium is usually a wave train rather than a delta pulse. To proceed from (2.13) to (2.14), we need to assume that the heterogeneity changes only the flight time of a transient wave but not its shape. This assumption is usually valid in a weakly-scattering application such as when a low-frequency ultrasonic pulse is used to image soft tissue. In this case, g is approximated as

$$g_\pm(\mathbf{r}, t\,|\mathbf{r}_0, t_0) = \delta(t - t_0 \mp t_f(\mathbf{r}, \mathbf{r}_d)) \,/ (4\pi\,|\mathbf{r} - \mathbf{r}_0|) \ , \tag{2.22}$$

where $t_f(\mathbf{r}, \mathbf{r}_0)$ is the flight time from $\mathbf{r}_0$ to $\mathbf{r}$. Then (2.14) can be extended to a heterogeneous medium after replacing $|\mathbf{r} - \mathbf{r}_d|\,/v_s$ in (2.14) with $t_f(\mathbf{r}, \mathbf{r}_0)$.

2. DT in a Heterogeneous Medium

When g is approximated as (2.22), we can obtain similar reconstruction formula for DT using Green function in a heterogeneous medium along the same line of deriving (2.20). In the heterogeneous case, we need to the time-reverse $\bar{p}_n(\mathbf{r}, k)$ back to time $t_f(\mathbf{r}, \mathbf{r}_s)$. In the heterogeneous case, (2.16) becomes

$$\begin{aligned}\varphi_1(\mathbf{r}) \;=\; & \frac{1}{4\pi}\oint_R d\mathbf{r}_1 \gamma(\mathbf{r}_1) \int dk \Big\{ \frac{|\mathbf{r} - \mathbf{r}_s| \exp\left[-ik(t_f(\mathbf{r}, \mathbf{r}_s) - t_f(\mathbf{r}_s, \mathbf{r}_1) - t_f(\mathbf{r}, \mathbf{r}_1))\right]}{4\pi\,|\mathbf{r} - \mathbf{r}_1|\,|\mathbf{r}_s - \mathbf{r}_1|} \\ & - \frac{|\mathbf{r} - \mathbf{r}_s| \exp[-ik(t_f(\mathbf{r}, \mathbf{r}_s) - t_f(\mathbf{r}_s, \mathbf{r}_1) + t_f(\mathbf{r}, \mathbf{r}_1))]}{4\pi\,|\mathbf{r} - \mathbf{r}_1|\,|\mathbf{r}_s - \mathbf{r}_1|} \Big\} \ . \end{aligned} \tag{2.23}$$

We will first consider the first part of the integration. After the integration over k, we have

$$\varphi_1^+(\mathbf{r}) = \frac{1}{2}\oint_R d\mathbf{r}_1 \gamma(\mathbf{r}_1) \frac{|\mathbf{r}-\mathbf{r}_s|\,\delta(t_f(\mathbf{r},\mathbf{r}_s) - t_f(\mathbf{r}_s,\mathbf{r}_1) - t_f(\mathbf{r},\mathbf{r}_1))}{4\pi\,|\mathbf{r}-\mathbf{r}_1|\,|\mathbf{r}_s-\mathbf{r}_1|} \tag{2.24}$$

Now, it can found that only only $\mathbf{r}_1$ within $l(\mathbf{r}_s,\mathbf{r})$ contributes to the above integration according to Fermats' principle, where $l(\mathbf{r}_s,\mathbf{r})$ is the ray path from $\mathbf{r}_s$ to $\mathbf{r}$. By an analog with (2.18)

$$\varphi_1^+(\mathbf{r}) \approx \frac{1}{8}\oint_{l(\mathbf{r}_s,\mathbf{r})} dr_1 \gamma(\mathbf{r}_1)\ . \tag{2.25}$$

Finally, we have

$$\gamma(\mathbf{r}) \approx 4\mathbf{n}_l \cdot \nabla_{\mathbf{r}}[|\mathbf{r}-\mathbf{r}_s|\, p_{nr}(\mathbf{r},\hat{t}_f(\mathbf{r},\mathbf{r}_s))]\ , \tag{2.26}$$

where $\mathbf{n}_l$ is the tangential unit vector along $l(\mathbf{r}_s,\mathbf{r})$ at $\mathbf{r}$.

F. RECONSTRUCTION ALGORITHM IN TAT

In TAT, the to-be-reconstructed parameter is the energy deposition, because the acoustic contrast is usually much less significant than the electromagnetic absorption contrast. We will be showing that the energy deposition is equivalent to the initial pressure distribution in TAT.

1. A Delta Excitation Pulse

The thermoacoustic signal is related to the energy deposition by

$$\nabla^2 p(\mathbf{r},t) - \frac{1}{v_s^2}\frac{\partial p(\mathbf{r},t)}{\partial t^2} = \frac{\gamma(\mathbf{r})}{v_s^2}\frac{\partial p(\mathbf{r},t)}{\partial t^2} - \frac{\beta}{C}\frac{\partial H(\mathbf{r},t)}{\partial t}\ . \tag{2.27}$$

We will first consider a delta pulse, and the effect of finite pulse length will be discussed later in the paper. Substituting a delta pulse into (2.27), and applying integration of t over $[0-,0+]$ twice, where 0+ (0-) is an infinite small positive (negative) real, we have

$$p(\mathbf{r}, 0+) = \varepsilon\varphi(\mathbf{r}), \tag{2.28}$$

where $\varepsilon = \beta v_s^2 I_0/C$, and it is assumed that the thermoacoustic pressure is finite. Therefore, the reconstruction algorithm in TAT is equivalent to reverting the pressure field to time zero. This concept can also be adopted to derive TAT reconstruction algorithm in a known acoustically heterogeneity medium. Therefore, combining (2.28) and the time reversal techniques, we have the following exact reconstruction algorithm in TAT,

$$\varphi(\mathbf{r}) = \frac{1}{\varepsilon}p_i(\mathbf{r}, 0) = \frac{1}{\varepsilon}p_r(\mathbf{r}, 2T_0). \tag{2.29}$$

2. The Effect of Finite Bandwidth in an Acoustically Homogeneous Model

In many cases, $\bar{p}(\mathbf{r}, k)$ may be modified from the signal in the ideal case by the multiplication of a function of k in the k-space due to the limited bandwidth of the detector. The time-reversed field is

$$\bar{p}_r(\mathbf{r}, k) = i\varepsilon k\bar{\eta}(-k)\exp(-2ikT_0)\iiint \varphi(\mathbf{r}')[G_k(\mathbf{r} \mid \mathbf{r}') - G_k^*(\mathbf{r} \mid \mathbf{r}')]d\mathbf{r}'. \tag{2.30}$$

The reconstructed image is equivalent to the time-reversed field at $2T_0$

$$\varphi_m(\mathbf{r}) = \frac{1}{2\pi\varepsilon}\int dk \exp(2ikT_0)\bar{p}_r(\mathbf{r}, k) = \frac{1}{2\pi\varepsilon}\int dk\bar{\eta}(-k)[\bar{p}_i(\mathbf{r}, k) + \bar{p}_i(\mathbf{r}, -k)]. \tag{2.31}$$

Now, we will compute the point spread function. If there is a point source at $\mathbf{r}_0$, the thermoacoustic signal caused by it is

$$\bar{p}_i(\mathbf{r}, k) = ik\varepsilon G_k(\mathbf{r} \mid \mathbf{r}_0)\ . \tag{2.32}$$

Substituting (2.32) into (2.31), we have the following expression for the point-spread-function (PSF)

$$\begin{aligned}\varphi_{psf}(\mathbf{r},\mathbf{r}_0) &= \frac{1}{2\pi}\int\limits_{-\infty}^{\infty} dkik\eta(-k)\frac{[\exp(-ik\left|\mathbf{r}-\mathbf{r}_0\right|)-\exp(ik\left|\mathbf{r}-\mathbf{r}_0\right|)]}{4\pi\left|\mathbf{r}-\mathbf{r}_0\right|} \\ &= (\frac{1}{2\pi})^2\int\limits_{-\infty}^{\infty} dk(-1)k\eta(-k)\frac{\sin(-ik\left|\mathbf{r}-\mathbf{r}_0\right|)}{\left|\mathbf{r}-\mathbf{r}_0\right|} \\ &= \frac{\eta'(-\left|\mathbf{r}-\mathbf{r}_0\right|/v_s)-\eta'(\left|\mathbf{r}-\mathbf{r}_0\right|/v_s)}{4\pi\left|\mathbf{r}-\mathbf{r}_0\right|}\ . \qquad (2.33)\end{aligned}$$

This is in agreement with the PSF in TAT obtained for planar, cylindrical and spherical configuration [43]. An interesting conclusion from (2.33) is that the component of the excitation pulse that is antisymmetrical with respect to time zero does not contribute to the reconstructed image.

FBA is used in our discussion about DT. We realize that FBA does not hold for high frequencies. However, if we confine the frequency response range of the ultrasound transducer to the low-frequency range, FBA will stand approximately. Alternatively, we can improve FBA by using distorted-wave Born approximation. At last, it should be pointed out that our time-reversal methods can be easily applied to inverse diffraction and inverse source problems.

CHAPTER III

LIMITED-VIEW THERMOACOUSTIC TOMOGRAPHY[1]

A. INTRODUCTION

As shown by (1.7), TAT signals can be represented in terms of a known circular Radon transform. There exist explicit reconstruction formulas for this transform [44, 45, 46, 47, 48, 49] when data are collected along a line or a full circle in a two-dimensional (2-D) case and along a plane, sphere, or a cylinder in a three-dimensional (3-D) case. In all these cases it is assumed that the imaged objects are located either on one side of the scanning line (plane), or inside the scanning circle (sphere, cylinder), without which assumption reconstruction is not always possible. The available inversion formulas employ either special-function expansions, or backprojection in the case of the linear or planar data-acquisition geometry.

Exact reconstruction algorithms for TAT based on series-expansion techniques are implemented in planar, spherical, and cylindrical configurations in [24, 25, 50]. Following the line of [39], an approximate modified backprojection algorithm has been developed from an exact 3-D model. Other backprojection algorithms are also proposed [12, 51]. In these algorithms for TAT, it is assumed that the thermoacoustic signals are detected in a full (panoramic) view. In other words, the detector moves along a whole circle in the 2-D case or sphere in the 3-D case. This means in particular that each point of the scanned object is visible from the detector's trajectory for 2π radians in the 2-D case or 4π steradians in the 3-D case. However, in many applications of TAT, the signals cannot be collected from all directions. For example,

---

[1] ©2003 American Association of Physicists in Medicine. Reprinted, with permission from Y. Xu and L.-H. Wang, "Reconstructions in limited-view thermoacoustic tomography," accepted by *Med. Phys.*, 2003.

the solid angle of detection is at most 2π steradians for a breast. So, one faces here an incomplete data problem. Although one can show [52] that theoretically an arbitrarily small scanning arc (i.e., the arc of a circle over which the detectors move) suffices for the uniqueness of recovery, in practical implementations the limited-view problems usually lead to losing some parts of the high-frequency information and hence blurring of some sharp details.

In this chapter, we present our results on the limited-view TAT. Although limited-view problems have been studied extensively in X-ray tomography (e.g., [53], and references therein), diffraction tomography [54], and reflectivity tomography [55], to the best of our knowledge, no results on the limited-view TAT have been published. In the methods section, a formula for the forward problem is presented. In particular, it is shown that the TAT signals can be represented in terms of a known circular Radon transform. This enables us to employ results of [52] that justify the theoretical possibility of reconstruction. Then results by Quinto and Louis [56] developed for sonar are applied to determine the "stably visible" parts of the objects in TAT. In particular, a piece of the boundary of an object (i.e., interfaces between objects) can be stably reconstructed as soon as at any point on the boundary at least one of its two normal directions passes through a detector position. On an intuitive level, this is because an arbitrary interface can be considered as a combination of small flat interface segments, and each segment transmits acoustic waves identically in the two opposite directions perpendicular to the interface segment. This means that we need to collect signals at only one of the two directions to obtain information about the boundary segment. More complicated sharp details ("singularities") could be considered as well, which would entail using the notion of a wavefront of a function and other tools of microlocal analysis. However, among all possible singularities, tissue interfaces are of the most interest for TAT.

Exact reconstruction formulas for the limited-view TAT are not yet known. We derive an approximate filtered backprojection (FBP) algorithm that works well quantitatively. A version of this method that emphasizes singularities [a "local tomography" (LT) reconstruction] is also tested. The FBP results are then iteratively improved using a truncated conjugated gradient (TCG) method. Besides using numerical phantoms for calculations, we also conducted experimental measurements on physical phantoms and applied our reconstruction methods to the obtained data. The results of all these reconstructions confirm our theoretical predictions. These are addressed in the section of results and discussion.

1. Analysis of Singularities in Circular Radon Transform and Limited-view TAT

a. Circular Radon Transform

It can be seen from (1.7) that $p_1(\mathbf{r}, t)$ can be obtained from $\varphi(\mathbf{r}')$ after applying three linear operations: circular (spherical in 3-D) Radon transform **R,** multiplication by $1/t$, and differentiation $\mathbf{D}_t$ with respect to t. The circular Radon transform defined as

$$\mathbf{R}\varphi(\mathbf{r}, t) = \oint\limits_{t=|\mathbf{r}-\mathbf{r}'|/\nu_s} \varphi(\mathbf{r}')d\mathbf{r}' \ . \tag{3.1}$$

It is similar to the conventional linear Radon transform, except that the integration here is over a circle or a sphere rather than a line or a plane. In this chapter, the set Σ of centers $\mathbf{r}$ of the circles (spheres) of integration coincides with the set of positions of the detector, and the set of radii (that are proportional to time t) is unrestricted. We call these circles (spheres) "projection curves" ("projection surfaces") and the set Σ the "scanning curve" (or "detector curve"). We assume that the source function $\varphi(\mathbf{r})$ is zero outside Σ and in a neighborhood of Σ. In other words, the scanned object is strictly inside the scanning detector trajectory Σ. In this case it is known that data collected from an arbitrarily small arc of the detector trajectory are theoretically sufficient for a complete reconstruction [52]. This result, however, neither provides reconstruction algorithms, nor guarantees that the reconstruction can be achieved in any practically stable manner. Indeed, it is well known [49] that solving incomplete data problems usually leads to operations like Fourier filtrations with fast growing filters, which implies high sensitivity to errors in data. This in turn requires cutting high frequencies and hence blurring the images. Sacrifices in high frequencies naturally lead to destroying sharp details (interfaces between different tissues) in the reconstruction. The question of what parts of the singularities (i.e., sharp details) of the image can be stably reconstructed depending on the scanning geometry is addressed for the planar Radon transform in [57] and for the circular one in connection with sonar in [56]. Local tomography reconstructions [58, 59, 60, 61] also address similar issues.

b. TAT

We would like to note that in (3.1) the presence of a temporal derivative in the TAT data (which is equivalent to a radial derivative after the circular Radon transform) can only emphasize singularities and hence should not lead to additional blurring in comparison with the circular Radon transform itself (this can be shown rigorously). In fact, as it will be seen later in this chapter, this derivative is a natural part of the reconstruction procedure for the circular Radon transform.

We will now apply to TAT the known results of integral geometry concerning singularity reconstruction [56, 57]. The exact description would require the notions of microlocal analysis, in particular the one of a wavefront set of a function (e.g., [56, 57]). However, in tomographic problems, in particular in TAT, one is mostly interested in only one type of singularity: the jump of the imaged value φ across

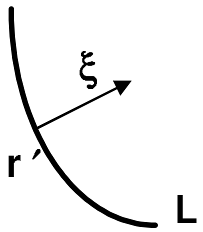

Fig. 3. Wavefront $WS(\varphi)$ of an image φ consisting of pairs $(\mathbf{r}', \xi)$. Point $\mathbf{r}'$ belongs to $\mathbf{L}$ (a jump interface in the image) and ξ is a non-zero vector normal to $\mathbf{L}$ at $\mathbf{r}'$.

an interface (a curve in 2-D or a surface in 3-D). Assuming that φ is smooth except for a jump across a curve $\mathbf{L}$ in the plane (the 3-D situation is analogous with $\mathbf{L}$ being a surface), then the wavefront $WS(\varphi)$ of φ consists of pairs $(\mathbf{r}', \xi)$ where point $\mathbf{r}'$ belongs to $\mathbf{L}$ and ξ is a non-zero vector normal to $\mathbf{L}$ at $\mathbf{r}'$ as shown in Fig. 3. Now the results of [56] can be summarized as follows: one can identify that a pair $(\mathbf{r}', \xi)$ belongs to the wavefront set of the image by looking at the singularities of the Radon data if and only if among the circles (spheres) of integration ("projection curves") there exists at least one passing through the point $\mathbf{r}'$ and normal to ξ at this point. To put it differently, in TAT one can see without blurring only those parts of the interfaces that one can touch tangentially by circles (spheres) centered at detector positions. This means that one needs to have a detector located on the normal to $\mathbf{L}$ at $\mathbf{r}'$ in either direction. What happens to other, "invisible" parts of the interfaces? We provide here a non-technical explanation. One would need to recover these singularities from smooth parts of the measured data. This in turn means the involvement of operations like filtrations in the frequency domains with filters growing faster than any power. In order to avoid instabilities then, this clearly requires cutting those frequencies off, which causes blurring. The conclusion is that the "visible" parts of the interfaces should be possible to recover, while the others should blur independently of the reconstruction method used. Discussion of the

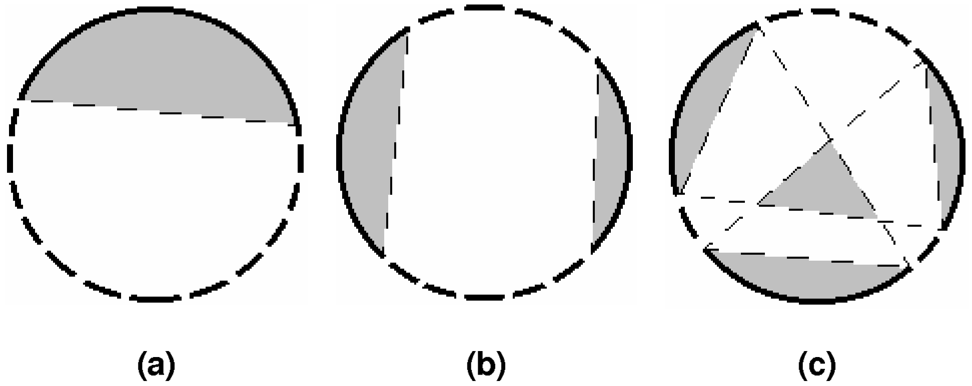

Fig. 4. Illustration of the “detection regions” (shaded areas) of circular Radon transform. (a) The detector moves along a single arc (solid) of a circle. (b) Two arcs. (c) Three arcs.

related issues of stability of reconstruction would be too lengthy; one can find the relevant considerations for instance in [62]. In a nutshell, more stable tomographic problems allow one to estimate the error in the reconstruction (in a Sobolev norm) by the error in the data in a somewhat smoother norm. This, however, is impossible when the information about the wavefront is lost.

Let us make this geometry more explicit for our circular (spherical) trajectory of detectors. We pose the question: Assume that only a part of the detector circle (sphere) is used for collecting data; at what locations then, all interfaces in the image will be completely recoverable? We will call the set of all such “good” locations the “detection region.” For images outside this region, one needs to apply the tangent-circle test as described in the preceding two paragraphs to predict what parts of the boundaries will not be stably recoverable. Assuming first that the detector moves along a single arc of the circle [Fig. 4(a)], then simple geometric consideration shows that the “detection region” is just the convex hull of this arc (i.e., the circular cap based on the arc). Here the “detection region” is shaded, and the arc of the circle where we do not position a detector is shown as a dotted line. Analogously, one can find the “detection region” (shaded) for two arcs [Fig. 4(b)]. The situation changes, however, for more complicated scanning trajectories. For instance, in the case of three arcs, one can have more than just circular caps in the “detection region” [Fig. 4(c)]. Here an additional triangular part of “detection region” appears in the center. The situation can become even more complicated for spherical 3-D geometry. The general rule for finding the “detection region” is: draw all lines such that both of their intersection points with the scanning circle (sphere) do not coincide with detector locations. These lines cover the “invisible” domain, so its complement forms the “detection region”. Note that in the “invisible” domain some boundaries can still be recovered stably, while others blur away. Namely, the parts of the boundaries the normal lines to which pass through a detector position, and only those, can be stably recoverable. The above conclusions are illustrated in Fig. 5, where the “invisible” parts of the object boundaries, i.e. the ones to be blurred during the reconstructions, are shown with dotted lines. For instance, in Fig. 5(a) one has a cap “detection region” and a rectangular object that does not fit fully into it. Then one expects the dotted parts of the rectangle’s boundary to be affected by blurring artifacts during the reconstruction. Fig. 5(b) shows the expected reconstruction of a circular object located outside the “detection region”. Let us remark that similar considerations apply to an arbitrary scanning geometry. For instance, Fig. 5(c) shows the parts (solid) of the boundaries of a circular and a square object that can be stably reconstructed from the detection on a segment AB.

c. Reconstruction Methods

As it has already been mentioned before, exact inversion procedures are known for circular and spherical Radon transforms in some special detection configurations [44, 49]. However, for the circular trajectories of detectors only special-function-expansion

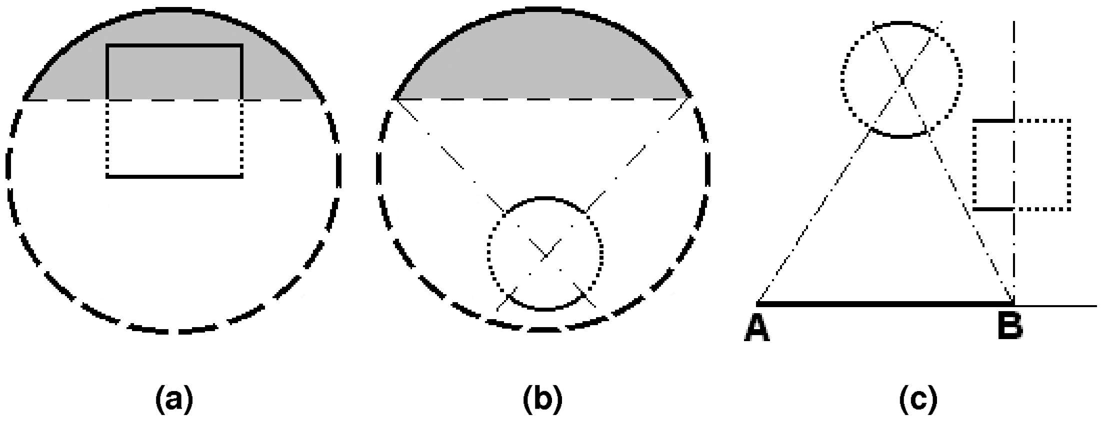

Fig. 5. ”Visible” (solid line) and “invisible” (dashed) boundaries of a square object, and the ”detection regions” (shaded areas). (a) The detector moves along an arc (solid). (b) Same as (a) for a disk phantom. (c) Same as (a) except that the detector moves along the line segment AB and the objects are a square and a disk. The ”visible” boundaries are expected to be recoverable stably, while the ”invisible” boundaries should be blurred away.

methods are known, while formulas of FBP type are available for the linear (planar) trajectories. Our approach is to use an approximate FBP formula, which happens to work well under most of circumstances and can be improved in conjunction with post-processing by an iterative method. Namely, for objects not too close to the detectors, one can think of projection lines as close to straight lines, and hence the circular Radon transform as being close to the standard Radon transform. In this approach, the center $\mathbf{r}$ of the projection circle and its radius ρ (which is proportional to time) are analogs of the normal coordinates $(\hat{\theta}, \varsigma)$ of a line $\mathbf{r} \cdot \hat{\theta} = \varsigma$ in the standard Radon transform where, $\hat{\theta}$ is a unit vector normal to the line. FBP inversion of the standard Radon transform on the plane consists (up to a constant factor) in applying the first derivative with respect to ς, then Hilbert transform with respect to ς, and finally the backprojection operator, which averages over lines passing through a given point [49]. We implement a similar procedure in the circular Radon transform. This amounts

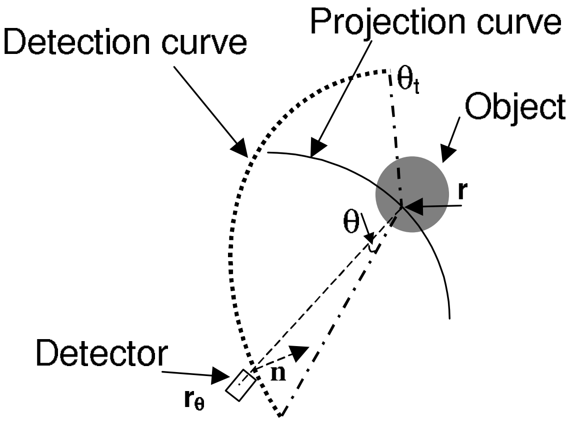

Fig. 6. Diagram to show the uniform rotation of θ in FBP in circular Radon transform or TAT. The dashed arrow represents the normal to the detection curve (dotted arc) at $\mathbf{r}_\theta$ and the dashed line is the normal to a projection arc centered at $\mathbf{r}_\theta$ and passing through a reconstructed point $\mathbf{r}$. θ_t is the detection view at $\mathbf{r}$, i.e. the angle subtended by the detection curve as viewed from $\mathbf{r}$.

to a differentiation with respect to the radius, a Hilbert transform with respect to the radius, and then a circular backprojection, i.e., averaging over the circles passing through a given point. One should also make sure that during the backprojection the tangent lines (or the normal vectors) to the projection curves at the given point, for example, θ in Fig. 6, rather than the centers of the projection curves (which coincide with detector positions), rotate at a constant speed. Differentiation with respect to the radius is already contained in the TAT data, as shown in (3.1), so this step can be simplified in 2-D reconstructions (it is still required in a 3-D TAT). Based on this, we arrive in Appendix B at an approximate FBP reconstruction formula for the 2-D TAT

$$\varphi(\mathbf{r}) \approx \frac{C}{\beta I_0 v_s^2} \oint ds \frac{\mathbf{n}\cdot(\mathbf{r}-\mathbf{r}_\theta)}{\left|\mathbf{r}-\mathbf{r}_\theta\right|^2} \mathbf{H}(p_1(\mathbf{r}_\theta, \left|\mathbf{r}_\theta-\mathbf{r}\right|/v_s)\left|\mathbf{r}-\mathbf{r}_\theta\right| + p_2(\mathbf{r}_\theta, \left|\mathbf{r}_\theta-\mathbf{r}\right|/v_s)), \tag{3.2}$$

where $\mathbf{H}$ is a Hilbert transform; $p_2(\mathbf{r},t) = v_s \int_0^t p_1(\mathbf{r},t)dt$; $\mathbf{n}$ is the inward normal to the detection curve at $\mathbf{r}_\theta$; ds is the arc length differential; and the integration is along a complete detection curve (i.e., the one that runs around the objects). In the case of incomplete data, one just replaces the missing data with zeros (possibly gradually phasing off the existing data closely to the missing data region to reduce the artifacts caused by the missing data) and then applies the formula. Although this is not an exact inversion, one can show using microlocal analysis that it preserves all "visible" singularities (a conclusion supported by the numerical and experimental evidences presented below). If one is interested in singularities only (e.g., interfaces between different types of tissue), then one can drop the integral term $p_2(\mathbf{r}_\theta, |\mathbf{r}_\theta - \mathbf{r}|/v_s)$ in the last formula, since it corresponds to a pseudo-differential operator of a smaller order.

Let us also provide a local tomography formula for the 2-D TAT. In order to do this we replace the Hilbert transform by an additional time derivative. This then leads to the local tomography reconstruction:

$$\Lambda\varphi(\mathbf{r}) = \frac{C}{\beta I_0 v_s^2} \oint ds \frac{\mathbf{n}\cdot(\mathbf{r}-\mathbf{r}_\theta)}{|\mathbf{r}-\mathbf{r}_\theta|^2} \left(\frac{\partial p_1}{\partial t}(\mathbf{r}_\theta, |\mathbf{r}_\theta - \mathbf{r}|/v_s)\,|\mathbf{r}-\mathbf{r}_\theta| + 2v_s\, p_1(\mathbf{r}_\theta, |\mathbf{r}_\theta - \mathbf{r}|/v_s)\right). \tag{3.3}$$

As before, if one wants to recover singularities only, the term of a lower pseudo-differential order $2v_s p_1$ in this formula can be dropped.

One can apply a similar consideration to the 3-D TAT, which leads to the approximate FBP formula:

$$\varphi(\mathbf{r}) \approx -\frac{C}{2\pi\beta I_0 v_s^3} \oint dS \frac{\mathbf{n}\cdot(\mathbf{r}-\mathbf{r}_\theta)}{|\mathbf{r}-\mathbf{r}_\theta|^2} \left(\frac{\partial p_1(\mathbf{r}_\theta, |\mathbf{r}_\theta - \mathbf{r}|/v_s)}{\partial t} + \frac{2p_1(\mathbf{r}_\theta, |\mathbf{r}_\theta - \mathbf{r}|/v_s)v_s}{|\mathbf{r}_\theta - \mathbf{r}|}\right). \tag{3.4}$$

In the case of limited-angle detection, there is also the following possibly useful correction if one is interested in quantitative imaging. Here, we define a detection view θ_t (solid angle Ω_t for 3-D case) at $\mathbf{r}$, which is the (solid) angle subtended by the detection curve (surface) when viewed from the reconstruction point $\mathbf{r}$ as shown in Fig.

6. Because of the incompleteness of data, the integral in the above equations runs over a portion of the detection curve (surface) only. One might want to compensate for that by multiplying the value of the reconstructed function at this point by a factor $2\pi/\theta_t$ ($4\pi/\Omega_t$ for the 3-D case). The factor appears when the backprojection operator is considered approximately as an averaging over the available projection curves passing through the reconstruction point $\mathbf{r}$. It should be noted that both θ_t and Ω_t depend on $\mathbf{r}$. The effectiveness of this compensation is shown below by our numerical simulation results of TAT.

There are three useful features of (3.2) and (3.4). First of all, they yield, as we intend to show in numerical simulations, acceptable quantitative results from limited-view data. Secondly, their computation complexity is much less than that for the iterative methods such as TCG, while they produce images of comparable quality. Finally, if an iterative method is necessary, our backprojection formula can serve as a good initial guess. This is also observed in our numerical simulations.

Although the above backprojection formula is shown to work well in numerical simulations, it is not exact. Nevertheless, one can show that it amounts to applying a pseudo-differential operator to the image φ (this is true if the data is gradually phased out near the areas of the missing data). Pseudo-differential operators are known not to shift locations of any singularities, including boundaries (see analogous considerations, e.g., in [52, 61, 63]). This means that although the backprojection formula might give imprecise values of φ it will present the locations of the boundaries of all inclusions correctly.

Another reconstruction method is to apply an additional differentiation with respect to time (the radius) without applying Hilbert transform, as shown in (3.3). This leads to a local tomography type formula [58, 61]. The result of the procedure also produces an expression of the form $\Lambda\varphi$ where Λ is a pseudo-differential operator defined in (3.3). In this case, however, the operator has a positive order, which means that all the “visible” interfaces and other sharp details not only have correct locations, but also are emphasized. This effect is well known in image processing, where for instance the Laplace operator is sometimes used to emphasize the edges. One can also notice that our experimental data, due to the shape of the transducer’s impulse response function and electromagnetic pulse shape, already carry a filtration that makes the reconstruction similar to the local one. Then, unless an appropriate deconvolution is applied to the data during pre-processing, the interfaces are accentuated in the reconstruction. The reader will notice this in our actual reconstructions from experimental data.

2. Numerical Implementation

In the case of incomplete data discussed above, we complete it by concatenating with zeros (sometimes gradually smoothing the data to zero at the boundary in order to reduce the artifacts in the reconstruction). The FBP algorithm described above is first applied to the limited-view data. Since the inversion formula we use is not exact even for complete data, we improve it by employing an iterative algebraic method for solving the discretized version of (3.1), starting with the FBP reconstruction as the initial guess. We adopt as such the TCG method for finding the least-squares solution of the discretized version of the problem. No preconditioner is used. We also employ local tomography procedure described above. We expect in all these methods to see the reconstructions that agree with the theoretical predictions stated in the previous section, i.e., sharp “visible” details with the “invisible” parts blurred.

B. RESULTS AND DISCUSSION

Our results consist of three parts: (1) inversion of simulated circular Radon transform data to show the theoretical predictions about the “visible” and “invisible” boundaries, (2) reconstructions from simulated TAT data to test our reconstruction algorithms quantitatively, and (3) images based on experimental data collected from a physical phantom.

1. Numerical Results for the Limited-view Circular Radon Transform

Fig. 7 shows the inversion of the circular Radon transform for different detection configurations and phantoms (shown in the first column from the left) to demonstrate our discussions on the “visible” and “invisible” boundaries. In the second column from the left, the detection curve is shown as the solid part of the outer circle, the “detection region” is shaded, and the “visible” (solid) and “invisible” (dashed) boundaries of the objects predicted by theory are shown. The inclusion represents the object to be imaged. The third and fourth columns from the left show the FBP reconstructions and the local tomography reconstructions, respectively. Notice the good agreement between the three columns on the right concerning reconstructions of the “visible” and “invisible” parts of the boundaries.

Fig. 7(1a-1d) shows the results for a phantom containing a square inclusion. The data are collected from detectors located on the upper half-circle. Exactly the parts of the boundary of the square predicted in this chapter (see the dotted lines in the Fig. 7(1b)) become blurred in Fig. 7(1c) and Fig. 7(1d).

Fig. 7(2a-2d) and Fig. 7(3a-3d) show the reconstructions of circular inclusions from the data collected by the detector located along the upper half-circle. In Fig. 7(2a-2d), the phantom is completely outside the “detection region”, which leads to

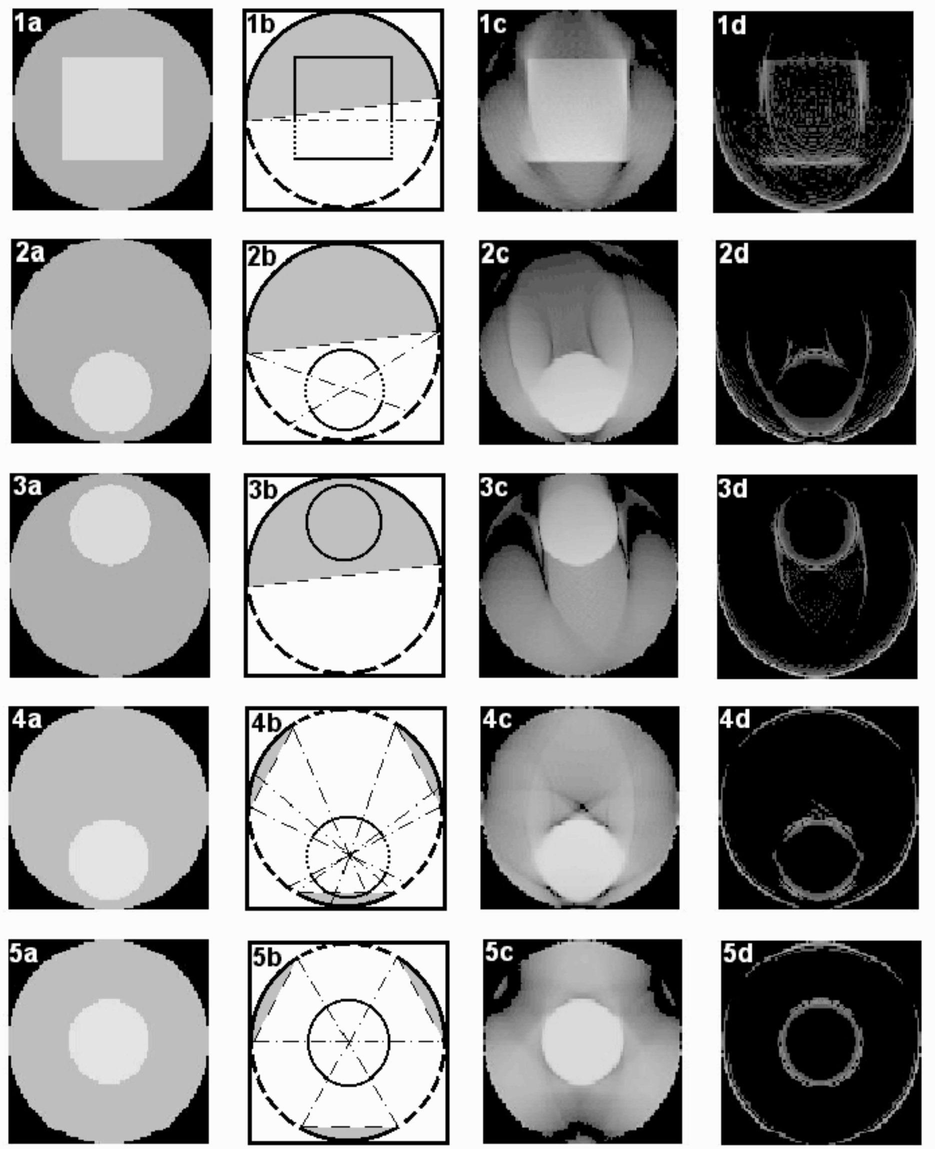

Fig. 7. Numerical simulation of circular Radon transforms. (1a) A square phantom inside a circular detection curve in a circular Radon transform. (1b) The diagram showing the detection curve (solid part of the outer circle), the "visible" (solid) and "invisible" (dashed) boundaries of the object predicted by theory, and the "detection region" (shaded). (1c) FBP reconstruction. (1d) Local tomography reconstruction, where the boundary is emphasized. (2a-2d) A disk phantom outside the "detection region". (3a-3d) A disk phantom inside the "detection region". (4a-4d) An off-center disk phantom and a detection curve consisting of three arcs. (5a-5d) A centered disk phantom and a detection curve consisting of three arcs.

blurring of its right and left boundaries in accordance with the theory. In Fig. 7(3a-3d), however, the boundaries of the disk are recovered sharply, since the inclusion is in the “detection region”. Notice here some deterioration of the image near the detector circle. This can be attributed to the fact that near the detector circle, linear and circular Radon transform become noticeably different, and so the quality of our approximate formulas diminishes. This problem can be dealt with in two ways: one can make sure that the detectors do not approach the imaged objects too closely (this will be enforced in our further numerical simulations and experiments), or to improve the reconstruction quality by post-processing with an iterative algebraic reconstruction method.

Other limited-view reconstructions from the circular Radon data are shown in Fig. 7(4a-4d) and Fig. 7(5a-5d), where there are three arcs of detection, 60 degrees each, with 60 degrees intervals between them. An off-center and a centered circular inclusion are reconstructed in Fig. 7(4a $-$4d) and Fig. 7(5a-5d), respectively. The results agree well with the theory: some parts of the boundary of the off-center disk are blurred; namely, those where the normals do not pass through any detector positions. However, the in-center disk is reconstructed sharply, in spite of the fact that it does not fit into the “detection region”. The reason is that in this case every normal to the boundary of the inclusion passes through a detector.

2. Reconstruction from Simulated Limited-view TAT Data

A numerical phantom that contains four sharp and one soft inclusions is shown in Fig. 8. Among the sharp ones we have one large and two small squares and one disk. The object value, which represents the electromagnetic energy deposition, is set to be 0.5 within the largest square and unity within other sharp inclusions and zero elsewhere. Inside the “soft” circular inclusion, this value drops linearly with the radius from unity

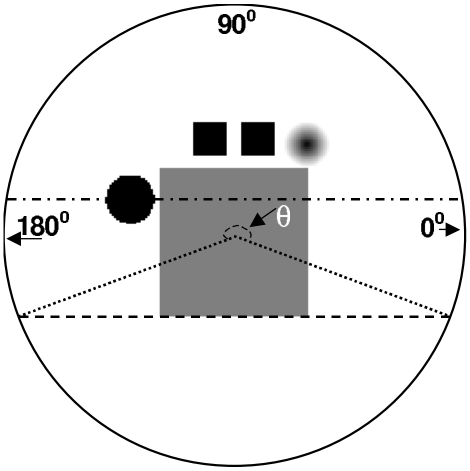

Fig. 8. Diagram of inclusions in TAT (used in Fig. 9). The value of the image $\varphi(\mathbf{r})$ is set to be 0.5 in the largest square and unity within other sharp inclusions and zero elsewhere. Inside the "soft" circular inclusion, this value drops linearly with the radius from unity at the center to zero at the interface.

at the center to zero at the interface in order to simulate a gradual interface. The imaged field of 154 mm by 154 mm is mapped with a 128 ×128 mesh. The detection circle has a radius of 133 mm and is centered at the center of the picture. We scan 200 steps in all the simulations. The gray scale and the scale bar of the images are shown below the images in Fig. 9. The top row of reconstructions employs the local tomography formula that emphasizes the boundaries. The next one uses the FBP formula, and the lowest one shows the improvements achieved by running the algebraic reconstruction method (TCG) starting with the FBP as an initial guess. The left column uses only the data collected from the $\pi/2$ detection arc in the first quadrant. None of the phantom inclusions fits into the "detection region". One can see that all parts of the inclusion boundaries the normals to which do not intersect the detector arc are blurred (even in the local tomography reconstruction). Other parts of the boundaries are sharp. This is in perfect agreement with our theoretical prediction. The soft inclusion is not significantly affected by the artifacts.

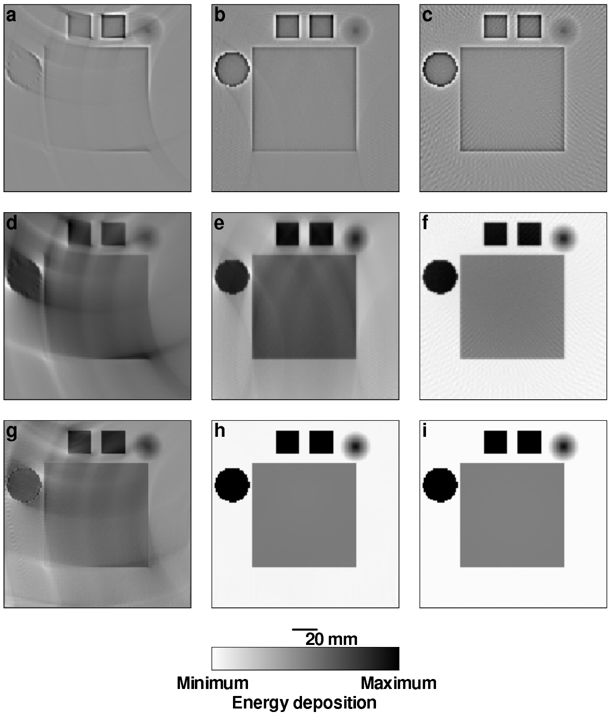

Fig. 9. Images reconstructed from simulated TAT data corresponding to the phantom in Fig. 8. The three columns correspond from the left to the right to detection angles of 90 degrees (from 0 ^{o} to 90 ^{o}), 217 degrees (from –19 ^{o} to 198 ^{o} as shown by the angle θ in Fig. 8), and 360 degrees respectively. The three rows correspond from top to bottom to the local tomographic reconstruction, FBP, and FBP with the consecutive TCG, respectively. The values of (minimum, maximum) of the gray scale for (a)–(i) are (–0.8081, 1.0000), (–0.8302, 1.0000), (–0.7515, 1.0000), (–2.0745, 1.7899), (–0.6385, 1.0723), (–0.1030, 1.0349), (–0.9284, 1.2859), (–0.0326, 1.0030), and (–0.0149, 1.0021) respectively. The maxima of the local reconstructions are normalized to unity.

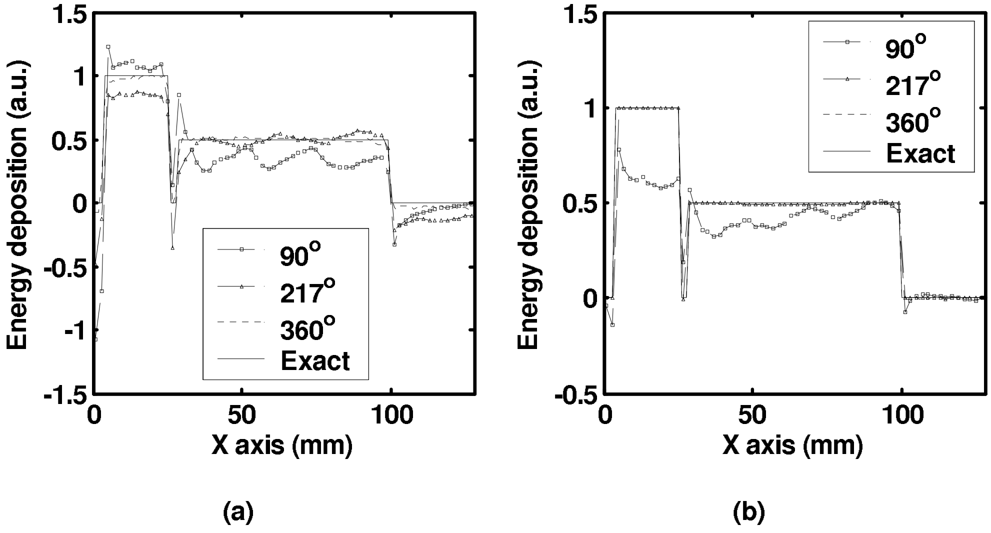

Fig. 10. Line graphs corresponding to the reconstructions in Fig. 9. (a) The graphs of FBP reconstructions shown in Fig. 9(d)–(f) and the corresponding exact value along the dashed-dotted line in Fig. 8. (b). The graphs corresponding to TCG reconstructions, Fig. 9(d)–(f), along the same line as in (a).

The middle column employs the data collected from the detector arc of approximately 217 degrees (the angle θ in Fig. 8), whose chord coincides with the bottom side of the large square inclusion. In this case all inclusions are in the "detection region", and hence all the boundaries are reconstructed sharply. The third column represents the full data reconstruction. Notice that the quality of the final reconstructions in the last two columns is the same. Figs. 8(a) and (b) show the reconstructed image $\varphi(\mathbf{r})$ along the dashed-dotted line in Fig. 8 using the FBP [Figs. 7(d)–(f)] and TCG reconstructions [Figs. 7(g)–(i)], respectively. The exact value is also shown for comparison. It can be found in Fig. 10 (a) that the results of FBP are in good agreement with the real value for the case of 217-degree and 360-degree detection, where all objects are in the "detection region". Iteration improves the results further as shown in Fig. 10(b). Even for the case of a 90-degree detection curve, the profile of the objects is reconstructed. Comparing (a) and (b), one can find that the significant overshoot

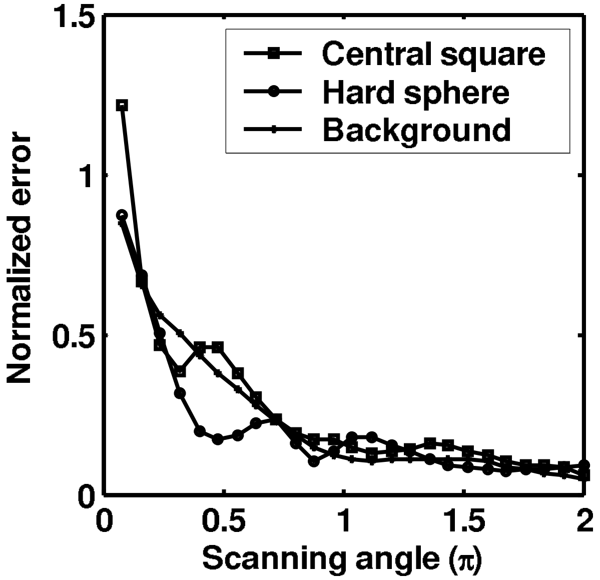

Fig. 11. Dependence of reconstruction on detection view. Dependence of the normalized errors on detection view of the mean value in the hard sphere(circle mark), the mean value in the central square(square mark), and the mean value in the background(*).

and undershoot in FBP can be considerably reduced by TCG iterations (we remind the reader that FBP is only an approximation rather than the implementation of an exact formula).

3. Dependence of Reconstruction on Detection View

Fig. 11 shows the normalized errors of reconstructions via the detection view. Three reconstruction values are studied: the mean value in the hard sphere, the mean value in the central square, and the mean value in the background. The errors of reconstruction are normalized to the corresponding real values for the hard sphere and the central square, and to the real value of the hard sphere in the case of the background(because its real value is zero). When the detection angle is less than π, the errors decrease sharply with the increasing detection angle; when the detection angle is larger

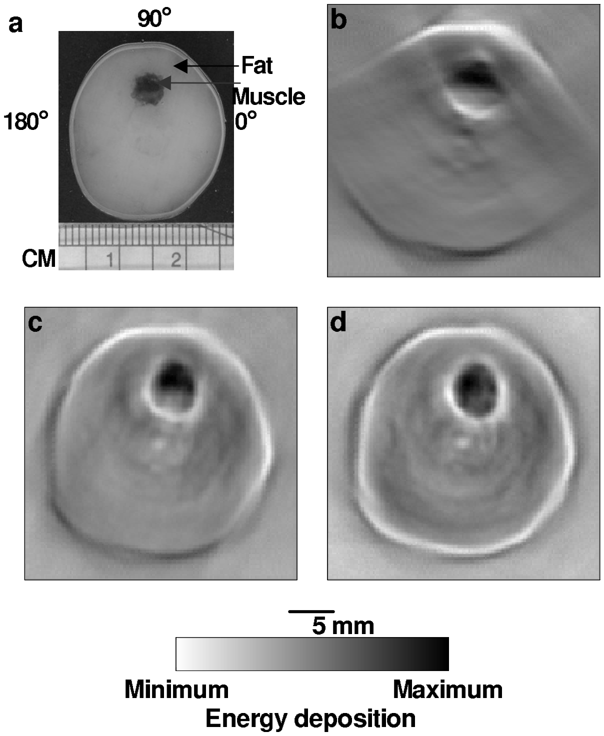

Fig. 12. Experimental results. (a) Photograph of the experimental sample. (b)–(d) TAT reconstructions using detection arcs of 92 degrees (from 50 ^{o} to 142 ^{o} in (a)), 202 degrees (from –18 ^{o} to 184 ^{o}), and 360 degrees, respectively. The blurred parts of the boundaries in (b) due to the limited view agree with the theoretical predictions. In (c) all the boundaries are resolved, since the object fits into the "detection region".

than π, the errors change much more slowly with the increasing detection angle. The results agree with our theoretical conclusions.

4. Experimental Results

The experimental setup is described in [19] and will not be repeated here. The sample and the polar coordinate system describing the scanning orbit are shown in Fig. 12(a). The sample consists of a muscle cylinder of 4 mm in diameter and 5 mm in length embedded in a chunk of pork fat of 1.2 cm in radius r_f. There is a 10-mm fat layer below the muscle and another 7-mm one above it. An electromagnetic pulse is delivered to the sample from below (i.e., from behind the picture plane). With a scanning radius of $r_d = 7.1$ cm, thermoacoustic data are collected around the sample over a $2\ \pi$ angular span with 161 steps. As it is mentioned above, the electromagnetic pulse profile and the impulse response function of the ultrasonic transducer impose a filter on the thermoacoustic signals. We attempted to correct this effect using deconvolution but found that the resulted images were distorted, due to the lack of precise knowledge of the filter. Therefore, we do not use deconvolution in the reconstruction. This leads, as is explained above, to somewhat emphasized interfaces.

Figs. 9(b)-(d) show the reconstructed images using FBP with three sets of data. In the first of them, we choose the data collected along a circular detector arc of 92 degrees located at the top of the picture and almost symmetric with respect to its vertical axes. One sees that the left and right boundaries of the muscle cylinder and of the pork chunk are blurred away, since their normal lines do not touch the detector arc, while the rest of the boundary is sharp. The next figure shows reconstruction obtained with the data collected from a 202-degree arc [which is about $180 + 2 * a\sin(r_f/r_d)$ obtained in the same way as θ in Fig. 8], when the whole phantom fits into the detection region. All boundaries are sharp now. Finally, the last figure shows the reconstruction with the full-view data.

Notice that although no local reconstruction algorithms are applied, the boundaries are somewhat emphasized. The reason for this is the presence in the data of the impulse response function of the ultrasonic transducer, which has an effect similar to the application of an additional derivative with respect to the radius of the circle of integration. Presence of such a derivative emphasizes high frequencies and makes the reconstruction similar to a version of a local tomography algorithm.

5. Discussion

As mentioned above, although circular scanning is used in both our numerical and experimental studies, our conclusions can be applied to other configurations as well. In TAT with a planar configuration [51, 64, 65], detections are implemented on a part of a line or a plane where the scanning view is quite limited; consequently, artifacts and interface blurring appear in the reconstructed images. In fact, in planar and linear scanning geometries one can never have an object immersed entirely into the "detection region" because the normal lines to any interfaces that are orthogonal to the detector plane (line) never pass through a detector. As a consequence, those parts of the interfaces will be blurred in any kind of reconstruction. For a sufficiently large view, these parts will be small, but theoretically will never disappear. For example, in [51] 2-D planar detection is utilized to image artificial blood vessels; the scanning view is about 2.18 steradians. Therefore, it is not surprising that only the interfaces more-or-less parallel to the plane of detection are well imaged. In [64], linear scanning detection is used to image a 2-D phantom. Because the view in [64] is much larger than in [51], the interfaces are recovered much more completely. However, due to a limited view, artifacts and interface blurring similar to those demonstrated in our numerical and experimental studies still appear in the images in [64].

By comparing Figs. 7 and 9, we observe that the quality of images reconstructed from incomplete data when an object is in the detection region, is comparable with those from the full-view data. Scanning a smaller range has the advantages of reducing the scanning time or the size of the acoustic transducer array. It should be pointed out that this advantage usually exists in the case when both the sample and medium are relatively acoustically homogeneous. When strong wavefront distortion caused by acoustic heterogeneities occurs, it might be beneficial to collect signal from all directions.

CHAPTER IV

EFFECT OF ACOUSTIC HETEROGENEITY ON BREAST THERMOACOUSTIC TOMOGRAPHY[1]

A. INTRODUCTION

An important assumption in the previous reconstruction algorithms is that the tissue is acoustically homogeneous. For many medical imaging applications, including imaging of the female breast, this assumption is an approximation. For example, the speed of sound in the breast can vary from 1400 m/s to 1550 m/s. Errors due to the assumption of a constant acoustic speed, which has never been studied in TAT, can potentially have a pronounced effect on image quality. In breast ultrasound tomography (UT), however, wavefront distortion has been studied extensively [66, 67, 68, 69]. The amplitude distortion caused by refraction dominates the phase distortion induced by acoustic speed variation in the breast UT [67]. Refraction occurs where there is a speed mismatch across a tissue interface. Because of refraction, rays from a single source can reach the same receiver by different paths, as shown in Fig. 13. The interference between these rays causes strong amplitude distortions in breast UT. Different deaberration methods have been proposed to compensate for phase distortion in UT [70, 71]. However, they have so far been inadequate to correct the strong amplitude distortion caused by refraction [72]. The effects of acoustic heterogeneity on breast TAT are estimated to be weaker than those in breast UT for the following reasons. First, signals in breast TAT are primarily in a lower frequency range (usually below 1.5 MHz [13]) than those in UT. Ultrasound scattering in this frequency range is

---

[1] ©2003 IEEE. Reprinted, with permission from Y. Xu and L.-H. Wang, "Effects of acoustic heterogeneity in breast thermoacoustic tomography," *IEEE Trans. Ultrason. Ferroelectr. Freq. Control*, vol. 50, pp. 1134–1146, 2003.

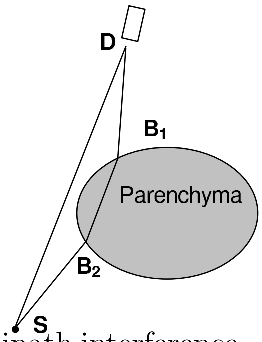

Fig. 13. Illustration of the multipath interference. An interference caused by refraction at boundary points B_1 and B_2 in breast ultrasound imaging in transmission mode. S is a point source and D is a detector.

weak. Secondly, in TAT, the acoustic source is induced by electromagnetic absorption; therefore, only one-way distortion on reception wave propagation occurs. As shown in Fig. 14, an acoustic ray, for example SB_1D, needs to pass through interface Σ only once. In contrast, in pure ultrasound imaging, either in the pulse-echo mode or in the transmission mode, ultrasound distortion includes two parts: distortion during both transmission and reception wave propagation. Therefore, the acoustic wave has to pass through the interface at least twice, as shown in SB_2B_1D in Fig. 14. Third, if the detection distance from the objects are properly chosen, the effects of amplitude distortion can be minimized in breast TAT, as will be shown in Section B.

In our work, we analyze the effects of amplitude distortion and numerically simulate the effects of phase distortion with the truncated conjugate gradient [73] (TCG) method. In Section B, we investigate the effects of refraction on the wavefront amplitude and phase in breast TAT. We prove that, in breast TAT, a convex parenchyma wall (when observed from the outside of the parenchyma tissue) does not cause multipath interference and that the effects of amplitude distortion are also not severe for a concave boundary. An equation for the forward problem in an acoustically heterogeneous model is also introduced at the end of this section. The inversion algorithm of TCG, and the model and parameters used in the numerical simulations, are presented

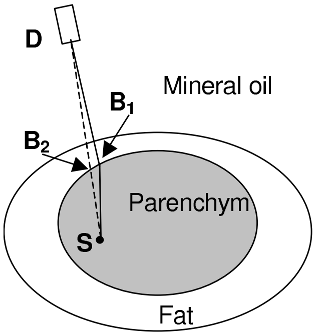

Fig. 14. Illustration of a ray refraction at the parenchyma wall in breast TAT. The outer oval represents the breast surface, where there is negligible refraction due to the good match of acoustic speed between fat and mineral oil. The solid line SB_1D represents a ray in the heterogeneous model while the dashed one SB_2D in a homogeneous model. S is a point source and D is a detector; B_1, B_2 are two points at the parenchyma wall.

in Section C. In Section D, the effects of phase distortion are studied numerically. We show how the degradation of the reconstructed images depends on acoustic heterogeneity when acoustic heterogeneity is not considered in the reconstruction algorithm. Correction of phase distortion should be the first step for improving image quality in breast TAT because phase is much more important in imaging than amplitude when there is no severe amplitude distortion [74, 75]. Therefore, the reconstructions are implemented with consideration of acoustic velocity heterogeneity to illustrate how the imaging degradation can be compensated for. The effects of the errors in the acoustical velocities on this compensation are also investigated. In Section E, an approach to implement compensation with only TAT data is proposed. The differences between breast TAT and breast ultrasound imaging on the effects of acoustic heterogeneity and speckles are explained by their differences in central ultrasound frequency and detection geometry. The last section presents conclusions.

B. THE EFFECT OF ACOUSTIC HETEROGENEITY IN TAT

A TAT model is shown in Fig. 14. In our imaging system, mineral oil is chosen as the coupling medium for both microwaves and ultrasonic waves. The acoustic speed of light in mineral oil is 1437 m/s [76], which is very close to that in fat [77]. Therefore, there should be negligible refraction at the boundary between the breast and the mineral oil, and, consequently, we will consider only the effects of the acoustical heterogeneity within the breast. More details on our TAT experimental setup can be found in [19].

1. Amplitude Distortion Caused by Refraction

Fig. 13 shows the multipath interference in breast ultrasound imaging in transmission mode. The acoustic ray from source S can travel to detector D by two different paths, SD and SB_2B_1D, due to refraction at the interfaces between different tissues. The interference between the two rays can cause amplitude distortion [67]. In the following subsections, we will first prove that there is no multipath interference in the case of a convex parenchyma wall in breast TAT. Then, we will show that the amplitude distortion is also not severe for a concave parenchyma wall.

a. Convex Boundary

In this subsection, we will show that there is no multipath interference in the TAT of the breast with a convex parenchyma wall by proving that no two rays from a source within the parenchyma will intersect with each other after refractions at the wall. The model is shown in Fig. 15, where S is an acoustic source; v_p and v_{s0} are the acoustic speed in the breast parenchyma and the medium (also the fat), respectively ($v_p > v_{s0}$); the dashed lines are the normals of the boundary points B_1, B_2, B_3,

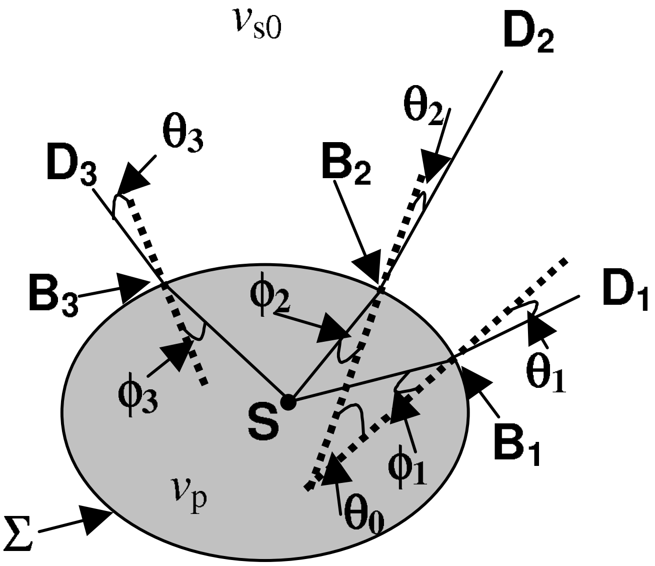

Fig. 15. Diagram to study refraction at a convex boundary. It shows that no two rays from a point source S will intersect with each other after being refracted at a convex boundary Σ and entering a medium with a slower acoustic speed. S is a point source; D_1 and D_2 are detectors; ϕ_1, ϕ_2, and ϕ_3 are the incidence angles; θ_1, θ_2, and θ_3 are the transmission angles; the solid lines represent acoustic rays; B_1, B_2, and B_3 are three points at the parenchyma wall; v_p, v_{s0} are the mean acoustic speeds in the parenchyma tissue and the fat tissue, respectively, and $v_p > v_{s0}$.

respectively; ϕ_1, ϕ_2, and ϕ_3 are the angles of incidence; θ_1, θ_2, and θ_3 are the angles of transmission; and the solid lines represent the acoustic rays. Since the boundary is convex, it can be inferred that rotation from the normal at point B_2 to the normal at point B_1 is clockwise and the angle is θ_0 (positive). We also have $\phi_2 < \theta_0 + \phi_1$, which can be seen by extending lines SB_2 and SB_1 to the outside of the boundary and noticing that SB_2 and SB_1 will never intersect outside the boundary. To prove B_2D_2 and B_1D_1 will not intersect outside the boundary, we need to show $\theta_2 < \theta_0+\theta_1$. According to Snell's law, we have

$$\begin{aligned} \sin\theta_2 &= (1-\alpha)\sin\phi_2 \\ \sin\theta_1 &= (1-\alpha)\sin\phi_1, \end{aligned} \tag{4.1}$$

where $\alpha = 1 - v_{s0}/v_p$, which is positive when $v_p > v_{s0}$. The problem can be discussed under two conditions:

(a) $\phi_2 < \phi_1$. In this case, according to (4.1), we have $\theta_2 < \theta_1$ and therefore $\theta_2 < \theta_0 + \theta_1$.

(b) $\phi_2 \geqslant \phi_1$. (4.1) can be transformed to:

$$\begin{aligned} \sin(\frac{\theta_1-\phi_1}{2}) &= -\frac{\alpha\sin(\phi_1)}{2\cos((\theta_1+\phi_1)/2)} \\ \sin(\frac{\theta_2-\phi_2}{2}) &= -\frac{\alpha\sin(\phi_2)}{2\cos((\theta_2+\phi_2)/2)}. \end{aligned} \tag{4.2}$$

Since $\phi_2 \geqslant \phi_1$ and consequently $\theta_2 \geqslant \theta_1$, it is straightforward to obtain $\theta_2-\phi_2 \leqslant \theta_1-\phi_1$ from (4.2). Using $\phi_2 < \theta_0+\phi_1$, we have $\theta_2 < \theta_0+\theta_1$. In conclusion, we prove that after the rays from a point source go into another medium with a slower acoustic speed, the rays cannot intersect with each other when the interface is convex. In another words, for any pairing of point source and detector, there is only one acoustic path that satisfies Snell's law. Consequently, no multipath interference occurs and amplitude distortion can be ignored. This conclusion can also be applied to a boundary with wavelength-scale concave segments. This kind of boundary can be treated as a convex boundary approximately because the effects of the small concave segments can be neglected when the detector are placed in the far field of the segments, as will be shown in the following subsection. In contrast, multipath interference does occur after rays pass a convex parenchyma wall in ultrasound imaging, as shown in Fig. 13. This difference makes the amplitude distortion in TAT of the breast with a convex, or approximately convex parenchyma wall, smaller than that in pure ultrasound imaging.

b. Concave Boundary

We realize that, in reality, the boundary between mammary tissue and subcutaneous fat tissue might be concave and quite irregular. In this subsection, we will show that the amplitude distortion caused by a concave boundary is not severe. Basically, this conclusion can be explained as follows. With wavelength-scale or smaller heterogeneities, amplitude distortion of the wavefronts is minor due to diffraction when the detectors are placed in the far field of the irregular boundary segment. When the size of the concave segment is larger, according to the imaging formula of concave boundaries shown below, only imaginary images exist after the wavefronts from real objects pass through the concave boundary. Equivalently, no two rays from a point source will intersect with each other after passing through the concave boundary segment and no strong amplitude distortion occurs. In the following subsection, we will define two kinds of multipath interference: focusing-type and nonfocusing-type interferences. The former can induce amplitude distortion in both narrowband and broadband signals, while the latter can only induce amplitude distortion in narrowband signals. As a consequence, we need only examine in detail the focusing-type interference, because signals in breast TAT are broadband.

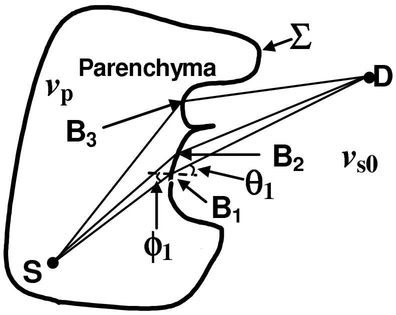

Fig. 16. Diagram to show two types of multipath interferences caused by a concave boundary: focusing-type interference between SB_1D and SB_2D, and nonfocusing-type interference between SB_1D (SB_2D) and SB_3D. In a focusing-type interference, the different rays have approximately the same time-of-flight (TOF), which consequently yields constructive interference and strong amplitude distortion; in this case, the boundary segment around B_1B_2 can be considered as a lens. In nonfocusing-type interference, the difference of the TOFs along two rays is larger than the pulse width, and, consequently, the pulses are separated temporally and no strong amplitude distortion occurs. See Fig. 15 for the symbols' definitions.

c. Definition of Focusing-type and Nonfocusing-type Interferences

Fig. 16 shows the two different kinds of multipath interferences. Three different ray paths SB_1D, SB_2D, SB_3D from source S to detector D are shown, and each of them satisfies the refraction law. SB_1D and SB_2D can be considered as a small modification of the straight line SD due to weak heterogeneity, while SB_3D is far away from SD. We use focusing-type interference to refer to the interference between pulses along the paths with the same TOFs. The interference between SB_1D and SB_2D is of this type. This is because SB_1D and SB_2D satisfy the refraction law, and their TOFs are local minima according to Fermat's principle [28]. Consequently the rays around SB_1D and SB_2D should have almost the same TOF. After noticing that B_1 and B_2 are close to each other, it can be inferred that SB_1D and SB_2D have the same TOFs. Actually, the boundary segment around B_1B_2 can be considered a focusing lens and can produce strong amplitude distortion even for broadband pulses, as verified by the strong amplitude distortion in broadband breast ultrasound imaging [67]. As a contrast, we use nonfocusing-type interference to refer to the interference between the pulses along paths with different TOFs. The interference between SB_3D and SB_1D (SB_2D) is a nonfocusing-type interference, because B_3 is far from B_1 and B_2, and generally, it can be assumed that $|t_{SB_1D} - t_{SB_3D}|$ and $|t_{SB_2D} - t_{SB_3D}|$ (t_{SB_1D}, t_{SB_2D}, and t_{SB_3D} are the TOFs along ray paths SB_1D, SB_2D, and SB_3D respectively) are larger than 1 μs, the average pulse width of thermoacoustic signals in our RF TAT experiments. Consequently, the pulse along SB_3D is separated temporally from the pulses along SB_1D, SB_2D and the interference between SB_3D and SB_1D (SB_2D) is insignificant. Similar analyses can be found in the pure ultrasound imaging literature [67].

The signals along SB_3D may introduce artifacts in the reconstructed images because detector D receives two pulses from source S–one along SB_1D and SB_2D, and the other along SB_3D. To estimate the effects of signals along path SB_3D, we numerically simulate refractions at arbitrary boundaries, where the locations of source S and detector D are randomly chosen. We find that the SB_3D type refraction rarely occurs. Therefore, we expect the artifacts introduced by the signals along SB_3D to be insignificant, and in the following studies, we consider only focusing-type interference.

d. Analysis of Focusing-type Interference

For a boundary segment with a size of $2a$ much larger than the wavelength of interest λ, we will use a ray model to study the effects of refraction. To have focusing-type interference, the positions of the source and detector must satisfy the following equation,

$$\frac{1}{l_{SB_1}/\cos\phi_1} + \frac{1}{l_{B_1D}(1-\alpha)/\cos\phi_1} = \frac{\alpha}{R_l} = \frac{1}{f}, \tag{4.3}$$

where f is the focal length of segment B_1B_2 in Fig. 16 and $f = R_l/\alpha$; R_l is the radius of the segment; and l_{SB_1} and l_{B_1D} are the lengths of line SB_1 and DB_1, respectively. The derivation of (4.3) can be found in Appendix C. To have a real image, or equivalently to have two rays intersect after passing through boundary segment B_1B_2, (4.3) requires

$$l_{SB_1}/\cos(\phi_1) > R_l/\alpha. \tag{4.4}$$

Next, we derive another requirement due to diffraction for the occurrence of strong amplitude distortion. The smallest beam width after a wavefront passes through a boundary segment with a size of $2a$ is $l_{B_1D}\lambda/a$, where λ is the wavelength of the acoustic wavefront. To induce strong focusing, or equivalently strong amplitude distortion at detector D, the beam width should be smaller than a at D; therefore, we have

$$l_{B_1D} < a^2/\lambda. \tag{4.5}$$

The right-hand side of the above inequality is the same as the definition of the near-field length of a plain transducer when a is considered as the radius of the transducer. It is well known that the amplitude can change rapidly in the near field, while it is much smoother in the far field. Similarly, if the detector is placed within the far field of the concave boundary segment, the amplitude distortion will be less severe in TAT.

(4.5) is derived for the case where a wavefront propagates perpendicularly to the boundary segment. When a wavefront is incident obliquely upon the segment B_1B_2, the effective size of the lens in (4.5) should be the projection of its geometrical size onto the plane perpendicular to the propagation direction of the incident wave. Then we have:

$$l_{B_1D} < (a\cos\phi_1)^2/\lambda. \tag{4.6}$$

By combining (4.6), (4.4) and $R_l > a$, we achieve the following requirement for strong amplitude distortion after passing through the boundary:

$$l_{SB_1} > \frac{\sqrt{l_{B_1D}\lambda}}{\alpha}. \tag{4.7}$$

It can be seen from this equation that when l_{B_1D} is large enough,

$$l_{B_1D} > \frac{(l_{SB_1}\alpha)^2}{\lambda}, \tag{4.8}$$

the strong amplitude distortion can be minimized. Notice that the required minimum detection distance in (4.8) increases linearly with the frequency of the wave.

In the derivation of (4.3), ray theory is utilized. Ray theory is valid under the following conditions [78]:

$$l_{B_1D} << 4a^2/\lambda, \tag{4.9}$$

and

$$2a >> \lambda. \tag{4.10}$$

(4.9) is similar to (4.5), but the former is stronger. (4.9) states that the ray model is valid when the wave propagation distance from the heterogeneity is smaller than $4a^2/\lambda$; beyond that distance, diffraction must be considered. In our analysis of amplitude distortion in TAT, we extend the effective range the ray model from (4.9) to (4.5). This is based on the assumption that the ray model overestimates the wavefront distortions due to ignorance of the diffraction effect. Therefore, if the analysis using ray theory shows that there is only minor amplitude distortion when (4.8) and (4.10) are met, the analysis from the exact wave equation should yield the same result.

For a wavelength-scale boundary segment, for example $2a < 4\lambda$, (4.10) is violated, and (4.8) cannot be applied. In this case, strong amplitude distortion can be minimized by placing the detector within the far field of the heterogeneity,

$$l_{B_1D} > 4\lambda, \tag{4.11}$$

where we have substituted $2a < 4\lambda$ into (4.5). Combining (4.8) and (4.11), we obtain the minimum detection distance for avoiding strong amplitude distortion induced by different scales of heterogeneities

$$l_{B_1D} > MAX[\frac{(l_{SB_1}\alpha)^2}{\lambda}, 4\lambda], \tag{4.12}$$

where $MAX[]$ represents computing the maximum. Using the following parameters, $l_{SB_1} < 10$ cm (the assumed size of the breast parenchyma), and $\alpha = 0.07$, where the mean velocity in the subcutaneous zone v_f and the breast parenchyma v_p are assumed to be 1437 m/s [79] and 1546 m/s [80], respectively, we have $l_{B_1D} > 4.9$ cm for 1.5 MHz ultrasound and $l_{B_1D} > 1.63$ cm for 0.5 MHz ultrasound. These requirements can be easily met in TAT experiments. For ultrasound waves with a frequency less than 0.5 MHz, it is not necessary to apply (4.12), because ultrasound scattering by soft tissue in this frequency range can be neglected and no severe amplitude distortion is expected.

The above analysis is made for 2-D TAT. This corresponds to the experimental configuration where a linear, or ring array of transducers with a cylindrical surface is used and a section image of the breast in the detection plane is desired. However, because of the refraction at the parenchyma wall, the thermoacoustic waves from the objects within the detection plane might deviate out of the plane. On the other hand, the signals collected in the detection plane are transmitted by the objects out of the detection plane rather than within it. Consequently, the obtained image is actually a projection of the out-of-plane objects onto the detection plane. To reduce this kind of error, we can use the technique of compressing the breast against the chest wall, which has proven to be effective in reducing wavefront distortions in breast ultrasound imaging. After the compression, the acoustic signals can pass through the interface more or less perpendicularly. However, the ultimate solution to this problem is 3-D TAT. Most of the 2-D results on amplitude distortions, such as (4.6), (4.8) and (4.12) and the results on phase distortions shown later, can be directly applied to 3-D TAT. (4.3) can also be applied to analyze a 3-D convex boundary locally by substituting - R_l for R_l. Then, it is straightforward to see that in a 3-D case no two rays can intersect with each other after passing a convex boundary segment.

In summary, our analysis shows that in RF breast TAT, if the detection is made at a distance to the breast surface farther than that required by (4.12), the amplitude distortion caused by the refraction at the parenchyma wall is not important because of the diffraction effect and the fact that TAT signals are broadband, have low central frequency, and experience only one-way transmission through the parenchyma wall. The effect of intramammory fat lobules will be addressed in the Discussion Section. Therefore, in the following analysis and simulations, we will consider only phase distortion.

2. Phase Distortion Caused by Refraction and Speed Variation

If the background is acoustically homogeneous, an acoustic ray from source S in Fig. 14 goes along the straight line SD to reach detector D. When there is acoustic heterogeneity, an acoustic ray goes along line SB_1D because of refraction at the interface. Assume there is no change in the shape of the acoustic pulse caused by acoustic heterogeneity. The TOF from source S to detector D in the acoustically heterogeneous model is

$$t_{SB_1D} = \int_{SB_1D} dl/\nu_s(\mathbf{r}''), \tag{4.13}$$

where $v_s(\mathbf{r}'')$ is the local acoustic speed, and $\mathbf{r}''$ is a point within line SB_1D. Now, we will show that t_{SB_1D} can be approximated to the second order of a small value $\varepsilon = (v_s(\mathbf{r}'') - v_{s0})/v_{s0}$ by $t_{SD} = \int_{SD} dl/\nu_s(\mathbf{r}'')$, where v_{s0} is the velocity used in the acoustically homogeneous model. According to Fermat's principle, an acoustic ray travels on the fastest path. In another words, SB_1D is a local minimum of TOF. Now assume B_1 is displaced to B' by a small distance $q = |BB'|$,

$$\frac{q}{l_{SD}} = o(\varepsilon). \tag{4.14}$$

After expanding $t_{SB'D}$ around t_{SB_1D} with respect to q, we have

$$t_{SB'D} = t_{SB_1D} + q \left.\frac{\partial t_{SB'D}}{\partial q}\right|_{q=0} + o(\varepsilon^2). \tag{4.15}$$

Recalling that SB_1D is a local minimum, we have $\left.\frac{\partial t_{SB_1'D}}{\partial q}\right|_{q=0} = 0$. Substituting it into (4.15) and assuming $l_{B_2B_1}/l_{SD} = o(\varepsilon)$ due to the weak acoustic heterogeneity in breast tissue, we have

$$t_{SD} = \int_{SD} dl/\nu_s(\mathbf{r}'') = t_{SB_1D} + o(\varepsilon^2). \tag{4.16}$$

The above result can be understood in the following way. Although the path length of SB_1D in Fig. 14 is longer than that of SD and $(l_{SB_1} + l_{DB_1} - l_{SD})/l_{SD} = o(\varepsilon)$, path SD has a longer part within the slow-speed area than path SB_1D. The combination of the two opposite effects leads to the cancellation of the first-order term of ε in (4.16).

Next we will show that the approximation of t_{SB_1D} by t_{SD} includes most of the flight-time variation induced by acoustic heterogeneity. The TOF from source S to detector D in an acoustically homogeneous and heterogeneous model is l_{SD}/v_{s0} and

t_{SB_1D}, respectively. The difference between them is

$$\delta t = |t_{SB_1D} - l_{SD}/v_{s0}| = |t_{SB_1D} - t_{SD} + t_{SD} - l_{SD}/v_{s0}| \approx \left|o(\varepsilon^2) + t_{SD} - l_{SD}/v_{s0}\right| \approx o(\varepsilon), \tag{4.17}$$

where we used (4.16). Combining δt with (4.16), we have

$$\frac{|t_{SD} - t_{SB_1D}|}{\delta t} = o(\varepsilon). \tag{4.18}$$

Therefore, the error in the approximation of t_{SB_1D} by t_{SD} is not important. At last, it should be pointed out that our analysis of TOF can be applied to both 2-D and 3-D TAT.

3. Forward Formula in an Acoustically Heterogeneous Model

In our analysis of TOF, we consider only a single interface. The results can be extended to the case involving several interfaces. In general, the TOF from $\mathbf{r}$ to $\mathbf{r}'$ can be expressed as

$$t_f(\mathbf{r}', \mathbf{r}) = \int_{L(\mathbf{r}',\mathbf{r})} dl/\nu_s(\mathbf{r}'') + o(\varepsilon^2), \tag{4.19}$$

where $L(\mathbf{r}', \mathbf{r})$ is the straight line from $\mathbf{r}'$ to $\mathbf{r}$, and $\mathbf{r}''$ lies within the line L. Combining (4.19) and (1.7), we obtain the forward formula for acoustically heterogeneous TAT.

Our analysis of TOF is in agreement with the results from a more rigid model [81]. It was reported that the variation in travel time caused directly by acoustic speed heterogeneity is a first-order perturbation, and that the effect of the ray bending on the travel times is a second-order one. For breast tissue, which is weakly acoustically heterogeneous, it is enough to consider the first-order perturbation by computing the integral of the slowness perturbation along straight lines, as shown in (4.19).

C. IMPLEMENTATION AND MODELLING OF NUMERICAL SIMULATIONS

1. Numerical Implementation

It can be seen from (1.7) that $p_1(\mathbf{r}, t)$ can be obtained from $\varphi(\mathbf{r}')$ after applying two linear operations to it: one is integration over the object space; the other is differentiation over t. Therefore, in its discrete form, (1.7) is a set of linear equations:

$$\mathbf{M}\varphi = \mathbf{p}, \tag{4.20}$$

where $\mathbf{M}$ is the matrix representing the product of the two linear operators. The standard techniques of solving a linear equation system can be utilized. We adopted the TCG method to minimize the object function $\|\mathbf{M}\varphi - \mathbf{p}\|$ and no preconditioner is used. In the implementation of TCG, instead of the whole matrix $\mathbf{M}$, a function that gives the multiplication of matrix $\mathbf{M}$ and its adjoin with an arbitrary vector is required. Consequently, the demand on computer memory is reduced greatly, compared with many other techniques that require storing the whole matrix $\mathbf{M}$ in memory. Another advantage of TCG is that an approximate result can be obtained by stopping the iteration before reaching the full convergence. The truncation not only saves computation time but also provides a way of regularization for stabilizing the results. In (4.19), we use the Savitzky-Golay smoothing method [82], rather than the finite differentiation method to implement the operation of the first-order temporal derivative, as the former yields a much smoother and more accurate result than the latter when data are noisy. We truncated our simulations after 15 iterations, which corresponds to the relative changes in the norms of the results, about 0.7% for the acoustically homogeneous model and up to 6% for the acoustically heterogeneous model. In both cases, further iterations yield little visible improvement to image quality and may induce instability.

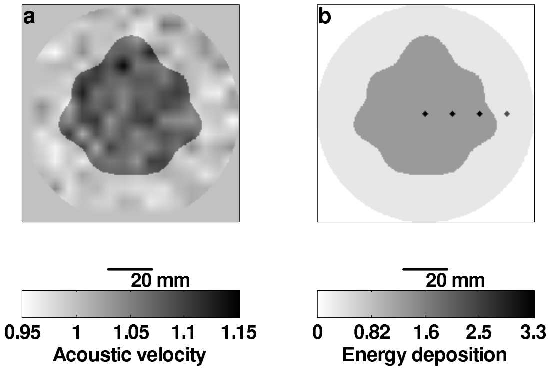

Fig. 17. Distribution of acoustic velocity and microwave absorption. (a) Distribution of acoustic velocity normalized to v_{s0} for a breast model. The breast surface is represented by the outer circle; the wall between the breast parenchyma and the subcutaneous fat is represented by the inner irregular boundary. (b) The microwave absorption distribution in our model. The four small spots represent the assumed tumors.

In our simulations, we choose the 2-D case rather than the 3-D case because the computational complexity can be reduced and because it is much easier to interpret and graph a 2-D image. For the 2-D case, the integration in (1.7) is over a curve instead of a spherical surface:

$$p_1(\mathbf{r}, t) = \frac{\beta I_0 v_{s0}}{4\pi C} \frac{\partial}{\partial t} \oint_{t=t_f(\mathbf{r}',\mathbf{r})} \frac{\varphi(\mathbf{r}')}{|\mathbf{r}-\mathbf{r}'|} d\mathbf{r}' \ , \tag{4.21}$$

where t_f is determined by (4.19). Nevertheless, the conclusions of a 2-D case can be extended to a 3-D one.

2. Model and Parameters in Numerical Simulations

Fig. 17 (a) and (b) illustrate the acoustic and RF absorption models of the breast, respectively. The acoustic model of the breast in our simulations is based on experimental results on the distribution of acoustic speed in the breast [77, 83]. Acoustic speed in the breast may vary from 1400 m/s to 1550 m/s. Generally, a zone of low velocity (1400-1450 m/s) characterizes subcutaneous fat [83]. The speed in normal dense parenchyma is higher, varying from 1500m/s to 1550 m/s [80]. In Fig. 17 the outer circles, with a radius of 50 mm, represent the breast surface. The inner irregular boundaries, which are generated by randomly modifying a circle, represent the walls of the breast parenchyma. The size of the parenchyma tissue was changed in different simulations because the ratio of breast parenchyma to subcutaneous fat may change with age. Usually, a young female breast has less fat than an older one does. The mean velocity in the subcutaneous zone v_f and the breast parenchyma v_p are set to be 1437 m/s [77] and 1546 m/s [80], respectively. A random component, which is a normal distribution with a mean of zero and a variance of 33 m/s, is added to the velocity distribution to simulate the velocity fluctuations in the subcutaneous zone [83] and the breast parenchyma [80]. Later, our simulation results show that the random component of velocity will induce little spread in the images due to the cancellation after integration. To ensure that the acoustic speed does not change sharply within each tissue, the random component is smoothed spatially by introducing a correlation length as shown below. The imaged area is divided into patches with side dimensions of a correlation length. The value of the random component at the center of each patch is determined according to the normal distribution mentioned above; then the random component within the patch decreases linearly to zero at the boundary of the patch. We tried different correlation lengths in our simulations, from 12 mm (about the size of fat lobules in parenchyma tissue) to 3 mm. The image degrades more with increasing correlation length, but the difference is minor. The correlation length was chosen to be about 6 mm for the reported results. The speed distribution in Fig. 17 was normalized to 1437 m/s, which is assumed to be the acoustic velocity in the medium surrounding the breast and also the acoustic speed in the subcutaneous fat.

The RF absorption model of the breast is shown in Fig. 17(b). The boundary shapes are the same as in Fig. 17(a). The outer circle is quite weak because of the low microwave absorption rate of fat. RF absorption coefficients in fat, tumors, and the coupling oil are set to be 0.3, 3, and 0 after being normalized to that in the parenchyma. The tumors, shown in Fig. 17(b) as dark spots, are placed evenly along the horizontal direction to study the dependence of the distortions in the images based on the tumor locations. We set the radii of the four tumors to about 1.2 mm to simulate approximately the point-source spread caused by acoustic heterogeneity.

The parenchyma wall in our simulation is generated as the following equation: $r(\theta) = r_p(1 + Ag(\theta))$, where $r(\theta)$ is the radius of the boundary at angle θ; r_p is the mean radius of the boundary and is used to represent the size of the parenchyma tissue; A is the distortion amplitude; and $g(\theta)$ generates random numbers within [-1,1].

The parameters in our simulations are chosen as follows unless stated otherwise. Noise is added to the generated signals so that the frequency range with signal-to-noise ratio (SNR) larger than unity is from 0 to 1.5 MHz, which approximates our experimental results [13]. The radius of the circle of detection is set to be 125 mm to meet (4.8); the angle range of detection is 2π with 400 steps. An insufficient number of scanning steps can cause radial aliases in the reconstructed image [25]. Thermoacoustic signals are sampled for 108 μs at a sampling rate of about 14 MHz, which is sufficient to meet the Nyquist criteria. The 100 mm by 100 mm imaging field is mapped with a 256 by 256 mesh. In our simulations, the thermoacoustic signals are generated in an acoustically inhomogeneous model, while the reconstruction is implemented for two cases–with and without the consideration of acoustic heterogeneity.

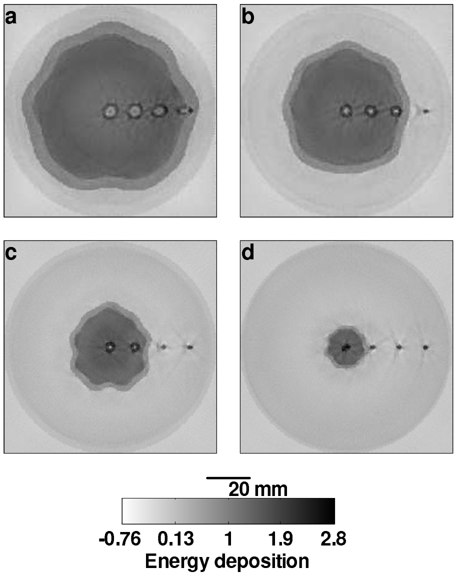

Fig. 18. (a)-(d) Images when acoustic heterogeneity is not considered in the reconstructions. The mean radii of the parenchyma wall are set to be 0.8, 0.6, 0.4 and 0.2 of the breast radius, respectively. The point-spread width and the boundary-spread width increase linearly with the size of the parenchyma tissue. Note that the spread of points outside the parenchyma tissue are much smaller than the spread inside.

D. NUMERICAL RESULTS

We first study the effect of acoustic heterogeneity on imaging when acoustic heterogeneity is considered in the forward problem but not in the reconstruction. In the reconstruction, $v_s(\mathbf{r})$ in (4.19) is set to be v_{s0}. Then we show how to improve image resolution after considering acoustic heterogeneity in the reconstructions. Lastly, the effects of measurement errors in v_f, v_p and Σ on the improvement are investigated.

1. Reconstruction without Considering Heterogeneity

Fig. 18(a)-(d) shows the results when acoustic heterogeneity is not considered in the reconstructions. In the four simulations, the mean radii of the parenchyma wall r_p

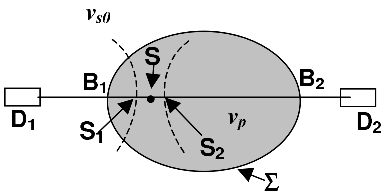

Fig. 19. Diagram for deriving (4.22), which estimates the spread of a point source S along line D_1D_2 due to TOF error. S_1 is the intersection of D_1D_2 with the backprojection arch of the signal transmitted by source S and detected by detector D_1; S_2 is the corresponding one at D_2.

are set to be 0.8, 0.6, 0.4 and 0.2 of the breast radius. The wall is distorted randomly in the simulations and the distortion amplitude is 0.1. We measure the point-spread width (PSW), which is the width of the image of a point source along a specific direction minus its real size, 2.4 mm, and the boundary spread width (BSW), which is the width of the blurred parenchyma wall Σ in an image. It is clear from Fig. 18 that PSW and BSW increase with the radius of the parenchyma wall. It is proved in Appendix D that the two widths can be estimated by the following equation:

$$w = l_p \alpha, \tag{4.22}$$

where l_p is $2r_p$ in the case of BSW; in the case of PSW, l_p is the length of a ray within the parenchyma tissue along a specific direction (for example the length of B_1B_2 in Fig. 19). The PSW is anisotropic because l_p depends on direction. This anisotropy of PSW can be verified by the observation that the three tumors within the parenchyma tissue in Fig. 18(a) and (b) have the same spread along the horizontal direction, while their spreads along the vertical direction decrease when the tumors are located away from the center. Fig. 20 shows the quantitative results (with an error of ± 0.8 mm) of the PSW and BSW along the horizontal direction in eight simulations where the radius changes from 0.1 to 0.8 of the breast radius with a step of 0.1. The corresponding linear fitting results for the PSW and BSW are shown

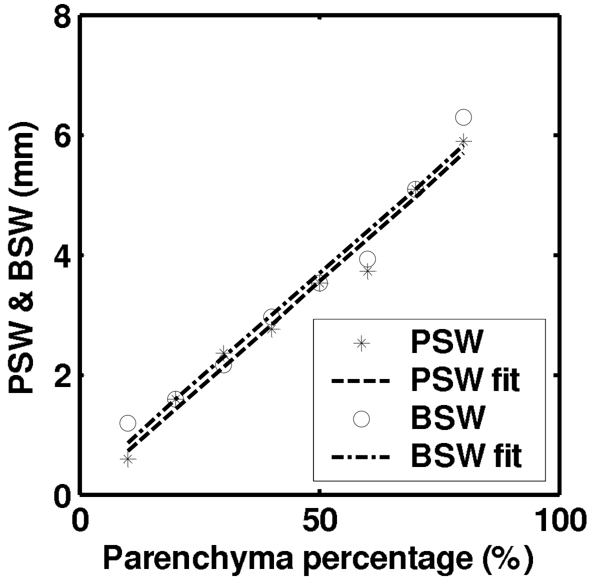

Fig. 20. Quantitative results of the point-spread width and boundary-spread width along the horizontal direction in eight simulations where the mean radius of the parenchyma wall changes from 0.1 to 0.8 of the breast radius using a step of 0.1. The corresponding linear fittings of PSW (dashed) and BSW (dash-dotted) are in good agreement with the proposed formula (4.22).

as dashed and dash-dotted lines, respectively. The slopes of the two lines are 0.071 and 0.0705, respectively, both of which are close to the estimated rate of 0.07 derived from (4.22) after substituting the parameters used in our simulations, the radius of the breast $r_b = 50$ mm and $\alpha = 0.07$. Another interesting point in Fig. 18 is that the PSW of the objects outside the parenchyma tissue are affected little by acoustic heterogeneity. Only minor artifacts are observed near them. This is because in TAT a π- or wider view can provide complete data for reconstruction [22]. In this case, a view means the angle subtended by the detection curve when observed from the to-be-imaged object. For example, object A in Fig. 21 has a view larger than π while object B's is less than π. If an object is outside the parenchyma tissue, it has at least a π-view detection range in which the medium between the object and the detectors is

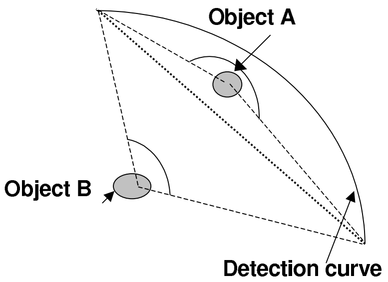

Fig. 21. Diagram to show the limited-view TAT. It shows that in TAT a π- or wider view can provide complete data for reconstruction. A view means the angle subtended by the detection curve when observed from the to-be-imaged object. Object A has a view larger than π, and object B has a view less than π.

acoustically homogeneous. Therefore, a perfect image can be reconstructed from this part of the data. On the other hand, the image reconstructed from the part of signals that experience the heterogeneous medium is weak in amplitude because the flight-time errors compromise the build-up strength of the signals. In addition to blurring of images, acoustic heterogeneity increases the background noise level and decreases the values of reconstructed tumors, which consequently reduces the contrast of tumors in the images and the detectability of small tumors. A comprehensive quantitative study of this issue will depend on the SNR of the hardware of the imaging system, the parameters of the imaging system and reconstruction algorithms, and the contrast of the to-be-imaged objects. Meaningful conclusions should be made based on relevant experimental data which we leave for future study.

2. Reconstruction with the Consideration of Heterogeneity

The exact distribution of acoustic velocity is included in the model in Fig. 22(a). Although the result is good, it is not practical, because it is not feasible to obtain the exact distribution of velocity in the breast by current technology. A much more practical situation is when the mean velocities v_f, v_p and boundary profile Σ are approximately known while the velocity fluctuation within each area is unknown. Different approaches to obtain v_f, v_p and boundary profile Σ will be explored in detail in the Discussion Section. Here, we will show the effectiveness of our compensation method. Fig. 22(b)–(f) shows the images reconstructed from the same data as in Fig. 22(a) but the reconstruction algorithm used only v_f, v_p and Σ to study the effects of the measurement errors in v_f, v_p and Σ on the improvement. In Fig. 22(b)–(f), the random component of the acoustic-velocity distribution is ignored. In addition, v_p is decreased by 1% and 3% in Fig. 22(c) and (d), respectively; Σ is scaled down by 10% in Fig. 22(e), and a 20% random error is introduced to Σ in Fig. 22(f). Fig. 23(a)-(f) are the corresponding close-up images around the central tumor in Fig. 22. r_p in these simulations is 0.6 of the breast radius, and the distortion amplitude of the parenchyma wall is 0.2.

a. Effect of Errors in Velocities

There is little difference between the resolution of the reconstructed images when we consider [Fig. 23(a)] and do not consider [Fig. 23(b)] the random component of velocity distribution, although the artifacts in the background in Fig. 23(b) are a little stronger than those in Fig. 23(a). The good resolution, after ignoring the random component of the acoustic-velocity distribution in Fig. 23(b), can be explained by modifying (4.22) to:

$$w = \int_{B_1 B_2} \alpha(\mathbf{r}'') dl_p, \tag{4.23}$$

where $\alpha(\mathbf{r}'') = 1 - v_{s0}/v_p(\mathbf{r}'')$ and is spatially dependent; the integration is over the line B_1B_2 in Fig. 19 . It can be found that the contributions of the random component of velocity are cancelled in some degree after the integration over an acoustic ray.

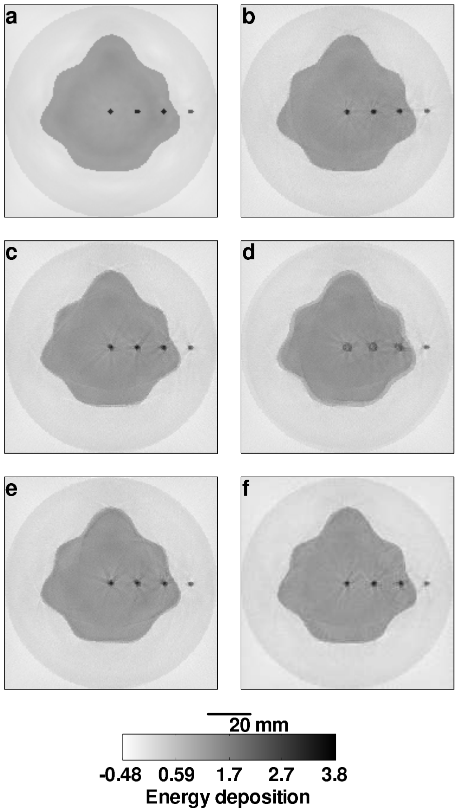

Fig. 22. Compensation for the degradation in images. (a) Complete acoustic heterogeneity information is included in the reconstructions. (b) Only exact v_p, v_f, and Σ are included to show the insensitivity of improvement to a random component of the acoustic-velocity distribution. (c) and (d) Images when there are 1% and 3% errors in v_p, respectively. (e). Images when Σ is scaled down by 10%. (f) Images when 20% random error is introduced in Σ. The above results show the stability of the improvement to the errors in v_p, v_f, and Σ.

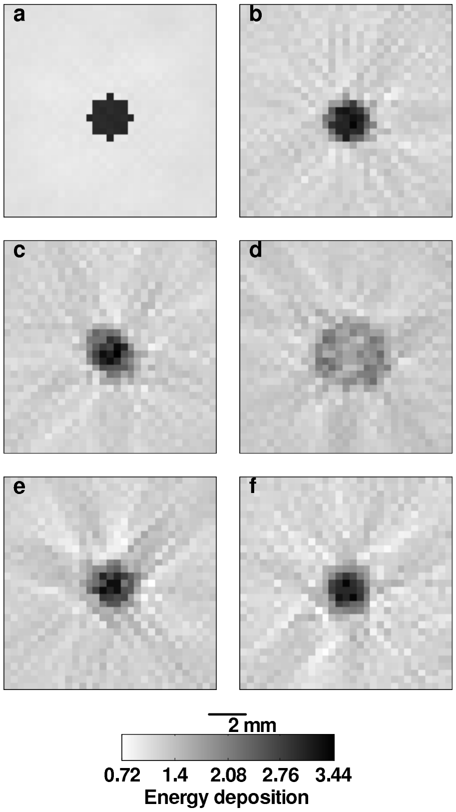

Fig. 23. (a)-(f) Close-up images around the central tumor in Fig. 22(a)-(f), respectively.

Comparing Fig. 23(c)–(d) with Fig. 23(b), it should be noted that a 1% error in v_p does not degrade the imaging quality much, while a 3% error in v_p greatly deteriorates the imaging resolution and contrast. This is because in our model, the difference between v_f and v_p is about 7% of their speeds, and a 3% error in v_p actually accounts for 42% of the difference between v_f and v_p. Therefore, we conclude that an accuracy of 1% in the determination of v_p is sufficient for significant improvement in imaging resolution.

b. Effects of Errors in Determining Σ

In the model in Fig. 23(e), the boundary Σ is scaled down by 10%. In Fig. 23(f), a random component is added to the real boundary, which is implemented by multiplying the real radii of a boundary with uniform random numbers within [0.8,1.2]. After comparing Fig. 23(e) and (f) with other figures in Fig. 23, it is found that compensation is less sensitive to error in determining Σ as v_p. This is because a 10% error, which is about 6 mm in the diameter of the parenchyma wall, adds at most 0.42 mm to the PSW and BSW according to (4.22).

E. DISCUSSION

1. Effect of Small Fat Lobules

In breast UT, cm-scale fat lobules in the parenchyma tissue can also cause significant distortion. In breast TAT, the amplitude distortion due to cm-scale fat lobules is estimated to be insignificant because of the diffraction effect, as discussed in the section on refraction in the concave boundary segments. For example, substituting a = 1 cm, λ =1.5 mm in (4.5), we obtain a near-field length of 6.7 cm. Therefore, no strong amplitude distortion is expected when detectors are placed farther than 6.7 cm from the lobule. In addition, Figs. 6 (b)-(d) shows that the images of point sources outside an acoustic heterogeneity are affected little by the acoustic heterogeneity due to the completeness of the π-view detection in TAT. This explanation can also be applied to the distortion caused by fat lobules. When a fat lobule on one side of an acoustic source causes severe distortion, the signals that are spared from severe distortion in other directions can still produce good images.

2. Determine v_f and v_p in Experiments

Our simulation results in Fig. 22(c) and Fig. 23(c) show that a 1% error in v_f and v_p will lead to minor blurring but that we still have enough definition to determine the configuration and location of the imaged objects. To determine v_f and v_p within 1% accuracy, we can try different speeds around the averages, which are 1437 m/s and 1546 m/s for fat and breast tissue, respectively, with a step size of 1% velocity. Optimum speeds can be determined by choosing the reconstructed image with the sharpest parenchyma wall, because errors in v_f and v_p will cause the spread of this boundary. Since the variations of v_f and v_p between individuals are about 2% and 4% respectively, only 15 trials are needed to scan all the combinations. Furthermore, the backprojection method [19] can be used in each trial because the boundary of the reconstructed image can be recovered well with this method [22, 56]. Therefore, the additional computation cost in the trials is estimated to be only double the total computation complexity.

3. Determine Σ in Experiments

There are two ways to obtain Σ. The first method uses only TAT signals. It takes advantage of the fact that fat and parenchyma have both acoustic and microwave contrasts. First, a TAT image is reconstructed with an acoustically homogeneous model. Then an approximate Σ can be extracted from the image and plugged into an acoustically heterogeneous reconstruction model to obtain a more accurate TAT image. As shown in Fig. 18, the boundary-spread of the parenchyma wall in TAT images is at most 7% of its real size (if $\alpha = 0.07$) when an acoustically homogeneous reconstruction model is used. Our studies on the effects on the reconstruction of the errors in the boundary profile, shown in Fig. 22(e) and Fig. 23(e), reveal that this level of error has little effect on the images reconstructed from a heterogeneous model. We intend to implement this method in our future work.

The second method for determining Σ is the coregistration of ultrasound B-scan imaging and TAT. In principle, this can be accomplished in the same set-up. First, TAT data is acquired. After that, the transducers work in pulse-echo mode to determine an approximate Σ. At last, this boundary information can be included in the reconstruction algorithm of TAT.

4. Differences between TAT and UT

The studies we presented show that there should be no severe amplitude distortion in breast TAT while severe amplitude distortion caused by refraction has been observed in both narrowband and broadband breast UT [67]. The difference between the effects of acoustic heterogeneity on TAT and UT can be explained by the different central frequencies. In UT, the central frequency is above 3 MHz, while in TAT, the central frequency is below 1 MHz. The higher frequency in UT results in stronger wavefront distortion due to the following reasons. First, the scattering effect increases rapidly with frequency; secondly, the minimum detection distance for avoiding strong amplitude distortion caused by an acoustic lens, which can be a boundary segment or a small inclusion, extends farther with increasing frequency. Substituting the following parameters for UT, $l_{SB_1} < 10$ cm, $\lambda = 0.5$ mm, and $\alpha = 0.07$ into (4.12), we have $l_{B_1D} > 9.8$ cm. We notice that the transducer or array was placed closer than the required distance to the breast [67, 68]. Therefore, it is not surprising to observe the strong interference effect in UT.

Another important difference between TAT and UT is that there is no speckle in our TAT images [24]. Speckle is an important factor limiting the quality of pure ultrasonic imaging. In our technology, the detected signals are primary acoustic waves rather than reflective or scattered waves as in UT. Further, the temporal frequency of the acoustic signals lies in a range from 0 to 1.5 MHz, which is only weakly scattered in the tissues. However, the issue of image speckle in more realistic medical imaging applications is a topic for future consideration.

5. Miscellaneous

Our analysis and numerical simulations have shown that breast TAT images can survive acoustic heterogeneity. The ultimate test, however, will come from clinical experiments on the breast where the motion artifacts due to breathing and cardiac movement, may introduce blurring. Such blurring of images is estimated to be on the order of the movement amplitude. To correct the blurring, we can monitor the breast motion, for example, placing a microwave absorber on the breast surface as a marker. Then the data on the breast motion can be used in the reconstructions to shift the detectors' positions and, consequently, compensate for the breast's displacement.

F. CONCLUSIONS

The effects of acoustic heterogeneity on TAT in the breast are studied. Our analysis shows that the amplitude distortion in the breast TAT is minor. There is no multipath interference in the breast TAT with a convex parenchyma wall, and the amplitude distortion is also not severe for concave boundary, because the TAT signals are broadband, have low central frequency, and experience only one-way transmission through the parenchyma wall. Therefore we consider only phase distortion in our numerical studies. The numerical results on the spread of point sources and boundaries caused by the phase distortion are in good agreement with the predictions of the proposed formula. It is shown that phase distortion can be compensated for when complete or partial information on the distribution of acoustic velocity in the breast is included in the reconstruction. It is found that improvement in the results is more sensitive to measurement error in v_f, v_p than Σ. Based on this sensitivity study, an approach to implement our compensation method using only TAT data is proposed. The differences between breast TAT and breast ultrasound imaging in relation to the effects of acoustic heterogeneity and speckles are accounted for by differences in their central frequency of ultrasound and detection configuration.

CHAPTER V

FAST RECONSTRUCTION ALGORITHMS

A. PLANAR GEOMETRY[1]

1. Introduction

In this chapter, I present our studies on an exact and fast reconstruction algorithm using a Fourier transform for TAT in a planar configuration. The reconstruction of an image by Fourier transform has been used in X-ray CT [28], ultrasonic reflectivity imaging [39, 29, 84] and diffraction tomography [30] successfully. The computation complexity is reduced greatly due to the efficiency of the Fourier transform. We developed image reconstruction by Fourier transform for planar TAT. Furthermore, some limitations from experiments, such as the effects of the finite size of the detectors and the finite length of the excitation pulse, are included explicitly in the reconstruction algorithm. The reconstruction algorithm is verified by both numerically simulated and experimental results. Our simulations also demonstrate that the blur due to the finite size of the detector surface, which is a key limiting factor on the resolution of images [10, 85], can be alleviated by deconvolution with respect to the size of the detector surface. Other effects that may cause blurring of images can be treated in a similar way. In our initial experiments, an image in good agreement with the real objects is reconstructed and the deconvolution improved the resolution of the imaging system.

---

[1] ©2002 IEEE. Reprinted, with permission from Y. Xu, D. Feng, and L.-H. Wang, "Exact frequency-domain reconstruction for thermoacoustic tomography: I. planar geometry," *IEEE Trans. Med. Imag.*, vol. 21, pp. 823–828, 2002.

2. Methods

a. Image Reconstruction

Assume that the detector scans within the plane $z = 0$ and that the object is distributed only in the half space $z' > 0$. In order to obtain a spatial resolution of about 1 mm, the microwave pulse should be set to less than ∼1 μs because the speed of sound in soft biological tissue is ∼1.5 mm/ μs. For these parameters, the diffusion term in the heat conduction equation is about six orders of magnitude less than the term of the first-derivative of the temperature [20]. Therefore, heat conduction can be ignored. This is known as the assumption of thermal confinement. If the acoustic signals are collected along a line or in a plane, for example at $z = 0$, following the line of Nortan and Linzer in [39], it can be shown that for the case $|k| > \rho$ and $z' > 0$, (1.6) can be transformed into

$$\bar{P}(u, v, k) = \frac{\beta v_s I_0 k \bar{\eta}(k) sgn(k)}{2C\sqrt{k^2 - \rho^2}} \int_0^{\infty} \Phi(u, v, z') \exp(-iz' sgn(k)\sqrt{k^2 - \rho^2}) dz', \quad (5.1)$$

where $k = \omega/v_{s0}$, $\rho^2 = u^2 + v^2$, $sgn(k)$ is the signum function,

$$\bar{P}(u, v, k) = \frac{1}{(2\pi)^2} \iint \bar{p}(x, y, 0, k) \exp(-i(ux + vy)) dxdy, \quad (5.2)$$

and

$$\Phi(u, v, z') = \frac{1}{(2\pi)^2} \iint \varphi(\mathbf{r}') \exp(-i(ux' + vy')) dx'dy'. \quad (5.3)$$

(5.1) can further be simplified to

$$\bar{P}(u, v, k) = \frac{\pi \beta v_s I_0 k \bar{\eta}(k) sgn(k) \Phi_1(u, v, sgn(k)\sqrt{k^2 - \rho^2})}{C\sqrt{k^2 - \rho^2}}, \quad (5.4)$$

where

$$\Phi_1(u, v, w) = \frac{1}{2\pi} \int_{-\infty}^{\infty} \Phi(u, v, z') \exp(-iwz') dz'. \quad (5.5)$$

The lower limit of the above integration is changed from 0 to $-\infty$ because $\Phi(u, v, z') = 0$ when $z' < 0$. (5.4) gives an exact mapping relation between the spectrum of the collected signals and the spectrum of the distribution of microwave energy deposition and is the essence of our reconstruction method. However, (5.4) stands only if the acoustic detector is a point detector. In practice, the detector is of finite size, whose surface shape can be described by $R(x, y)$. The signal from the detector $p_d(x, y, t)$ can be expressed as an integral of the acoustic wave $p(\mathbf{r}, t)$ over the detector surface:

$$p_d(x, y, t) = \iint\limits_{s} p(x', y', t)R(x' - x, y' - y)dx'dy'. \tag{5.6}$$

After transforming (5.6) into the temporal- and spatial-frequency domain, we have

$$\bar{P}_d(u, v, k) = 4\pi^2\bar{P}(u, v, k)\bar{R}(-u, -v), \tag{5.7}$$

where $\bar{P}_d(u, v, k)$ is the temporal and spatial Fourier transform of $p_d(x, y, t)$, and $\overline{R}(u, v)$ is the spatial Fourier transform of $R(x, y)$. Substituting (5.7) into (5.4) results in

$$\bar{P}_d(u, v, k) = \frac{4\pi^3\beta v_s I_0 k\bar{\eta}(k)sgn(k)\bar{R}(-u, -v)\Phi_1(u, v, sgn(k)\sqrt{k^2 - \rho^2})}{C\sqrt{k^2 - \rho^2}}. \tag{5.8}$$

Mapping the (u, v, k) space into the (u, v, w) space by the relation

$$w = sgn(k)\sqrt{k^2 - \rho^2} \tag{5.9}$$

yields an explicit expression for Φ_1:

$$\Phi_1(u, v, w) = \frac{Cw\bar{P}_d(u, v, sgn(w)\sqrt{w^2 + \rho^2})}{4\pi^3\beta v_s I_0 sgn(w)\sqrt{w^2 + \rho^2}\bar{\eta}(sgn(w)\sqrt{w^2 + \rho^2})\bar{R}(-u, -v)}. \tag{5.10}$$

At last, the distribution of the microwave energy deposition can be reconstructed from Φ_1 by a 3-D inverse Fourier transform. (5.10) gives an exact reconstruction algorithm for planar TAT for the first time. Furthermore, the effects of the finite size of the detectors and the finite length of the excitation pulse are included explicitly. From (5.10), it can be inferred that the reconstructed image spectrum $\Phi_d(u, v, w)$ from the experimental data without the consideration of these two effects, as was presented by previous researchers [10, 85], is related to the actual image spectrum $\Phi_1(u, v, w)$ by

$$\Phi_d(u, v, w) = 4\pi^2 \bar{\eta}(sgn(w)\sqrt{w^2 + \rho^2})\bar{R}(-u, -v)\Phi_1(u, v, w). \tag{5.11}$$

Both of the effects result in multiplications of a function to the actual image spectrum in the frequency domain. They are equivalent to convolutions in the spatial domain, which blur the reconstructed image. However, given the pulse shape and the surface configuration of the detector surface, the two effects can be reduced by deconvolution.

To summarize, the reconstruction procedure consists of the following steps:

(1) The signal from the detector $p_d(x, y, \bar{t})$ is Fourier transformed with respect to $\bar{t}$ to yield $\bar{p}_d(x, y, k)$. Deconvolution with respect to the finite pulse length can be implemented immediately after the Fourier transform.

(2) $\bar{p}_d(x, y, k)$ is Fourier transformed with respect to x and y, yielding $\overline{P}_d(u, v, k)$.

(3) According to (5.9)–(5.10), $\overline{P}_d(u, v, k)$ is mapped to $\Phi_d(u, v, w)$.

(4) $\Phi_d(u, v, w)$ is deconvoluted with respect to the finite size of the detector, giving $\Phi_1(u, v, w)$.

(5) $\Phi_1(u, v, w)$ is inversely Fourier transformed with respect to u, v, w to yield $\varphi(x', y', z')$.

The order of steps (4) and (5) can be exchanged so that more stable deconvolution algorithms can be applied. In numerical calculations, $\overline{P}_d(u, v, k)$ is obtained only at discrete points; hence the mapping from $\overline{P}_d(u, v, k)$ to $\Phi_d(u, v, w)$ needs interpolation, which can be a major source of distortion.

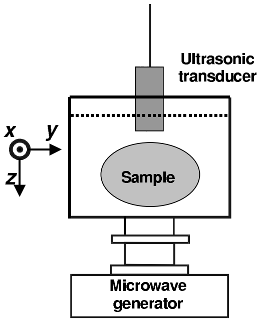

Fig. 24. Experiment setup of planar TAT.

b. System Setting

The experimental setup was reported in [64] and, for convenience, is only briefly described here Fig. 24. The x-axis points perpendicularly to the drawing plane; the y-axis points to the right in the plane; and the z-axis points downward along the acoustic axis. Microwave pulses are transmitted by a 9-GHz microwave generator. The pulse width is 0.5 μs. The object to be imaged is a cylinder of pork fat containing a thin layer of connective tissue and six yellow microstructures. The diameter of the cylinder fat is 14 mm and the length in the x direction 30 mm. The cylinder was immersed in mineral oil in a plexiglass tank. The central frequency of the ultrasonic transducer (Panametrics) is 2.25 MHz; the bandwidth 1.8 MHz; and the diameter of the active element 6 mm. More details about the system can be found in [64].

3. Results and Discussion

Our method was applied to reconstructing images from both the simulated and the experimental data in a 2-D case, where the imaged objects were uniform along the x-axis. Because the blur due to the finite size of the detector surface is a limiting factor on the resolution of images, we demonstrated how deconvolution with respect to the detector surface can deblur the images. We chose the 2-D case here because both the computational and experimental complexity can be reduced more in the 2-D case than in the 3-D one. Nevertheless, the extension of the conclusions of the 2-D case to the 3-D one is straightforward.

a. Simulation

The thermoacoustic imaging of two cylinders was numerically simulated. Cylinders were chosen because the analytical expression for their thermoacoustic signal is available [86]. In the simulations, the temporal-frequency range was from near 0 to 1.5 MHz, which was in accordance with the experimental one and with our previous experiments [13]. Two simulations were run. The first one was to test our reconstruction algorithm under an ideal experimental condition, which is noiseless and does not consider any experimental limitations on the detectors. In the second case, the effect of the finite size of the detectors on the imaging was studied while noise was also added. Deconvolution with respect to the finite size of the detector surface was applied to improve the lateral resolution of the blurred image. Since energy deposition is a positive value, only the positive components of the reconstructed image were retained, and the others were set to zero.

In step (3) of the reconstruction, which is the mapping from $\overline{P}_d(u, v, k)$ to $\Phi_d(u, v, w)$, linear interpolation was applied. By adopting the zero-padding technique [30] for the time-domain data, one can increase the sampling density in the k-space and, consequently, obtain a better performance of the interpolation in the k-space. In the reconstruction from the simulation data and experimental data, we appended to the end of the data the same number of zeros as in the original collected data, so that the sampling density in the k-space was doubled. By utilizing the Wiener filtering method [87], deconvolution with respect to the finite pulse length was implemented immediately after the Fourier transform with respect to time in step (1). As the deconvolution with respect to the finite size of the detector surface is much more unstable than the deconvolution with respect to the finite pulse length, we have tried two methods of deconvolution: the Wiener filtering method and the piecewise polynomial truncated singular value decomposition (PP-TSVD) [88] method. The first method can be implemented in the spatial-frequency domain and is more computationally efficient than the second, but the performance of the second method is much better, as it can restore sharp boundaries blurred by the convolution while avoiding the appearance of artificial oscillations in an unstable deconvolution. Therefore, we adopted the PP-TSVD method to process the images. Since the models in our simulation and experiment were uniform along the x-axis, one-dimension deconvolution was applied.

Fig. 25 shows the reconstructed image from the simulated data under the ideal experimental condition, where the radius of the two cylinders was 2 mm; the distance between the centers of the cylinders was 5.5 mm; the centers of the cylinders were positioned in the plane of $z = 10$ mm; the scanning range of the detector along the y axis was 90 mm with a step size of 0.5 mm; and the thermoacoustic signals were sampled for 40 μs at a sampling rate of 50 MHz. The reconstructed image is in good agreement with the real objects, whose outlines are plotted as dotted circles in Fig. 25. The dimension of the cylinders is 3.75 mm along the z direction and 4.7 mm along the y direction. The cylinder is a little deformed laterally, which is due to the finite scanning range of the detector. Fig. 26 shows the images before and after deconvolution with respect to the finite size of the detector surface in a case similar to our experimental conditions. The noise was added to the thermoacoustic signals, and the SNR was 50; the diameter of the detector was 6 mm. All of the other parameters were the same as those in the first case. The image before deconvolution is shown in Fig. 26(a). The dimension of the images of the objects is 3.5 mm along the z-axis, which agrees well with the real one, 4 mm. However, along the y-axis, the images of

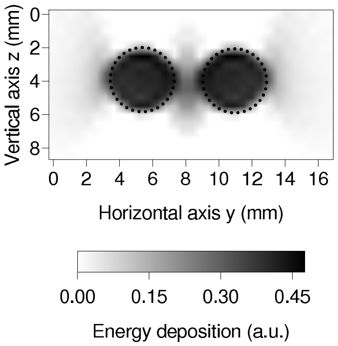

Fig. 25. The reconstructed image of the cross-section of two cylinders with a radius of 2 mm and the centers separated by 5.5 mm under ideal experimental conditions.

the two cylinders were blurred and consequently merged into one, which is predicted by our analysis of the effect of the finite size of the detector. The image shows no clear boundaries of the objects along the y-axis. After deconvolution, the lateral boundaries of the objects become very clear and the width of the objects in Fig. 26(b) is 4.1 mm, which is quite close to reality. Furthermore, the two objects can be distinguished clearly. After comparing Fig. 26(a) with Fig. 26(b), it seems that the ghost images become slightly more obvious, which is a disadvantage of deconvolution. Nevertheless, it is obvious that deconvolution with respect to the finite size of the detector surface can improve the lateral resolution greatly. In Fig. 25 and Fig. 26, there are some ghost images. In principle, our reconstruction method is exact under the assumption of thermal confinement and constant acoustic speed. However, several factors may introduce distortions. First, as mentioned at the end of part (a) of the method section, the mapping from $\overline{P}_d(u, v, k)$ to $\Phi_d(u, v, w)$ needs interpolation, which is a major source of distortion. This distortion can be reduced by increasing sampling time or applying a better interpolation algorithm in the mapping. Second, in experiments, the detector cannot be scanned over the whole plane. Nevertheless, Fig. 25 shows that collecting data within a finite area of the collection plane can

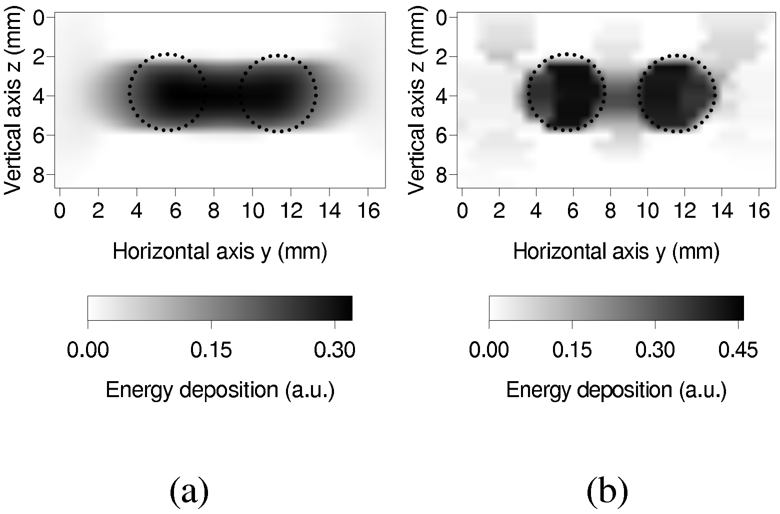

Fig. 26. Demonstration of deconvolution with numeric simulation. The reconstructed images for the same two cylinders as in Fig. 25 from noisy data (a) before and (b) after the deconvolution with respect to the detector surface.

produce images of sufficient definition to determine the configuration and position of the objects.

b. Experimental Result

Fig. 27 shows the experimental result. The images before and after deconvolution with respect to the finite size of the detector surface are shown in Fig. 27(a) and Fig. 27(b), respectively. Fig. 27(c) is the cross section of the biological tissue, which was a cylinder with a radius of about 14 mm and 3 cm long. It consisted of two parts of fat separated by a very thin layer of connective tissue, which is labelled as (7) in the middle of the sample. There were some yellow microstructures among the fat, labelled from (1) to (6), respectively. Fig. 27(a) is the image reconstructed from the experimental data before deconvolution. The connective tissue between the two parts of fat and the yellow microstructures are imaged clearly. The dimension of the image is 16.4 mm along the z direction and 19.2 mm along the y direction. However, it is

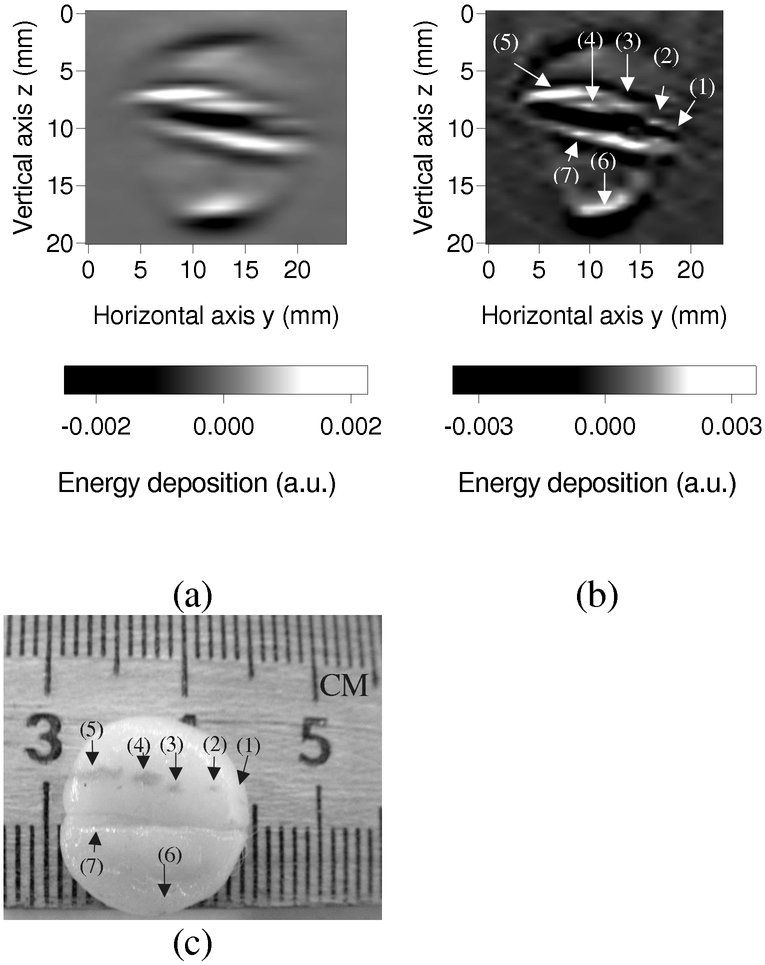

Fig. 27. Demonstration of deconvolution with experimental results. The reconstructed images from the experimental data (a) before and (b) after the deconvolution with respect to the detector surface; (c) the cross section of a cylinder of fat sample containing six yellow microstructures labelled from 1 to 6 and a layer of connective tissue in the middle labelled as 7.

obvious that the image before deconvolution is blurred along the y-axis, which makes the lateral boundaries unclear and the yellow microstructures (1) and (2), (3) and (4) merge into one object, respectively. The lateral resolution of the image needs to be improved. Consequently, deconvolution with respect to the finite size of the detector surface was applied to Fig. 27(a), and the result is shown in Fig. 27(b). The lateral resolution of the image after deconvolution is much improved. The merged objects can be distinguished clearly, and the lateral boundaries of the cylinder become much clearer. The dimension of the image is 16.4 mm along the z direction and 16.7 mm along the y direction.

c. Discussion

There are several advantages of our reconstruction method. The first one is that it is an exact reconstruction algorithm. Unlike other reconstruction methods for TAT that are approximate ones, our reconstruction method provides a solid base for analyzing and improving the quality of reconstructed images. Furthermore, the exact reconstruction method has a broader application than the approximate ones. For example, in both our simulation and experiment, the closest distance between the objects and the detectors was only about 1 cm; this is possible because in principle there is no limitation on the detector-object distance in our method. In other words, the detector can be placed very close to the object to ensure a better SNR. The second advantage of our method is that it can explicitly include the effect of many limitations from the experiment, such as the finite size of detector surface, the microwave pulse length, and the finite frequency response range of the detector. Actually, these analysis are also valid for other approximate reconstruction methods as long as the other reconstruction methods are able to produce images approximating the real objects. Consequently, our analysis of the blur caused by the various experimental limitations can also be very useful for eliminating the limitations in other reconstruction methods. Lastly, since the reconstruction in our method is implemented in the frequency domain, the efficiency of computation is much better than the algorithm implemented in the time domain due to the use of the efficient Fourier transformation in our method. This is especially important for real-time 3-D imaging.

From the above images, it can be seen that there is no speckle in the reconstructed image. Speckles are an important factor limiting the quality of pure ultrasonic imaging. In our technology, the detected signals are directly from the primary acoustic waves rather than reflective or scattered waves. Further, the temporal frequency of the acoustic signals lies in a range from 0 to 1.5 MHz, which is only weakly scattered in the tissues. The above two factors guarantee that there is no obvious speckle in our experimental images. However, the issue of image speckle in more realistic medical imaging applications of our algorithm is a topic for future consideration.

The formulas in this chapter are for TAT in planar geometry only. However, for cylindrical geometry [25], we can predict that the lateral resolution of images can also be improved by deconvolution with respect to the detector surface, where the deconvolution is carried out in a cylindrical surface instead of a plane. For spherical geometry [19], similar work can be conducted as well.

4. Conclusions

We develop a Fourier-domain reconstruction for TAT and obtain an exact and fast reconstruction algorithm. The effects of the finite size of the detectors and the finite length of the excitation pulse are included explicitly in the reconstruction algorithm. The reconstruction algorithm is verified by both numerical simulations and experimental results. Our simulations demonstrate that the blurring caused by the finite size of the detector surface, which is a key limiting factor on the resolution of images, can be alleviated by deconvolution with respect to the detector surface. Other effects that may cause the blur of the images can be treated in a similar way. In the initial experiment, an image in good agreement with the real objects is reconstructed and the deconvolution improves the resolution of the imaging system.

B. CYLINDRICAL GEOMETRY[1]

1. Introduction

In some applications such as the imaging of the limbs, a cylindrical scanning surface may be more appropriate. In this section, using a new expansion formula in cylindrical coordinates, we derive a frequency-domain reconstruction algorithm and report our numerical and experimental results in two-dimensional (2-D) cases.

2. Methods

We assume that the detector scans on a cylindrical surface with a radius of ρ, which encircles all microwave absorbing objects. In this chapter, a coordinate with a prime refers to the position in an imaged object, while a coordinate without a prime refers to that of a detector. In the case of thermal confinement, the temporal spectrum of acoustic field $\bar{p}(\mathbf{r}, k)$ is related to the microwave absorption distribution $\varphi(\mathbf{r}')$ by (1.6). Cylindrical coordinates are used in the following derivation, where z is shown in Fig. 2 of [19], and ρ, ϕ are the polar coordinates within the $x-y$ plane. Following the derivation of the series expansion of $1/|\mathbf{r}-\mathbf{r}'|$ [89], we obtained the following new identity for a series expansion of a spherical wave in a cylindrical coordinate system

---

[1] ©2002 IEEE. Reprinted, with permission from Y. Xu, M. Xu, and L.-H. Wang, "Exact frequency-domain reconstruction for thermoacoustic tomography: II. cylindrical geometry," *IEEE Trans. Med. Imag.*, vol. 21, pp. 829 – 833, 2002.

(see appendix for the derivation):

$$\frac{\exp(-ik\left|\mathbf{r}-\mathbf{r}'\right|)}{4\pi\left|\mathbf{r}-\mathbf{r}'\right|}=\frac{-i}{8\pi}\int_{-\infty}^{\infty}dk_z\exp[-ik_z(z'-z)]\sum_{m=-\infty}^{\infty}A(m,\mu\rho',\mu\rho)\exp[-im(\phi'-\phi)], \tag{5.12}$$

where $\mu = sgn(k)\sqrt{|k^2-k_z^2|}$; sgn() is the signum function; and A is the function defined as:

$$A(m,\mu\rho',\mu\rho)=\{\begin{array}{c} J_m(\mu\rho')H_m^2(\mu\rho),\ \text{if}\ |k|\geq|k_z| \\ \frac{2i}{\pi}I_m(|\mu|\,\rho')K_m(|\mu|\,\rho),\ \text{if}\ |k|<|k_z| \end{array},$$

where $J_m, H_m^2, I_m,$ and K_m are the m-th order Bessel, second-kind Hankel, and modified Bessel functions, respectively. It has been assumed in the above two equations that $\rho > \rho'$. Substituting (5.12) into (1.6) results in

$$\begin{aligned}\bar{p}(\mathbf{r},k) &= \frac{\beta v_s I_0 k\bar{\eta}(k)sgn(k)}{8\pi C}\oint d\mathbf{r}'\varphi(\mathbf{r}')\int_{-\infty}^{\infty}dk_z\exp[-ik_z(z'-z)] \\ &\quad\times\sum_{m=-\infty}^{\infty}A(m,\mu\rho',\mu\rho)\exp[-im(\phi'-\phi)]\ .\end{aligned} \tag{5.13}$$

The $|k|\geq|k_z|$ part of the integration with respect to k_z represents the contribution from the propagation wave, while the $|k|<|k_z|$ part represents the evanescent wave. As the evanescent wave decays rapidly at a distance several wavelengths from the source, it is not suitable for thermoacoustic imaging. For the case of $|k|\geq|k_z|$, after Fourier transforming both sides of the above equation with respect to ϕ and z, we have

$$\bar{p}_1(m,k_z,k)=\frac{\beta v_s I_0 k\bar{\eta}(k)H_m^2(\mu\rho)}{8\pi C}\int_0^{\infty}d\rho'\rho'\varphi_1(m,k_z,\rho')J_m(\mu\rho'), \tag{5.14}$$

where $\bar{p}_1(m,k_z,k)$ and $\varphi_1(m,k_z,\rho')$ are the Fourier transforms of $\bar{p}(\mathbf{r},k)$ and $\varphi(\mathbf{r}')$, respectively. Noticing that the right side of (5.14) is actually a Hankel transform, an inverse Hankel transform gives

$$\varphi_1(m,k_z,\rho') = \frac{8\pi C}{\beta v_s I_0}\int_0^\infty d\mu \frac{\mu \bar{p}_1(m,k_z,k) J_m(\mu\rho')}{k\bar{\eta}(k) H_m^2(\mu\rho)},\ \ |k| \geq |k_z|\,.$$

Applying a variable change of the integral variable from μ to k to the above equation results in

$$\varphi_1(m,k_z,\rho') = \frac{8\pi C}{\beta v_s I_0}\int_{k_z}^\infty dk \frac{\bar{p}_1(m,k_z,k) J_m(\mu\rho')}{\bar{\eta}(k) H_m^2(\mu\rho)},\ \ |k| \geq |k_z|\,. \tag{5.15}$$

At last, $\varphi_1(m,k_z,\rho')$ is inversely Fourier transformed with respect to m and k_z to yield $\varphi(\phi',z',\rho')$. (5.15) gives an exact mapping relation between the spectrum of the collected signals and the spectrum of the distribution of microwave energy deposition and is the essence of our reconstruction method.

An exact reconstruction method for ultrasonic reflectivity imaging with a cylindrical scanning surface was given in [39]. However, our results are much simpler and more stable. In their equation A24, $J_m(\mu r_0)$, where r_0 is the radius of the scanning cylindrical surface, appeared in the denominator and can be zero for some values of μ; consequently, this term can cause instability. In our (5.15), $H_m^2(\mu\rho)$ appeared in the denominator, which cannot be zero for a finite μ.

To summarize, the reconstruction procedure consists of the following steps:

(1) The signal from the detector $p(\phi,z,\bar{t})$ is Fourier transformed with respect to $\bar{t}$ to yield $\bar{p}(\phi,z,k)$. Deconvolution with respect to the finite pulse length can be implemented immediately after the Fourier transform.

(2) $\bar{p}(\phi,z,k)$ is Fourier transformed with respect to z and ϕ, giving $\bar{p}_1(m,k_z,k)$.

(3) According to (5.15), $\bar{p}_1(m,k_z,k)$ is mapped to $\varphi_1(m,k_z,\rho')$.

(4) $\varphi_1(m,k_z,\rho')$ is inversely Fourier transformed with respect to u,v,w to yield $\varphi(\phi',z',\rho')$.

3. Results and Discussion

To test our method, images from both numerically simulated and experimental data were reconstructed in a 2-D case. We chose the 2-D case rather than the three-dimensional (3-D) case to reduce the computational and experimental complexity. For the 2-D case, the reconstruction equation can be derived from (5.14) by replacing all k_z with zero. The extension of the conclusions of the 2-D case to a 3-D one is straightforward.

a. Numerical Simulation

The thermoacoustic imaging of two cylinders was numerically simulated, where the radius of each cylinder was 2 mm; the distance between the centers of the cylinders was 5 mm; and the center of one of the cylinders was positioned at the origin of the circle of detection. Cylinders were chosen because the analytical expression for their thermoacoustic signal is available [86]. In the simulations, the temporal-frequency range was from about 0 to 2 MHz, which was close to our experimental situation [13]. For the noiseless simulated data, the reconstruction is almost perfect. Therefore, we show only the results from noisy data. Fig. 28 shows the images before and after the reconstruction from the simulated data with introduced additive noise. The units for the signals and energy deposition in Fig. 28 and 29 are relative ones. Calibration of our system is needed to obtain an absolute measurement. The radius of the circle of detection was 30 mm; the angular scanning range was 2π with 256 steps; and the thermoacoustic signals were sampled for 50 μs at a sampling rate of 4 MHz. The signal-noise-ratio (SNR) of the raw data shown in Fig. 28(a) was 1. The reconstructed image shown in Fig. 28 (b) is in good agreement with the real objects, whose outlines are plotted as dotted circles in Fig. 28(b). The dimensions of the

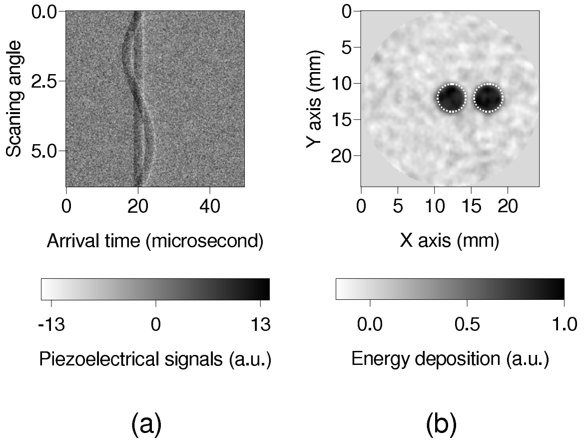

Fig. 28. The images (a) before and (b) after the reconstruction from the simulated data of two cylinders.

reconstructed cylinders are 4 mm along both the x and the y directions. The SNR of the reconstructed image is about 8, which is improved greatly compared with that of the raw data.

b. Experiment Results

The experimental setup for 2-D TAT in a cylindrical configuration is the same as that in [12]. The sample is shown in Fig. 29(a), which was photographed after the experiment. Microwave pulses were delivered to the sample from below. The imaging plane was 2 cm above the bottom of the tissue sample. Above the plane, there is another layer of fat about 1 cm thick. The sample consisted of five muscle cylinders with a diameter of about 3 mm and a height of 6 mm. The muscle cylinders were surrounded by pork fat. The electrical property of interest to this imaging technique is the microwave attenuation coefficient of the medium at the experimental microwave frequency, 3 GHz. The microwave attenuation coefficients of fat and muscle are 9 cm^{-1} and 1 cm^{-1}, respectively. The microwave absorption in mineral oil can be neglected, compared with the absorption in fat and muscle. During the experiment,

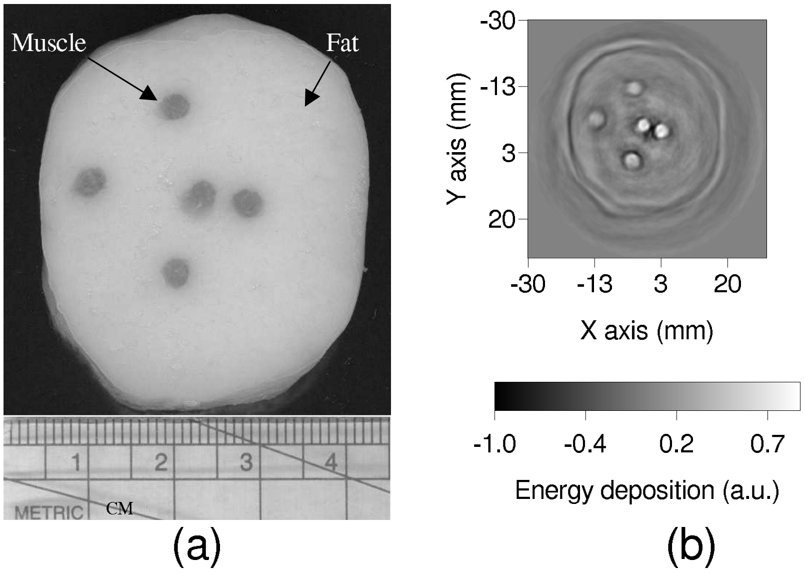

Fig. 29. Experiment results of cylindrical TAT. (a) The cross section of a fat sample containing 5 pieces of muscle cylinders. (b) The reconstructed image from the experimental data.

the transducer scanned around the sample at a radius of 7.1 cm from 0 to 360 degrees with a step size of 2.25 degrees. The thermoacoustic signals were sampled for 60 μs at a sampling rate of 20 MHz. The time between the end of a microwave pulse and the acquisition of the thermoacoustic signal was between 10 μs and 20 μs in our system, depending on the distance of the transducer to the nearest sample surface. Fig. 29(b) shows the reconstructed image from the experimental data. The reconstructed image is in good agreement with the real objects. The boundaries between the fat and the surrounding medium and the muscle cylinders are imaged clearly. However, it can be seen that the quality of the image decreases with the increasing distance of the objects from the center of the circle of detection. One possible reason is that the finite surface area of the detector, which has a 6-mm diameter in this experiment, may cause blurring of the image perpendicular to the radial direction, and this blurring is more serious when the object is farther from the center. Another possible reason is that the microwave field decreases when the radius increases in our irradiation configuration.

Our method can be applied to analyze the effect of the discrete sampling by the detector along the circle of detection on imaging. This can be illustrated by analyzing the signals from a point source located at radius ρ_1. According to (5.14),

$$\bar{p}_1(m, k) \propto J_m(k\rho_1). \tag{5.16}$$

Fig. 30 shows how $J_m(k\rho_1)$ changes with m, where $k = 8.37$ mm $^{-1}$ (the wave number of a 2-MHz acoustic wave) and $\rho_1 = 10$ mm. It is clear that $J_m(k\rho_1)$ has considerable value until $m \approx k\rho_1$, where the Bessel function makes a transition from near-field behavior to far-field behavior. Therefore, it is safe to claim that, with respect to variable ϕ, $\bar{p}(\mathbf{r}, k)$ is band-limited by $k\rho_1$. According to the Nyquist criteria, the number of scanning points per cycle should be at least $2k\rho_1$ to avoid aliasing. In other words, for a fixed number of scanning points N, the maximum wave number before aliasing occurs is $k_{\max} \approx N/(2\rho_1)$. It can be seen that the maximum wave number is inversely proportional to ρ_1. For the same N and temporal spectrum of signal, the aliasing may be more serious for signals coming from sources at a greater radial distance than for those closer to the center. The above analysis also points out a way to produce an aliasing-free image from the data obtained by discrete detection. That is to apply a filter in the temporal-frequency domain to the spectrum of the temporal data with a stopband at about $N/(2\rho_{\max})$, where $\rho_{\max}$ is the maximum radius of imaging range of interest. The application of the filter will decrease the resolution of the image; however, it can guarantee that there will be no aliasing in the image.

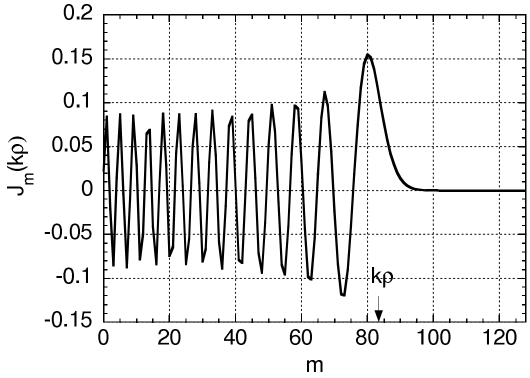

Fig. 30. $J_m(k\rho_1)$ versus m, where $k = 8.37\,\mathrm{mm}^{-1}$ (the wave number of a 2 MHz acoustic wave) and $\rho_1 = 10$ mm.

4. Discussion

Since our method is implemented in the frequency domain using the FFT technique, the computational efficiency is much greater than if implemented in the time domain. The most time-consuming computation in the numerical reconstruction lies in (5.15), which is a Hankel transform. Fortunately, a quasi-fast algorithm for it, which is as efficient as a 1-D fast Fourier transform, is available [90]. Following the methods in [24], our method can explicitly include and further eliminate the effect of many limitations from the experiment, such as the finite size of the detector surface, the microwave pulse length, and the finite response frequency range of the detector. Additionally, combining our method and the techniques in [39], a new exact reconstruction algorithm for 3-D ultrasonic reflectivity imaging with a cylindrical aperture can be derived.

The size of tissue samples that can be imaged by our system is mainly limited by the safety standard on microwave power, the microwave frequency, the microwave irradiation configuration, the sensitivity of the ultrasonic transducer, the dynamic range of the preamplifier and sampling system, and the affordable imaging time. A microwave irradiation configuration that renders a uniform microwave irradiation within the sample will also increase the capacity of the system to image larger samples. A large dynamic range of the preamplifier and the sampling system is necessary to accurately collect the thermoacoustic signals from both the surface and the inside of a sample. A more sensitive ultrasonic transducer and a longer imaging time can improve the signal-to-noise ratio of acoustic signals and make the weak signals from the inside of large samples detectable.

In our initial computation, the reconstruction of a single 2D image required about 2 minutes in a Dell precision 330 computer (Intel Pentium 4 processor with a clock frequency of 1.5 GHz) with Matlab programs if there was no precomputation of Bessel and Hankel functions. However, our initial computation was aimed at verifying the proposed algorithm rather than demonstrating the computation efficiency. The proposed algorithm can be implemented with high computational efficiency as stated in the discussion section. For high computational efficiency, the program should be coded with languages such as C or Fortran, Bessel and Hankel functions should be precomputed, and the fast Hankel transform algorithm should be adopted. The evaluation of the computation efficiency of our algorithm is a topic for future studies.

5. Conclusions

Using a new expansion of a spherical wave in the cylindrical coordinate system, we apply the Fourier transform and Hankel transform techniques to TAT with a cylindrical detection surface. The reconstruction algorithm is verified by both numerical simulations and experimental results in 2-D cases. The method is applied to analyze the effect of discrete sampling by the detector along the circle of detection on imaging; an aliasing-free reconstruction method for discrete sampling along the azimuthal direction is proposed.

CHAPTER VI

CONCLUSIONS

Time-domain methods are proposed to time-reverse a transient scalar wave using only the field measured on an arbitrary closed surface enclosing the initial source. Under certain conditions, a time-reversed field can be approximated by retransmitting the measured signals in a reversed temporal order in a free space. Exact reconstructions for TAT and broadband diffraction tomography (a linearized inverse scattering problem) are proposed by time-reversing the measured field back to the time when each (secondary) source is excited. The theoretical conclusions are supported by a numerical simulation of three-dimensional diffraction tomography. Extension of the results to a heterogeneous medium is discussed.

It is explained theoretically what parts of the image can be stably recovered in the limited-view TAT. Analytic and algebraic reconstruction methods are developed and applied to numerical phantoms and experimental data. Both numerical and experimental results agree perfectly with the theoretical conclusions. The results can be applied practically to quantitative reconstructions with incomplete data, as well as to designing efficient scanning geometries in TAT and interpreting the obtained images.

The effects of acoustic heterogeneity on TAT in the breast are studied. Our analysis shows that the amplitude distortion in the breast TAT is minor. There is no multipath interference in the breast TAT with a convex parenchyma wall, and the amplitude distortion is also not severe for concave boundary, because the TAT signals are broadband, have low central frequency, and experience only one-way transmission through the parenchyma wall. Therefore we consider only phase distortion in our numerical studies. The numerical results on the spread of point sources and boundaries caused by the phase distortion are in good agreement with the predictions of the proposed formula. It is shown that phase distortion can be compensated for when complete or partial information on the distribution of acoustic velocity in the breast is included in the reconstruction. It is found that improvement in the results is more sensitive to measurement error in v_f, v_p than Σ. Based on this sensitivity study, an approach to implement our compensation method using only TAT data is proposed. The differences between breast TAT and breast ultrasound imaging in relation to the effects of acoustic heterogeneity and speckles are accounted for by differences in their central frequency of ultrasound and detection configuration.

We develop a Fourier-domain reconstruction for TAT and obtain an exact and fast reconstruction algorithm. The effects of the finite size of the detectors and the finite length of the excitation pulse are included explicitly in the reconstruction algorithm. The reconstruction algorithm is verified by both numerical simulations and experimental results. Our simulations demonstrate that the blurring caused by the finite size of the detector surface, which is a key limiting factor on the resolution of images, can be alleviated by deconvolution with respect to the detector surface. Other effects that may cause the blur of the images can be treated in a similar way. In the initial experiment, an image in good agreement with the real objects is reconstructed and the deconvolution improves the resolution of the imaging system.

Using a new expansion of a spherical wave in the cylindrical coordinate system, we apply the Fourier transform and Hankel transform techniques to TAT with a cylindrical detection surface. The reconstruction algorithm is verified by both numerical simulations and experimental results in 2-D cases. The method is applied to analyze the effect of discrete sampling by the detector along the circle of detection on imaging; an aliasing-free reconstruction method for discrete sampling along the azimuthal direction is proposed.

REFERENCES

[1] W. Joines, R. Jirtle, M. Rafal, and D. Schaeffer, “Microwave power absorption differences between normal and malignant tissue,” *Radiation Oncology*, vol. 6, pp. 681–687, 1980.

[2] S. Chaudhary, R. Mishra, A. Swarup, and J. Thomas, “Dielectric properties of normal human breast tissues at radiowave and microwave frequencies,” *Ind. J. of Biochem. and Biophys.*, vol. 21, pp. 76–79, 1984.

[3] W. Joines, Y. Zhang, C. Li, and R. Jirtle, “The measured electrical properties of normal and malignant human tissues from 50–900 mhz,” *Med. Phys.*, vol. 21, pp. 547–550, 1994.

[4] W. F. Cheong, S. A. Prahl, and A. J. Welch, “A review of the optical properties of biological tissues,” *IEEE J Quantum Elect.*, vol. 26, pp. 2166–2185, 1990.

[5] L. E. Larsen and J. H. Jacobi, Eds., *Medical Applications of Microwave Imaging.* Piscataway, NJ: IEEE Press, 1986.

[6] S. Caorsi, A. Frattoni, G. L. Gragnani, E. Nortino, and M. Pastorino, “Numerical algorithm for dielectric-permittivity microwave imaging of inhomogeneous biological bodies,” *Med. Biol. Eng. Comput.*, vol. NS-29, pp. 37–44, 1991.

[7] M. S. Hawley, A. Broquetas, L. Jofre, J. C. Bolomey, and G. Gaboriaud, “Microwave imaging of tissue blood content changes,” *J. Biomed. Eng.*, vol. 13, pp. 197–202, 1991.

[8] P. M. Meaney, K. D. Paulsen, and J. T. Chang, “Near-field microwave imaging of biologically-based materials using a monopole transceiver system,” *IEEE Trans. Microwave Theory Tech.*, vol. 46, pp. 31–45, 1998.

[9] X. Wang, Y. Pang, G. Ku, X. Xie, G. Stoica, and L.-H. Wang, "Non-invasive laser-induced photoacoustic tomography for structural and functional imaging of the brain in vivo," *Nature Biotechnology*, vol. 21, pp. 803–806, 2003.

[10] C. G. A. Hoelen, F. F. M. Mul, R. Pongers, and A. Dekker, "Three-dimensional photoacoustic imaging of blood vessels in tissue," *Opt. Lett.*, vol. 23, pp. 648–650, 1998.

[11] A. A. Karabutov, E. V. Savateeva, N. B. Podymova, and A. A. Oraevsky, "Backward mode detection of laser-induced wide-band ultrasonic transients with optoacoustic transducer," *J. of Appl. Phys.*, vol. 87, pp. 2003–2014, 2000.

[12] R. A. Kruger, P. Liu, Y. R. Fang, and C. R. Appledorn, "Photoacoustic ultrasound (PAUS)—reconstruction tomography," *Med. Phys.*, vol. 22, pp. 1605–1609, 1995.

[13] Y. Xu and L.-H. Wang, "Signal processing in scanning thermoacoustic tomography in biological tissues," *Med. Phys.*, vol. 28, pp. 1519–1524, 2001.

[14] T. Bowen, L. Nasoni, A. E. Pifer, and G. H. Sembrosk, "Some experimental results on the thermoacoustic imaging of soft tissue -equivalent phantoms," in *Proc. IEEE Ultrasonics Symposium*, vol. 2, 1981, pp. 823–827.

[15] J. C. Lin and K. H. Chan, "Microwave thermoelastic tissue imaging—system design," *IEEE Trans. Microwave Theory Tech.*, vol. 32, pp. 854–860, 1984.

[16] R. A. Kruger, D. R. Reinecke, and G. A. Kruger, "Thermoacoustic computed tomography—technical considerations," *Med. Phys.*, vol. 26, pp. 1832–1837, 1999.

[17] L.-H. Wang, X. Zhao, H. Sun, and G. Ku, "Microwave-induced acoustic imaging of biological tissues," *Rev. Sci. Instrum.*, vol. 70, pp. 3744–3748, 1999.

[18] G. Ku and L.-H. Wang, "Scanning microwave-induced thermoacoustic tomography: signal, resolution, and contrast," *Med. Phys.*, vol. 28, pp. 4–10, 2001.

[19] M. Xu and L.-H. Wang, "Time-domain reconstruction for thermoacoustic tomography in a spherical geometry," *IEEE Trans. Med. Imag.*, vol. 21, pp. 814–822, 2002.

[20] E. Gusev and A. A. Karabutov, *Laser Optoacoustics.* New York: American Institute of Physics, 1993.

[21] Y. Xu and L.-H. Wang, "Time reversal and its application to tomography with diffracting sources," accepted by *Phys. Rev. Lett.*, 2003.

[22] Y. Xu and L.-H. Wang, "Reconstructions in limited-view thermoacoustic tomography," accepted by *Med. Phys.*, 2003.

[23] Y. Xu and L.-H. Wang, "Effects of acoustic heterogeneity in breast thermoacoustic tomography," *IEEE Trans. Ultrason. Ferroelectr. Freq. Control*, vol. 50, pp. 1134–1146, 2003.

[24] Y. Xu, D. Feng, and L.-H. Wang, "Exact frequency-domain reconstruction for thermoacoustic tomography: I. planar geometry," *IEEE Trans. Med. Imag.*, vol. 21, pp. 823–828, 2002.

[25] Y. Xu, M. Xu, and L.-H. Wang, "Exact frequency-domain reconstruction for thermoacoustic tomography: II. cylindrical geometry," *IEEE Trans. Med. Imag.*, vol. 21, pp. 829 – 833, 2002.

[26] R. P. Porter, “Image formation with arbitrary holographic type surfaces,” *Phys. Lett.*, vol. 29A, pp. 193–194, 1969.

[27] D. Cassereau and M. Fink, “Time-reversal of ultrasonic fields-part III: theory of the closed time-reversal cavity,” *IEEE Trans. Ultrason. Ferroelectr. Freq. Control*, vol. 39, pp. 579–592, 1992.

[28] H. Stark, J. W. Woods, I. Paul, and R. Hingorani, “Direct Fourier reconstruction in computer tomography,” *IEEE Trans. Acous. Speech Signal Processing*, vol. ASSP-29, pp. 237–245, 1981.

[29] K. Nagai, “A new synthetic-aperture focusing method for ultrasonic b-scan imaging by the Fourier transform,” *IEEE Trans. Sonics Ultrason.*, vol. SU-32, pp. 531–536, 1985.

[30] S. X. Pan and A. C. Kak, “A computational study of reconstruction algorithms for diffraction tomography: interpolation versus filtered backprojection,” *IEEE Trans. Acous. Speech Signal Processing*, vol. ASSP-31, pp. 1262–1275, 1983.

[31] R. P. Porter, “Scattered wave inversion for arbitrary receiver geometry,” *J. Acoust. Soc. Am.*, vol. 80, pp. 1220–1227, 1986.

[32] J. Thomas, P. Roux, and M. Fink, “Inverse scattering analysis with an acoustic time-reversal mirror,” *Phys. Rev. Lett.*, vol. 72, pp. 637–640, 1994.

[33] J. H. Rose, “Time-reversal focusing and exact inverse scattering,” in *Imaging of complex media with acoustic and seismic waves*, ser. Topics in applied physics, M. Fink, W. A. Kuperman, J. P. Montagner, and A. Tourin, Eds. New York: Springer, 2002, vol. 84, pp. 97–106.

[34] M. Fink, "Time-reversal of ultrasonic fields-part I: basic principles," *IEEE Trans. Ultrason. Ferroelectr. Freq. Control*, vol. 39, pp. 555–566, 1992.

[35] A. Tourin, A. Derode, and M. Fink, "Sensitivity to perturbations of a time-reversed acoustic wave in a multiple scattering medium," *Phys. Rev. Lett.*, vol. 87, p. 274301, 2001.

[36] E. Wolf, "Three-dimensional structure determination of semi-trasnparent objects from holographic data," *Opt. Commun.*, vol. 1, pp. 153–156, 1969.

[37] A. J. Devaney, "A filtered backpropagation algorithm for diffraction tomography," *Ultrason. Imag.*, vol. 4, pp. 336–350, 1982.

[38] T. Melamed, Y. Ehrlich, and E. Heyman, "Short-pulse inversion of inhomogeneous media: a time-domain diffraction tomography," *Inv. Prob.*, vol. 12, pp. 977–993, 1996.

[39] S. J. Nortan and M. Linzer, "Ultrasonic reflectivity imaging in three dimensions: exact inverse scattering solution for plane, cylindrical and spherical aperture," *IEEE Trans. Biomed. Eng.*, vol. BME-28, pp. 202–220, 1981.

[40] A. J. Devaney and G. Beylkin, "Diffraction tomography using arbitrary transmitter and receiver surface," *Ultrason. Imag.*, vol. 6, pp. 181–193, 1984.

[41] P. M. Morse and K. U. Ingard, *Theoretical acoustics.* New York: McGraw-Hill, 1954.

[42] P. M. Morse and H. Feshbach, *Methods of theoretic physics.* New York: McGraw-Hill, 1953.

[43] M. Xu and L.-H. Wang, "Analytic explanation of spatial resolution related to bandwidth and detector aperture size in thermoacoustic or photoacoustic reconstruction," *Phys. Rev. E*, vol. 67, p. 056605, 2003.

[44] J. A. Fawcett, "Inversion of n-dimensional spherical averages," *SIAM J. Appl. Math.*, vol. 45, pp. 336–341, 1985.

[45] L.-E. Andersson, "On the determination of a function from spherical averages," *SIAM J. Math. Anal.*, vol. 19, pp. 214–232, 1988.

[46] S. Nilsson, "Application of fast backprojection techniques for some inverse problems of integral geometry," Ph.D. dissertation, Linkoping University, Linkoping, Sweden, 1997.

[47] A. Denisjuk, "Integral geometry on the family of semi-spheres," *Fract. Calc. Appl. Anal.*, vol. 2, pp. 31–46, 1999.

[48] V. P. Palamodov, "Reconstruction from limited data of arc means," *J. Fourier Anal. Appl.*, vol. 6, p. 2542, 2000.

[49] F. Natterer and F. Wuebbeling, *Mathematical Methods in Image Reconstruction.* Philadelphia, PA: SIAM.

[50] K. P. Kostli, M. Frenz, H. Bebie, and H. P. Weber, "Temporal backward projection of optoacoustic pressure transients using Fourier transform methods," *Phys. in Med and Bio.*, vol. 46, pp. 1863–1872, 2001.

[51] C. G. A. Hoelen and F. F. M. Mul, "Image reconstruction for photoacoustic scanning of tissue structures," *Applied Optics*, vol. 39, pp. 5872–5883, 2001.

[52] M. L. Agranovsky and E. T. Quinto, “Injectivity sets for the radon transform over circles and complete systems of radial functions,” *J. of Func. Anal.*, vol. 139, pp. 383–413, 1996.

[53] A. H. Delaney and Y. Bresler, “Globally convergent edge-preserving regularized reconstruction: an application to limited-angle tomography,” *IEEE Trans. Imag. Proc.*, vol. 7, pp. 204–221, 1998.

[54] X. Pan and M. Anastasio, “Minimum-scan filtered backpropagation algorithms in diffraction tomography,” *J. Opt. Soc. Am.*, vol. 16, pp. 2896–2903, 1999.

[55] X. Pan, Y. Zou, and M. Anastasio, “Data redundancy and reduced-scan reconstruction in reflectivity tomography,” *IEEE Trans. Image Proc.*, vol. 12, pp. 784–795, 2003.

[56] A. K. Louis and E. T. Quinto, “Local tomographic methods in sonar,” in *Surveys on solution methods for inverse problems.* Vienna: Springer, 2000, pp. 147–154.

[57] E. T. Quinto, “Singularities of the x-ray transform and limited data tomography in p^2 and p^3,” *SIAM J. Math. Anal.*, vol. 24, pp. 1215 – 1225, 1993.

[58] A. Faridani, E. L. Ritman, and K. T. Smith, “Local tomography,” *SIAM J. Appl. Math.*, vol. 52, pp. 459–484, 1992.

[59] A. Faridani, E. L. Ritman, and K. T. Smith, “Local tomography examples of local tomography,” *SIAM J. Appl. Math.*, vol. 52, pp. 1193–1198, 1992.

[60] A. Faridani, D. Finch, E. Ritman, and K. Smith, “Local tomography II,” *SIAM J. Appl. Math.*, vol. 57, pp. 1095–1127, 1997.

[61] P. Kuchment, K. Lancaster, and L. Mogilevskaya, “On local tomography,” *Inverse Problems*, vol. 11, pp. 571–589, 1995.

[62] V. Isakov, *Inverse problems for partial differential equations*, ser. Applied Math. Sci. Springer-Verlag, Berlin, 1998, vol. 127.

[63] G. Beylkin, "The inversion problem and applications of the generalized radon transform," *Comm. Pure Appl. Math.*, vol. 37, pp. 579–599, 1984.

[64] D. Feng, Y. Xu, G. Ku, and L.-H. Wang, "Microwave-induced thermoacoustic tomography: reconstruction by synthetic aperture," *Med. Phys.*, vol. 28, pp. 2427–2431, 2001.

[65] C. G. A. Hoelen, R. Pongers, G. Hamhuis, F. F. M. Mul, and J. Greve, "Photoacoustic blood cell detection and imaging of blood vessels in phantom tissue," in *SPIE*, vol. 3196, 1998, pp. 142–153.

[66] M. Moshfeghi and R. C. Waag, "In vivo and in vitro ultrasound beam distortion measurements of a large aperture and a conventional aperture focused transducer," *Ultrsound Med. Bio.*, vol. 5, pp. 415–428, 1988.

[67] Q. Zhu and B. D. Steinberg, "Large-transducer measurements of wavefront distortion in the female breast," *Ultrason. Imag.*, vol. 14, pp. 276–299, 1992.

[68] C. W. Manry and S. L. Broschat, "FDTD simulations for ultrasound propagation in a 2-d breast model," *Ultrason. Imag.*, vol. 18, pp. 25–34, 1996.

[69] P. D. Freiburger, D. C. Sullivan, B. H. Leblanc, S. W. Smith, and G. E. Trahey, "Two dimensional ultrasonic beam distortion in the breast: in vivo measurements and effects," *Ultrason. Imag.*, vol. 14, pp. 398–414, 1992.

[70] S. W. Flax and M. O'Donnell, "Phase aberration correction using signals from point reflectors and diffuse scatters: basic principles," *IEEE Trans. Ultrason. Ferroelect. Freq. Contr.*, vol. 35, pp. 758–767, 1988.

[71] G. E. Trahey, D. Zhao, J. A. Miglin, and S. W. Smith, “Experimental results with a real-time adaptive ultrasonic imagining system for viewing through distorting media,” *IEEE Trans. Ultrason. Ferroelect. Freq. Contr.*, vol. 37, pp. 418–427, 1990.

[72] Q. Zhu and B. D. Steinberg, “Deaberration of incoherent wavefront distortion: an approach toward inverse filtering,” *IEEE Trans. Ultrason. Ferroelect. Freq. Contr.*, vol. 44, pp. 575–589, 1997.

[73] H. P. C., *Rank-deficient and discrete ill-posed problems.* Philadelphia, PA: SIAM Press, 1998.

[74] A. V. Oppenheim and J. S. Lim, “The importance of phase in signals,” in *Proc. IEEE*, 1981, pp. 529–541.

[75] B. D. Steinberg, “A theory of the effect of hard limiting and other distortions upon the quality of microwave images,” *IEEE Trans. Acoustics Speech and Sig. Proc.*, vol. ASSP-35, pp. 1462–1472, 1987.

[76] A. R. Selfridge, “Approxiamte properties in isotropic materials,” *IEEE Trans. on Sonics and Ultrason.*, vol. SU-32, pp. 381–394, 1985.

[77] F. S. Foster, M. Strban, and G. Austin, “The ultrasound microscope: initial studies of the breast tissue,” *Ultra. Imag.*, vol. 6, pp. 243–261, 1984.

[78] L. A. Chernov, *Wave propagation in a random medium.* New York: Dover Publications, 1960.

[79] F. S. Foster, M. Strban, and G. Austin, “The ultrasound microscope: initial studies of the breast tissue,” *Ultrason. Imag.*, vol. 6, pp. 243–261, 1984.

[80] G. Kossoff, E. K. Fry, and J. Jellins, "Average velocity of ultrasound in the human female the breast," *J. Acous. Soc. Am.*, vol. 53, pp. 1730–1736, 1973.

[81] R. Sneider and D. F. Aldridge, "Perturbation theory for travel times," *J. Acoust. Soc. Am.*, vol. 98, pp. 1565–1569, 1995.

[82] W. T. V. William H. P., Saul A. T. and B. P. F., *Numerical recipes in C.* Cambridge: Cambridge University Press, 1992.

[83] J. F. Greenleaf and R. C. Bahn, "Clinical imaging with transmissive ultrasonic computerized tomography," *IEEE Trans. Biom*, vol. BME-28, pp. 177–185, 1981.

[84] J. Lu, "Experimental study of high frame rate imaging with limited diffraction beams," *IEEE Trans. Ultrason. Ferroel. Frequency Control*, vol. 45, pp. 84–97, 1998.

[85] W. J. Kiser and R. A. Kruger, "Thermoacoustic computed tomography-limits to spatial resolution," in *SPIE*, vol. 3659, 1999, pp. 895–905.

[86] G. J. Diebold, M. I. Khan, and S. M. Park, "Photoacoustic signatures of particulate matter: optical production of acoustic monopole radiation," *Science*, vol. 250, pp. 101–104, 1990.

[87] K. Jain, *Fundamentals of digital image processing.* Englewood Cliffs, New Jersey: Prentice Hall, 1989.

[88] P. C. Hansen and K. Mosegaard, "Piecewise polynomial solutions without priori breakpoints," *Num. Lin. Alg. Appl.*, vol. 3, pp. 513–524, 1996.

[89] J. D. Jackson, *Classical electrodynamics.* New York: Wiley, 1975.

[90] A. E. Siegman, "Quasi fast hankel transform," *Opt. Lett.*, vol. 1, pp. 13–15, 1977.

[91] M. Abramowitz and I. A. Stegun, *Handbook of mathematical functions.* New York: Dover, 1972.

APPENDIX A

DERIVATION OF (2.13)

First, after combining (2.12), (2.20) and the time-domain form of (2.2), it can be found that $g_1(\mathbf{r}, t\,|\mathbf{r}_d\,, t_0)$ only within $t < A_g$, where $A_g = t_0 + (|\mathbf{r} - \mathbf{r}_d| + 2l_{obj})/v_s$, is needed to compute $p_r(\mathbf{r}, \hat{t}_e(\mathbf{r}))$ using (2.12) for DT application. Secondly, when $\mathbf{r}$ is around the center of Σ and $l_{\text{det}} > 2l_{obj}$, the flight-time difference between the first two rays (arriving at $\mathbf{r}$ at time $t_0 + |\mathbf{r} - \mathbf{r}_d|\,/v_s$) and the other rays (such as ray DAB) is larger than $2l_{obj}/v_s$ in most cases and, consequently, the rays other than the first two make contribution to $g_1(\mathbf{r}, t\,|\mathbf{r}_d\,, t_0)$ only when $t > A_g$, and to $p_r(\mathbf{r}, t)$ only when $t > \hat{t}_e(\mathbf{r})$.

APPENDIX B

DERIVATION OF (3.2)

(3.1) can be rewritten as

$$p_1(\mathbf{r},t) = \frac{\beta I_0}{4\pi C}\mathbf{D}_t\frac{\mathbf{R}\varphi}{t}. \tag{B.1}$$

We define $p_2(\mathbf{r},t) = v_s\int_0^t p_1(\mathbf{r},t)dt$. Then we have

$$\frac{4\pi Ctp_2(\mathbf{r},t)}{\beta I_0 v_s} = \mathbf{R}\varphi. \tag{B.2}$$

If the detector is not very close to the objects, we can approximate the circular Radon transform by the standard Radon transform. The forward and inverse formulas for the standard Radon transform are [49]

$$m(\varsigma,\theta) = \int\limits_{r\cdot\theta=\varsigma}^{f(\mathbf{r})} d\mathbf{r}, \tag{B.3}$$

and

$$f(\mathbf{r}) = \frac{1}{4\pi}\int\limits_0^{2\pi} d\theta\,\mathbf{H}\frac{\partial m(\mathbf{r}\cdot\theta,\theta)}{\partial\varsigma}, \tag{B.4}$$

where **H** is Hilbert transform. Although the circular Radon transform is different, one can write down an approximate inversion formula modeled after (B.4). By combining an analog of (B.4) with (B.2), one obtains an approximate formula

$$\varphi(\mathbf{r}) \approx \frac{C}{\beta I_0 v_s^2}\int_0^{2\pi} d\theta\mathbf{H}(p_1(\mathbf{r}_\theta, |\mathbf{r}_\theta - \mathbf{r}|/v_s)\,|\mathbf{r}_\theta - \mathbf{r}| + p_2(\mathbf{r}_\theta, |\mathbf{r}_\theta - \mathbf{r}|)), \tag{B.5}$$

where θ is defined as in Fig. 6. According to Fig. 6, we have the relation

$$d\theta = ds\frac{\mathbf{n}\cdot(\mathbf{r}-\mathbf{r}_\theta)}{|\mathbf{r}-\mathbf{r}_\theta|^2}, \tag{B.6}$$

where $\mathbf{n}$ is the inward normal to the detection curve at $\mathbf{r}_\theta$ and ds is the arc length differential of the detection curve. After substituting this identity into (B.5) we obtain (3.2). (3.4) can be derived in a similar way.

APPENDIX C

DERIVATION OF (4.3)

Assume the concave boundary can be approximated by an arch with a radius $R_l > a$, where a is half the size of the boundary segment. Two rays are refracted at points B_1 and B_2 in Fig. 16, where B_2 has a small displacement from B_1 along the boundary. According to the refraction law, we have

$$\sin\theta_1 = (1-\alpha)\sin\phi_1,$$

$$\cos\theta_1 d\theta_1 = (1-\alpha)\cos\phi_1 d\phi_1, \tag{C.1}$$

where $d\phi_1$ is the difference between the incidence angles of the two rays and $d\theta_1$ is the transmission one. They can be expressed as

$$d\theta_1 = (1 - \frac{R_l \cos\theta_1}{l_{B_1 D}})d\theta$$

$$d\phi_1 = (\frac{R_l \cos\phi_1}{l_{SB_1}} + 1)d\theta, \tag{C.2}$$

where l_{SB_1} and l_{B_1D} are the distances from the boundary point B_1 to source S and detector D, respectively, and $d\theta = l_{B_1B_2}/R_l$. Combining the above equations, we have the imaging formula for the boundary segment

$$\frac{\cos^2\phi_1}{l_{SB_1}} + \frac{\cos^2\theta_1}{l_{DB_1}(1-\alpha)} = \frac{\cos\theta_1/(1-\alpha) - \cos\phi_1}{R_l}. \tag{C.3}$$

Since in our breast model $\alpha \approx 0.1$ is small, the above equation can be further simplified to (4.3) after using $\theta_1 \approx \phi_1$.

APPENDIX D

DERIVATION OF (4.22)

The first iteration in TCG is equivalent to the backprojection method [22]. In backprojection for an acoustically homogeneous TAT, $\varphi(\mathbf{r}, t)$, the signal detected at $\mathbf{r}$ and time t is projected back to a sphere with a radius of tv_{s0} and a center at $\mathbf{r}$. It is shown that the boundaries of objects can be reconstructed correctly with the backprojection method [56]. Let's consider a model illustrated in Fig. 19 to estimate the spread of source S along line D_1D_2, where D_1 and D_2 are two detectors; S_1 is the intersection of D_1D_2 with the backprojection arch of the signal transmitted by source S and detected by detector D_1; S_2 is the corresponding one at D_2, and Σ represents the parenchyma wall. If there is no error in computing TOFs, S_1, S_2, and S will be one point; therefore, a point image of source S can be recovered. In an acoustically heterogeneous model, however, the flight-time errors caused by the approximation of v_p by v_{s0} in the reconstruction result in the splitting of S_1 and S_2 from S, where l_{S_1S} and l_{S_2S} can be estimated by the multiplication of the flight-time errors with v_{s0}, $l_{S_1S} = l_{B_1S}(1 - v_{s0}/v_p) = \alpha l_{B_1S}$ and $l_{S_2S} = l_{B_2S}(1 - v_{s0}/v_p) = \alpha l_{B_2S}$. Combining them together, we have (4.22) for the spread width of source S along line D_1D_2. Similar analysis can be applied to estimating BSW as well.

APPENDIX E

DERIVATION OF (5.12)

The derivation of (5.12) will be presented here. The spherical wave $G_k(\mathbf{r}, \mathbf{r}') = \exp(-ik\,|\mathbf{r}-\mathbf{r}'|)/(4\pi\,|\mathbf{r}-\mathbf{r}'|)$ is a solution to the wave equation with a point source:

$$\nabla^2_{\mathbf{r}} G_k(\mathbf{r}, \mathbf{r}') + k^2 G_k(\mathbf{r}, \mathbf{r}') = -\delta(\mathbf{r}-\mathbf{r}') \ . \tag{E.1}$$

The solution can be expanded in terms of orthonormal functions of z and ϕ in a cylindrical coordinate system:

$$G_k(\mathbf{r}, \mathbf{r}) = (\frac{1}{2\pi})^2 \sum_{m=-\infty}^{\infty} \int_{-\infty}^{\infty} dk_z g_m(k, k_z, \rho, \rho') \exp[im(\phi-\phi') + ik_z(z-z')] \ . \tag{E.2}$$

Substituting (E.2) into (E.1) results in an equation for the radial Green's function g_m:

$$\frac{1}{\rho}\frac{d}{d\rho}(\rho\frac{dg_m}{d\rho}) + (k^2 - k_z^2 - \frac{m^2}{\rho^2})g_m = -\frac{\delta(\rho-\rho')}{\rho} \ . \tag{E.3}$$

When $|k| < |k_z|$, following the derivation of the series expansion of $1/|\mathbf{r}-\mathbf{r}'|$ [89], one obtains a similar expansion for the spherical wave:

$$g_m = I_m(|\mu|\,\rho')K_m(|\mu|\,\rho) \ . \tag{E.4}$$

We next consider the case of $|k| \geq |k_z|$ and $k > 0$. Noticing that when $\rho \to \infty$, g_m behaves asymptotically as $\exp[-i\mu(\rho-\rho')]$ ($\rho > \rho'$ is implicit in our model), one can follow the derivation in [89] and obtain

$$g_m = \frac{\pi}{2i} J_m(\mu\rho')H_m^2(\mu\rho) \ . \tag{E.5}$$

Similarly, for $|k| \geq |k_z|$ and $k < 0$:

$$g_m = \frac{\pi i}{2} J_m(|\mu|\,\rho')H_m^1(|\mu|\,\rho) \ . \tag{E.6}$$

Using the following identities of Bessel and Hankel functions [91]:

$$H_m^1(\mu\rho) = -(-1)^m H_m^2(-\mu\rho),$$

$$J_m^{(}\mu\rho) = (-1)^m J_m^{(} - \mu\rho),$$

and combining (E.2), (E.4), (E.5), and (E.6), we obtain (5.12).

VITA

YUAN XU

Ph.D. Biomedical Engineering

Texas A&M University, College Station, Texas, 2003

Advisor: Dr. Lihong V. Wang

Ph.D. Physics

Institute of Physics, Chinese Academy of Sciences, Beijing, China, 1999

Advisor: Dr. Long Wang

M.S. Physics

Shanghai Institute of Optics and Fine Mechanics, Shanghai, China, 1995

B.S. Physics

Wuhan University, Wuhan, China, 1992

Permanent address:

Dr. Lihong V. Wang, 233 Zachry Engineering Center TAMU 3120
College Station, TX 77843-3120